Dissertation

submitted to the

Combined Faculties of the Natural Sciences and Mathematics

of the Ruperto-Carola-University of Heidelberg, Germany

for the degree of

Doctor of Natural Sciences

Put forward by

Nicolaas Petrus Marcus Brantjes

Born in Groningen, the Kingdom of the Netherlands

Day of oral examination: June 27th, 2012

The g-Factor of Hydrogen-Like Heavy Ions as a Test for QED

First referee: Priv. Doz. Dr. Wolfgang Quint

Second referee: Prof. Dr. Klaus Blaum

Zusammenfassung

Diese Arbeit beschreibt die Konzeption und den Aufbau eines Experiments zum Test der Quantenelektrodynamik (QED) in Gegenwart von starken elektromagnetischen Feldern. Der g-Faktor eines geladenen Teilchens ist eine dimensionslose Konstante. Er beschreibt das Verhältnis des magnetischen Moments des Teilchens zu seinem Drehimpuls und bestimmt die Stärke der Wechselwirkung zwischen dem Teilchen und dem Magnetfeld. Im Fall eines Elektrons, das im Feld eines schweren Kerns gebunden ist, wird der g-Faktor mit großer Genauigkeit von der Quantenelektrodynamik gebundener Zustände (BS-QED) vorhergesagt. Somit dient die genaue Bestimmung des g-Faktors eines Ions in einer Penning-Falle als strenge Überprüfung der BS-QED. Ein Bündel von schweren hochgeladenen Ionen wird an der GSI-HITRAP Anlage erzeugt und abgebremst. Die Ionen werden schließlich in der Kühlerfalle eingefangen und auf 4 Kelvin abgekühlt. Die kalten Ionen werden in die g-Faktor-Penning-Falle transportiert und eingeschossen. Hier wird der g-Faktor wird mit Hilfe von Laser-Mikrowellen-Doppel-Resonanz-Spektroskopie bestimmt. Derzeit ist das Einfangen von Elektronen in der Kühlerfalle möglich, und die Falle ist bereit, Ionen in den nächsten Monaten zu speichern.

Abstract

This thesis describes the design and construction of an experiment to test quantum electrodynamics (QED) in the presence of strong electromagnetic fields. The g-factor of a charged particle is a dimensionless constant. It relates the particle's magnetic moment to its angular momentum and as such it determines the strength of the interaction between the particle and the magnetic field. In the case of an electron bound in the field of a heavy nucleus, the g-factor is predicted to great accuracy by bound-state quantum electrodynamics (BS-QED). Thus, the accurate determination of the g-factor of an ion inside a Penning trap serves as a stringent test of BS-QED. A bunch of heavy highly-charged ions are created and decelerated at the GSI-HITRAP facility. The bunch is finally captured and cooled to 4 Kelvin inside the Cooler trap. The cold ions are transported and injected into the g-factor Penning trap. Here the g-factor is determined using laser-microwave double-resonance spectroscopy. Presently, electron trapping is possible inside the Cooler trap and the trap is being prepared to trap ions.

Samenvatting

Dit proefschrift beschrijft het ontwerp en de bouw van een experimentele opstelling met als doel de quantum elektrodynamica (QED) in de aanwezigheid van sterke elektrische velden te testen. De *g*-factor van een geladen deeltje is een dimensieloze constanted die het magnetisch moment aan het impulsmoment van dat deeltje relateert. Als zodanig bepaalt de *g*-factor de kracht van de interactie tussen een geladen deeltje en het magnetische veld. Bij een elektron dat is gebonden in het electrisch veld van een zware kern wordt de *g*-factor met grote nauwkeurigheid voorspeld door de quantum elektrodynamica voor gebonden toestanden (BS-QED). Een nauwkeurige experimentele bepaling van de *g*-factor van een ion in een Penning val is dus een stringente test van BS-QED. Een bundel hooggeladen ionen wordt geproduceerd en vertraagd aan de GSI-HITRAP faciliteit. De bundel wordt ingevangen en tot 4 Kelvin gekoeld in de 'Cooler Trap'. De koude ionen worden getransporteerd naar en geïnjecteerd in de *g*-factor Penning val. Hierin wordt de *g*-factor bepaald door middel van laser en microgolf spectroscopie. Elektronen zijn al in de 'Cooler Trap' ingevangen en de opstelling wordt voorbereid om ook ionen in te vangen.

Table of Contents

List of Tables

List of Figures

xi

xiv

1   Precision Test of QED

In physics, one of the most successful theories, in terms of predictive power, is quantum electrodynamics (QED). Its foundations were laid in the 1920's. QED is a relativistic quantum field theory that describes the interactions between charged particles and photons. One of the strong points of QED is that observables can be predicted with relative accuracies of over 10^{-12} [1, 2]. At the same time, experimental precision is sufficient to test these predictions at almost the same level.

While the predictive power of QED is unrivalled, the inner workings of the theory are made intuitive with the aid of the Feynman rules and diagrams (such as shown in figure 1.1). An initial solution can be calculated using only the simplest of diagrams. Additional precision is then created by calculating the next-order Feynman diagrams, or, colloquially, by calculating the diagrams with more photon or particle-antiparticle loops.

This work presents the development towards an experiment to measure the *g*-factor of hydrogen-like (H-like) heavy ions in a Penning trap. The value of the *g*-factor is predicted to high accuracy by QED (see sections 1.2 and 1.3). Also, it can be measured with great experimental precision, as explained in section 1.1. This combination of experimental and theoretical precision makes the measurement of the *g*-factor an excellent method to test QED.
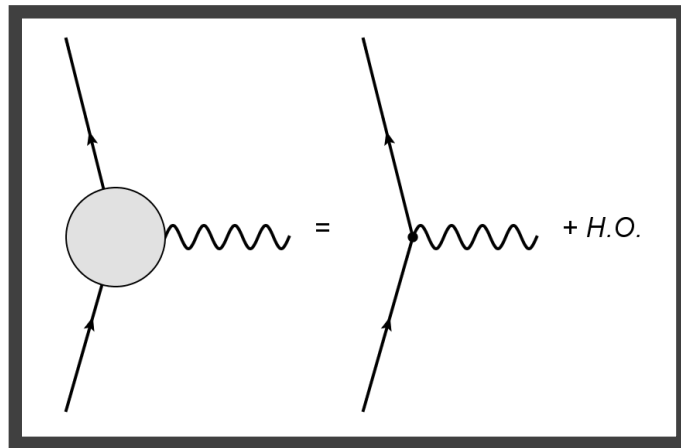
Figure 1.1: Generalised particle-photon interaction through Feynman diagrams. The grey area contains the interaction for all orders. The second diagram is the lowest order diagram for the interaction. Higher order terms (H.O.) contain combinations of photon and particle-antiparticle loops.

1.1 g-Factor

For a charged particle, with spin angular-momentum **S**, the magnetic dipole moment **μ** is proportional to **S**. In a homogeneous magnetic field **B**, such as in figure 1.2, the particle has a magnetic potential energy $V = -\boldsymbol{\mu} \cdot \boldsymbol{B}$.
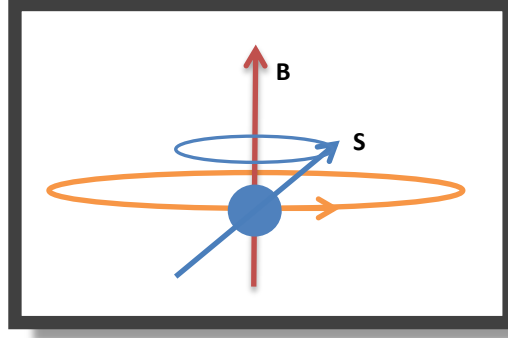
*Figure 1.2: A charged particle with angular momentum **S** in a magnetic field **B**. In this picture, **S** precesses around the magnetic field axis (blue circle). The particle itself also moves in a 'cyclotron' orbit (orange circle) around the magnetic field lines.*

The g-factor of a charged particle is a proportionality constant that relates the magnetic moment of that particle to its spin angular momentum. For the free electron the g-factor (g_e) is defined as:

$$\boldsymbol{\mu_S} = g_e \mu_B \frac{\boldsymbol{S}}{\hbar} \qquad\qquad 1.1$$

Here $\boldsymbol{\mu_S}$ is the magnetic moment, μ_B the Bohr magneton, $\hbar$ Planck's constant and **S** the intrinsic angular momentum of the electron. In the presence of an external magnetic field **B**, the energy of the system shifts with $-\boldsymbol{\mu_S} \cdot \boldsymbol{B}$. This energy shift is also proportional to the Larmor precession frequency ($\omega_L = \frac{g_e\,e}{2\,m}B$) such that:

$$g_e = 2\frac{\omega_L}{\omega_c} \qquad\qquad 1.2$$

Here ω_c is the cyclotron frequency of the electron in the magnetic field given by: $\omega_c = \frac{e}{m}B$. From equation 1.2 it is clear that the g-factor can be, experimentally, determined as the ratio of two frequencies. As such, this makes the g-factor an easily measured observable that can be determined with great accuracy. Indeed, the g-factor of the free electron has been measured with below a part-per-trillion precision [3, 4] to $\frac{g}{2} = 1.001\ 159\ 652\ 180\ 73(28)$.

System	Experimental result	Theoretical Prediction
Free Electron (e⁻)	2.002 319 302 361 46(56)	2.002 319 304 361 53*
Hydrogen (H)	2.002 283 845(26)	2.002 283 853
H-Like Helium (He⁺)	2.002 259 33(60)	2.002 177 407
H-Like Carbon (C⁵⁺)	2.001 041 596 3(10)(44)	2.001 041 590 18(3)
H-Like Oxygen (O⁶⁺)	2.000 047 026 0(15)(44)	2.000 047 020 32(11)
H-Like Silicon (Si¹³⁺)	1.995 3489 587 (5)(3)(8)	1.995 3489 580(17)
H-Like Lead (Pb⁸¹⁺)	1.78(12)	1.738 3
H-Like Bismuth (Bi⁸²⁺)	1.734 1(35)	1.731 013 38

Table 1.1: Known g-factors for single electron systems [3-11]. The literature value for the theoretical free electron g-factor (*) is taken from CODATA. For the systems carbon, oxygen and silicon, the g-factor was measured in a Penning trap by observing the continuous Stern-Gerlach effect [12]. For the heavy systems, the lifetime of the excited state was measured through spectroscopy in a storage ring. From this, an experimental figure for the g-factor has been calculated.

When the electron is bound to an atomic nucleus with mass M and charge Z, the electron spin is no longer an observable quantity. Instead the total angular momentum ($J = L + S$) is the combination of the electron spin and the orbital angular momentum (L) of this electron. For the total angular momentum, the Landé g-factor (g_J) is defined along the lines of equation 1.1. It can be obtained from the measurable quantities [13]:

$$g_J = 2\frac{Q}{e}\frac{m}{M}\frac{\omega_L}{\omega_c} \qquad\qquad 1.3$$

The Landé g-factor has been successfully measured for several light hydrogen-like ions (Table 1.1). Currently, an experiment is under way to determine the g-factor of a single electron bound in calcium [14, 15].

If the nucleus has a non-zero spin (I) of its own, the nuclear spin and the electron angular momentum (J) couple together into the total angular momentum of the ion ($F = J + I$). The ionic g-factor (g_F) contains both g_J of the bound electron and g_I of the nucleus. With m_e and m_p the masses of the electron and proton, respectively, g_F is given by [16, 17]:

$$g_F = g_J \frac{F(F+1) + J(J+1) - I(I+1)}{2F(F+1)}$$
$$- \frac{m_e}{m_p} g_I \frac{F(F+1) + I(I+1) - J(J+1)}{2F(F+1)} \qquad 1.4$$

1.2   The free electron in an external magnetic field

The Dirac equation predicts the value of the *g*-factor of the free electron as exactly 2 [18, 19]. However, a more accurate prediction can be calculated with QED. The interaction of a charged particle, like the electron, with the electromagnetic field can be split into the electric field contributions and the magnetic contributions. The electron can interact with these fields both through its charge and through its magnetic dipole moment. The part where the electron interacts with a magnetic field (**B**) through its magnetic moment (**μ**) contains the *g*-factor. This means that, in order to extract the *g*-factor, the part containing $\boldsymbol{\mu} \cdot \boldsymbol{B}$ must be separated from the full interaction between the electron and the electromagnetic field. The aim of this section is to sketch how this is done and how the *g*-factor can be determined using Feynman diagrams.

In QED, the full interaction is described by the interaction Hamiltonian [19]:

$$H_{int} = ie \int d^3x \big[A_\mu(x) j^\mu(x) \big] \qquad 1.5$$

Here *e* is the electron charge, $A_\mu(x)$ the electromagnetic field and $j^\mu(x)$ is the current density. Consider an electron with momentum p and spin s, interacting with this field. The matrix element for the interaction is:

$$\langle p', s | H_{int} | p, s \rangle \sim \int d^3x \, \bar{u}(p', s) A_\mu(x) \Gamma^\mu(p', p) u(p, s) e^{ikx} \qquad 1.6$$

Here $u(p, s)$ is the spinor wave function that describes the electron. $\Gamma^\mu(p', p)$ is called the vertex function. It describes the physical interaction as shown in figure 1.1 and includes the basic 1 photon interaction as well as the higher order corrections. This vertex function transforms as a vector. It must be a linear combination of the vectors: γ^μ, p^μ and p'^μ. Here γ^μ are, as usual, the Dirac matrices. So, it can be written as:

$$\Gamma^\mu(p', p) = F(k^2)\gamma^\mu + \frac{1}{2m}G(k^2)P^\mu \qquad 1.7$$

4

$F(k^2)$ and $G(k^2)$ are form factors that must be calculated with $k = p' - p$ and $P^\mu = p^\mu + p'^\mu$. A third term, holding the momentum difference, $K^\mu = p^\mu - p'^\mu$, is forbidden [19, 20]. In the lowest order, depicted in figure 1.1, $F(k^2) = 1$ and $G(k^2) = 0$ [20]. The matrix element in 1.6, amongst others, contains the interaction between the electron magnetic moment, and thus its angular momentum, and the electromagnetic field. The interaction of the electron, through its angular momentum, with the magnetic field shifts the energy of the system. When $A_\mu(x)\gamma^\mu$ is written explicitly in terms of E and B, this shift can be extracted from equation 1.8:

$$\langle p', s | H_{spin} | p, s \rangle \sim F(k^2) \int d^3x \, \bar{u}(p', s) \mathbf{S} \cdot \mathbf{B}(x) u(p, s) e^{ikx} \qquad 1.8$$

Here S is the four-dimensional spin matrix. $B(x)$ denotes the magnetic field. For a magnetic field that does not depend on x, the right-hand side of equation 1.8 becomes:

$$-\frac{e}{m} F(0) \bar{u}(p, s) \mathbf{S} \cdot \mathbf{B} u(p, s) \delta^3(\vec{p}' - \vec{p}) = -\boldsymbol{\mu} \cdot \mathbf{B} \qquad 1.9$$

Here it should be noted that we look at the electron in its rest frame. The magnetic moment in this system has the magnitude:

$$|\mu| = \frac{e}{2m} F(0) = \frac{e}{2m} [1 - G(0)] \qquad 1.10$$

Rewriting the form factor $F(0)$ into the form factor $G(0)$, allows the g-factor to be conveniently defined as its Dirac value modified by QED contributions.

$$g = 2[1 - G(0)] \qquad 1.11$$

As $G = 0$ in the lowest order, QED predicts the leading term of the g-factor as 2 and any deviation from this value is the result of higher order corrections. The expression based on $G(0)$ is not chosen entirely for convenience. In fact, both form factors $F(k^2)$ and $G(k^2)$ are contained within the vertex function. And by defining $F(0) + G(0) = 1$ we identify e with the physical charge of the electron [19]. Now the calculation of the g-factor reduces to evaluating of the vertex function and extracting the part that depends on the combined incoming and outgoing momentum (P^μ). The Feynman rules give an expression for the vertex function. It contains a summation over all Feynman diagrams up to the desired level of complexity.
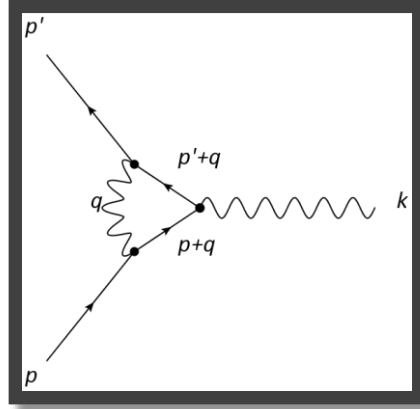
Figure 1.3: Feynman diagram of order α contribution to the g-factor. Straight lines indicate electrons and the wavy lines are the photons. Particle momenta are as indicated. The external photon indicates the interaction with the magnetic field. This particular diagram is also termed the "vertex correction".

In the case of the g-factor the first contribution to $G(0)$ is the vertex correction. This diagram is shown in figure 1.3. Using the Feynman rules for QED interactions, this diagram then translates into the following term of the vertex function:

$$\delta\Gamma^\mu(p',p) = -\frac{ie^2}{(2\pi)^4}\int \frac{d^2q}{q^2+i\epsilon}\gamma^\rho S_F(p'+q)\gamma^\mu S_F(p+q)\gamma_\rho \qquad \text{1.12}$$

Here $S_F(p'+q)$ is used to abbreviate the momentum-space propagator for the internal fermion lines. It is this expression that can be reordered into terms of γ^μ and P^μ and evaluated numerically in order to calculate the g-factor. Each electron-photon vertex contributes a factor 'e' to this expression.
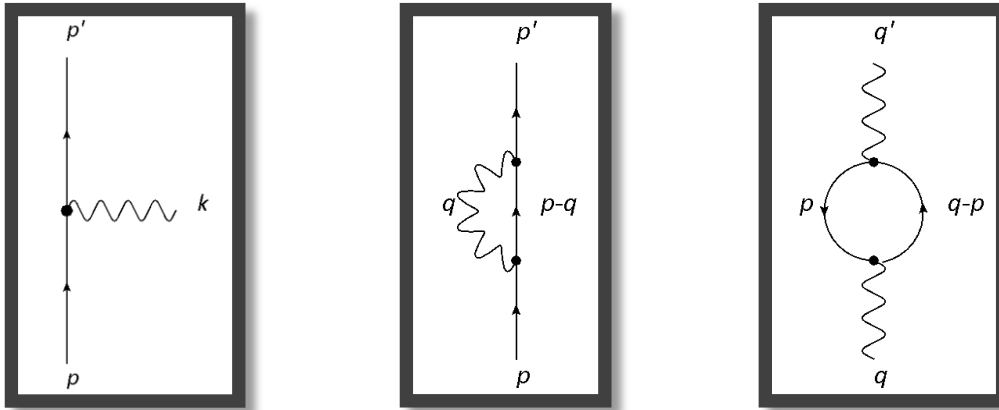
Figure 1.4: Feynman diagrams for 0th order interaction with the EM field (left), the "self-energy" correction (middle) term and the "vacuum polarisation" (right).

The factor e^2 in equation 1.12 is equivalent to the fine-structure constant ($\alpha = e^2/\hbar c$). Therefore, the diagram in figure 1.3 is said to be of order α. For completeness, figure 1.4 shows the other

6

diagrams of up to order α. These diagrams do not, however, contribute to the g-factor calculation. In a more complex diagram, a larger number of these vertices give rise to higher powers in α. These higher order diagrams typically involve more photon and fermion loops. Since $\alpha \approx 1/137$, these higher order contributions are suppressed and good results can be obtained from a limited number of diagrams.

1.3   Bound state QED
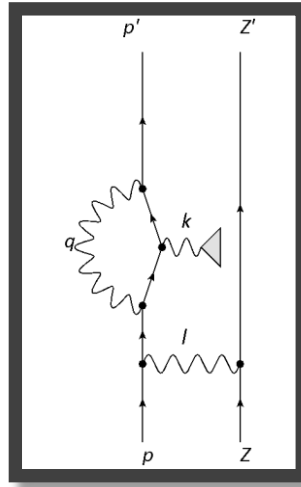
Figure 1.5: Vertex term with a single nuclear recoil photon. The triangle labels the interaction with the magnetic field, the photon is labelled 'p' and the nucleus is labelled by its nuclear charge Z.

When the electron is no longer a free particle but bound in the field of the nucleus, the spin angular-momentum is no longer an observable [10]. Instead, the intrinsic angular momentum combines with the orbital angular momentum into the total angular momentum *J*. In an external magnetic field, the Zeeman effect is described by the following interaction Hamiltonian:

$$H_{Zeeman} = -\boldsymbol{\mu_J} \cdot B$$

1.13

For a hydrogen-like ion with nuclear charge Z and assuming a point-like nucleus, the g-factor in the pure Coulomb potential is given by the Breit term:

$$g_j = \frac{2}{3}\left(1 + 2\sqrt{1 - (Z\alpha)^2}\right)$$

1.14

However, as with the Dirac prediction for the g-factor of the free electron, QED effects are not included. And, as the electron is bound to a nucleus and is thus no longer free, the influences of self-

energy and vacuum polarisation differ from that of free electrons. Also, the nuclear mass, size and structure are unaccounted for [10].

In the QED framework of section 1.2 the additional interaction of the electron with the nucleus introduces a second particle in the Feynman diagrams. An illustration of this is seen in figure 1.5. In these diagrams, the vertices associated with the photon 'q' still contribute a relative strength α. The nuclear recoil photon 'l' however, contributes a total factor $Z\alpha$ through its vertices. Higher order interactions between the electron and the nucleus are possible, such that the expansion in α is complemented by an expansion in $Z\alpha$. For large values of Z, $Z\alpha \rightarrow \sim 1$ and the expansion in $Z\alpha$ no longer converges. Figure 1.8 shows how for heavy nuclei the calculation for the first order in $Z\alpha$ easily differs from the result in all orders $Z\alpha$ by an order of magnitude.

Furry picture
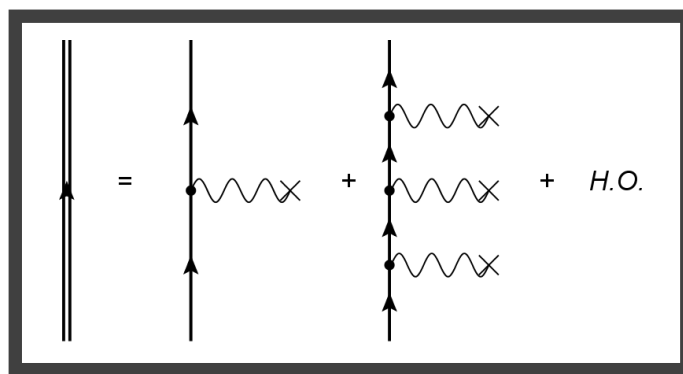
Figure 1.6: The bound electron propagator (double line) contains all the interactions between the electron and the nucleus, represented as a permanent point-like source (cross-shaped vertices). The double interaction is not allowed, and therefore not drawn [21]. Higher order terms (H.O.) are not drawn explicitly.

For bound states, these two particles stay together infinitely long and they can therefore interact arbitrarily often. This situation cannot be described by the summation of a few Feynman diagrams [18]. Because the nucleus is always much heavier than the electron, the problem can be simplified by considering the mass of the nucleus to be infinite compared to the mass of the electron. The bound electron can then be described by an electron in the permanent presence of a constant external potential. An infinite nuclear mass is assumed and a time-independent solution to the Dirac equation becomes possible. This is called the Furry picture [10]. Now the interaction with the field of the nucleus is included into the interaction Hamiltonian:

8

$$H_{int}(x) = \left(A_\mu^{nuclear}(x) + A_\mu^B(x)\right)j^\mu(x) \qquad\qquad 1.15$$

In this case, $A_\mu^{nuclear}(x)$ is the binding photon-field and $A_\mu^B(x)$ represents the external magnetic field and the magnetic field of the nucleus. The solutions to the Dirac equation now yield the bound-electron propagators, represented through a double line in the Feynman graphs (Figure 1.6). This propagator contains the interaction with the nucleus indicated by the expansion diagrams in figure 1.6. Methods exist to evaluate the bound-state propagator without explicitly evaluating the individual underlying diagrams [10, 22-25]. This means that e.g. the g-factor can be calculated in all orders of $Z\alpha$. Figure 1.7 shows the 6 diagrams contributing to the g-factor to order α. The next order (α^2) consists of 50 diagrams.
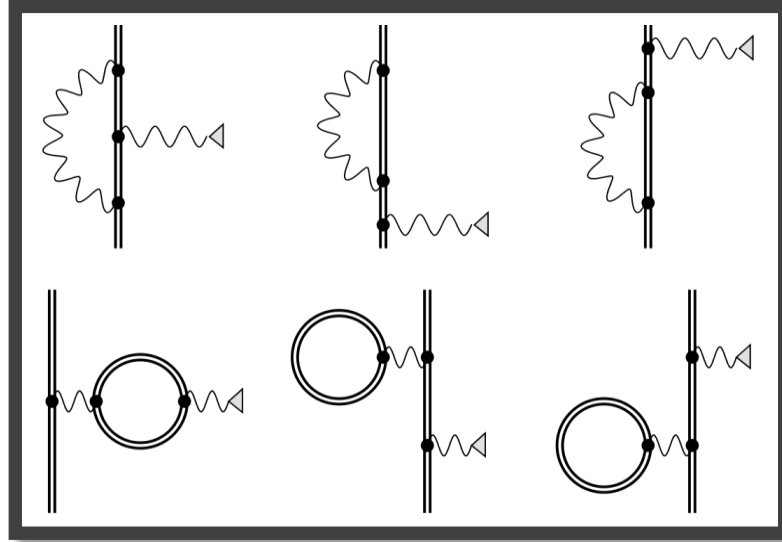
Figure 1.7: The Feynman diagrams representing the QED contributions of order α to the g-factor of the bound electron. Double lines indicate the bound-electron propagator. Triangles labels the interaction with the magnetic field, mediated through a photon (wiggly line). Self-energy diagrams are on the top and the vacuum polarisation is on the bottom row.

Beyond the Furry picture

Above the nucleus is assumed to be a point-like, infinitely heavy source. This is obviously only an approximation. The nucleus has a finite mass, a nonzero size and an internal structure that e.g. causes additional magnetisation effects [10, 24]. To correct for these deviations from the initial approximation, correction terms must be included in the calculation.

The effect on the interaction due to the finite nuclear mass, nuclear recoil, can be quantified with the ratio between the electron mass and the nuclear mass: m_e/M_Z. As, for all nuclei, this ratio is much smaller than 1, the finite mass can be considered perturbatively. For H-like ions the recoil contribution up to orders $(Z\alpha)^2$, α and $(m_e/M_Z)^2$ to the g-factor were obtained in the 1970's by Grotch [26, 27].
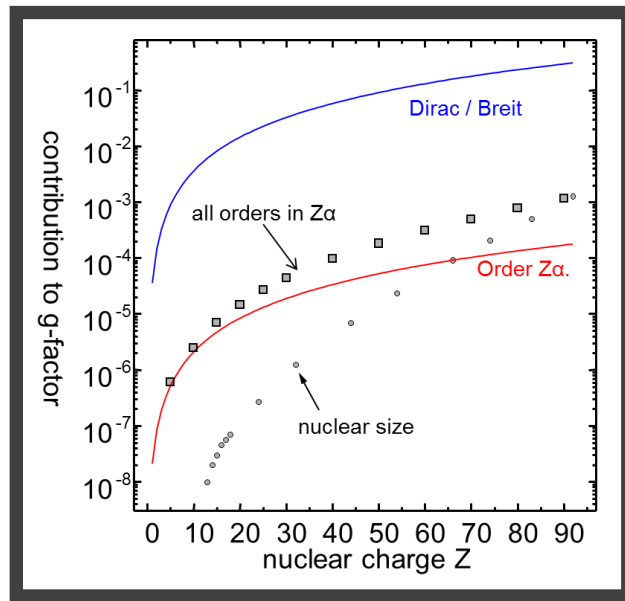
Figure 1.8: Contributions to the g-factor, given as (g-2) as a function of nuclear charge. The Breit term (blue) is given by equation 1.14. Bound QED calculations for order Zα (red) and for all orders in Zα (Black squares) can be easily compared. The nuclear size effect (black dots) adds significantly to the g-factor for larger Z. The exact values and their errors are extensively tabulated in [10].

As figure 1.8 shows, the effect of the charge distribution on the g-factor is considerable for heavy ions. The nuclear size can be taken into account by replacing the point-like binding potential by the extended charge density of the extended nucleus [10]. The exact charge distribution within a nucleus is generally not known. Therefore, a general model for this charge density distribution can be used.

The nuclear structure influences the ionic g-factor in several ways. First, the nuclear magnetic dipole moment, as shown in equation 1.4, influences the predictions linearly. The nuclear magnetic moment is determined by the spins of its constituents. An exact prediction for this value is not possible and it has to be determined experimentally [10]. Section 5.1 presents a method in which this can be done with great precision for bismuth.

The nucleus is not a perfect point-like magnetic dipole. The influence of the nuclear structure on the ionic g-factor is called the "Bohr-Weisskopf effect". This effect describes the extended magnetisation

distribution of the nucleus. Models exist that can incorporate this effect into QED predictions. An overview of these is given in [10].

The nucleus can also absorb and emit virtual photons. The internal degrees of freedom inside the nucleus get excited and deexcited. This is called nuclear polarisation. The order of magnitude value of this process is the same size as or less then the QED corrections of order α^2.

In general, the *g*-factor calculation for H-like systems is an on-going process. More QED- and other corrections are added to the list every year. As the number of diagrams increases with every higher order of precision, these calculations become extremely laborious.

2   Penning Traps
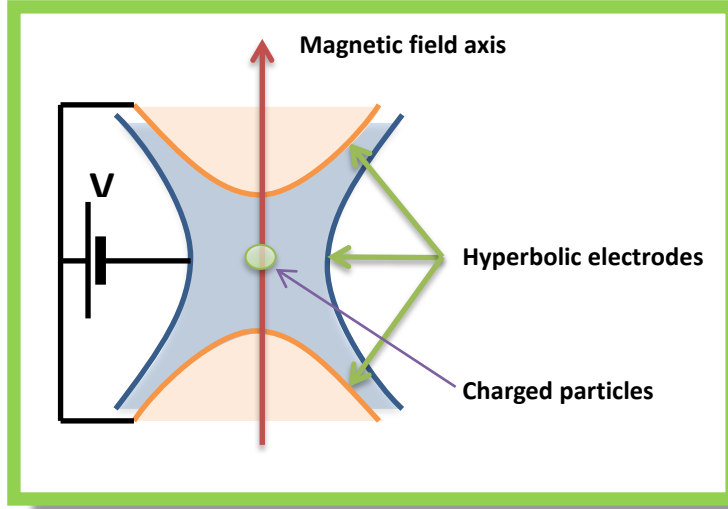
Figure 2.1: Schematic representation of an ideal Penning trap. the magnetic field (B) confines the particles in the radial plane. The electric potential (V) across the hyperbolic electrodes confines the particle in the axial direction.

Precision experiments on ions require precise control over the ions and detailed knowledge of the experimental boundary conditions. This can be achieved by trapping and storing a single ion or an ensemble of ions inside the combined electric and magnetic fields of a Penning Trap (Figure 2.1).

For the classical, ideal, Penning trap, the electric potential originates from a voltage applied between hyperbolically shaped electrodes [28]. In the ideal case, these electrodes extend ad infinitum.

A charged particle in motion inside the magnetic field of the Penning trap experiences a force, orthogonal to its direction of motion. Thus, the particle is 'pushed' into a cyclotron orbit and confined radially with respect to the magnetic field. Finally the electric potential confines the particle in the axial direction as well.

2.1   Electrostatics of the classical Penning trap

The ideal Penning trap has hyperbolic electrodes whose surfaces are given by[28]:

$$z^2 = z_0{}^2 + \rho^2/2$$

for the end-cap electrode and for the ring electrode by:

$$z^2 = \frac{1}{2}(\rho_0{}^2 + \rho^2)$$

The constants z_0 and ρ_0 are the distances from the trap centre to the end-cap and ring electrodes, respectively (Figure 2.2).
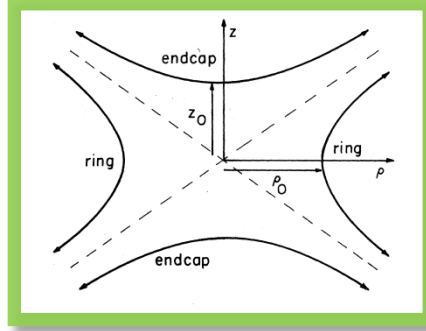
Figure 2.2: Schematic cross section of a classical Penning trap [28].

We define a characteristic trap size d as $d = \frac{1}{2}\sqrt{2z_0{}^2 + \rho_0{}^2}$. Now, with a voltage U_0 across the electrodes, the quadrupole potential induced is:

$$U = U_2 = U_0 \frac{z^2 - \frac{1}{2}\rho^2}{2d^2} \qquad\qquad 2.1$$

The hyperbolic shape of the electrodes results in a harmonic potential. Though not absolutely necessary for confinement, harmonicity is very important in many experiments. The harmonic potential results in a harmonic axial motion with oscillation frequency

$$\omega_z = \sqrt{\frac{qU_0}{md^2}}, \qquad\qquad 2.2$$

where m and q are the mass and charge of the particle. Thus, for an ideal trap, the axial frequency is independent of the amplitude of oscillation.

It can be easily seen that in reality the potential inside the Penning trap is not perfectly harmonic. It is necessary to put holes and slits in the electrodes for experimental access. Also, the electrodes do not extend infinitely long and there are machining imperfections and alignment errors. The imperfections

13

modify the original quadrupole potential of equation 2.1 with an additional anharmonic term such that:

$$U = U_2 + U_0 \Delta\varphi_0, \qquad where \; \Delta\varphi_0 = \frac{1}{2} \sum_{\substack{k=0 \\ even}}^{\infty} C_k^{(0)} \left(\frac{r}{d}\right)^k P_k(\cos\theta) \qquad 2.3$$

The main contributions to the modified potential now come from the $C_2^{(0)}$ and the $C_4^{(0)}$ coefficients. These coefficients are independent of the trap potential and trap size d. They can be calculated by solving Laplace's equation for the trap's geometry. In this expansion is a harmonic term, given by $C_2^{(0)}$. This term is the deviation of the harmonic strength from the ideal potential. However, it is convention to fully absorb the ideal potential into $C_2^{(0)}$. $C_4^{(0)}$ quantifies the strongest anharmonicity contribution [28]. It shifts the oscillation frequency dependent on the oscillation amplitude.

To reduce the anharmonicity, compensation electrodes with potential U_c can be added. Now, with U_2 absorbed into the series expansion, the potential is given by:

$$U = U_0 \Delta\varphi_0 + U_c \varphi_c \qquad\qquad 2.4$$

with (φ_c) given by the expansion:

$$\varphi_c = \frac{1}{2} \sum_{\substack{k=0 \\ even}}^{\infty} D_k \left(\frac{r}{d}\right)^k P_k(\cos\theta) \qquad\qquad 2.5$$

Equation 2.3 together with the expansion 2.5 shows that one can write:

$$C_k = C_k^{(0)} + D_k \frac{U_c}{U_0} \qquad\qquad 2.6$$

And for a careful choice of the tuning ratio, $T = U_c/U_0$, the C_4 coefficient can be adjusted to zero. At the same time, U_c influences the harmonic term through D_2. This means that the motional frequencies of the trapped particle in general change with U_c. Minimizing D_2 by choice of geometry reduces this influence. If $D_2 \approx 0$, the trap is called orthogonal.

With leading anharmonic terms cancelled out, the remaining C_2 still modifies the potential with respect to the hyperbolic trap (see equation 2.1). This leads to a change in the axial motion such that:

$$\omega_z = \sqrt{\frac{qU_0(C_2)}{md^2}} \qquad\qquad 2.7$$

2.2 Cylindrical Penning trap

The classical Penning trap configuration has a few disadvantages [29]. The hyperbolic shape of the electrodes is difficult to engineer and thus limits engineering precision and consequently the accuracy of the electric potential. The hyperbolic electrode structure hinders access to the insides of the trap. Charged particles have no natural way of entering the trap and experimental access with e.g. lasers is equally difficult. These issues can be addressed by replacing the hyperbolic electrodes by a cylindrical ring electrode and a pair of flat end-cap electrodes.
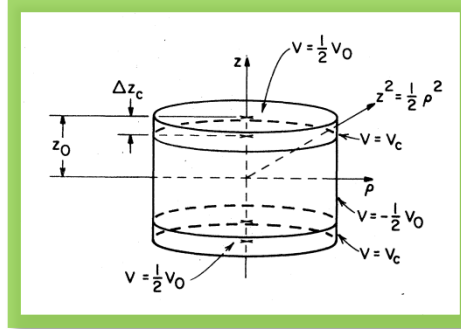
Figure 2.3: Electrically compensated cylindrical Penning trap [28].

With this configuration, the electric potential inside the trap is no longer harmonic. However, in the centre of the trap, for small oscillations, the potential is harmonic by approximation. Compensation electrodes, placed between ring and end-cap, can further improve the harmonic region of the trap (Figure 2.3). Expanded in Legendre polynomials, the potential near the centre of the trap is [30]:

$$V = \frac{1}{2}V_0 \sum_{\substack{k=0 \\ even}}^{\infty} C_k \left(\frac{r}{d}\right)^k P_k(\cos\theta) \qquad\qquad 2.8$$

C_k and d are still defined the same as for the ideal trap. The specific electrode geometry factors into the potential through the evaluation of the coefficients C_k. By a careful choice of electrode dimensions and potentials, the region where the harmonic approximation holds may be extended [28, 29].

At the same time, it is desirable to keep the trap orthogonal. This adds another constraint on the electrode dimensions. In total, the 5-pole cylindrical Penning trap has three parameters that can be controlled: trap length, correction electrode length and the correction voltage. These are enough to minimise D_2, C_4 and C_6. For ion motion inside this region, the frequency is again given by equation 2.7:

$$\omega_z = \sqrt{\frac{qU_0C_2}{md^2}}$$

The leading anharmonic contribution comes from C_4. This coefficient gives rise to a modification of the axial frequency by[28]:

$$\frac{\Delta\omega_z}{\omega_z} = \frac{1}{2}C_4\frac{E_z}{qU_0}, \qquad\qquad 2.9$$

with E_z the axial energy.

2.3   Single-ion motion inside a Penning trap

The force that a single charged particle experiences in the combined magnetic and electric fields of the Penning trap is of course the Lorentz force:

$$F_L = ma = q(E + v \times B) \qquad\qquad 2.10$$

This equation can easily be split up into an axial equation and a radial equation. The axial equation of motion depends only on the electric field:

$$m\ddot{z} = \frac{qU_0}{d^2}z \qquad\qquad 2.11$$

The solution of this equation is given as equation 2.2. The solution of the radial equation of motion is less straightforward since now both the electric field and the magnetic field contribute:

$$\ddot{\rho} - \omega_c\hat{B} \times \dot{\rho} - \frac{1}{2}\omega_z^2\rho = 0, \qquad where\ \omega_c = \frac{q|B|}{m} \qquad\qquad 2.12$$

ω_c is also called the free cyclotron frequency, it describes the motion a charged particle would undergo in the homogeneous magnetic field alone. With the electric field acting in the radial direction

as well, the equation of motion has two solutions. They are called the reduced cyclotron frequency (ω_+) and the magnetron frequency (ω_-):

$$\omega_+ = \frac{\omega_c}{2} + \sqrt{\frac{\omega_c^2}{4} - \frac{\omega_z^2}{2}}$$

2.13

$$\omega_- = \frac{\omega_c}{2} - \sqrt{\frac{\omega_c^2}{4} - \frac{\omega_z^2}{2}}$$
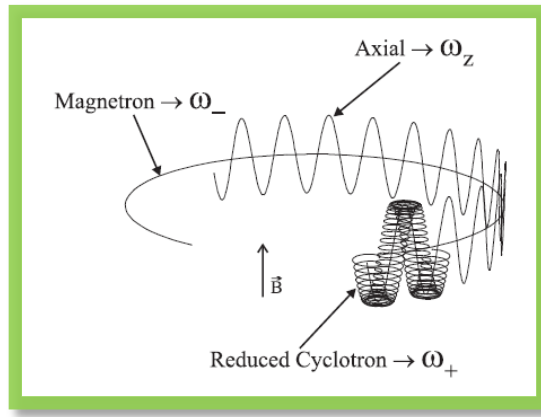
Figure 2.4: Orbit of a charged particle in a Penning trap [28].

The reduced cyclotron frequency is often called simply the cyclotron frequency. From equation 2.12 and equation 2.13 it follows that the three motional frequencies and the free cyclotron frequency are related through the 'invariance theorem':

$$\omega_c^2 = \omega_-^2 + \omega_+^2 + \omega_z^2$$

2.14

This theorem is very useful as it allows for a very precise and clean determination of the magnetic field that the particle experiences without electric field contribution[28, 31]. Finally, figure 2.4 shows the full motion of a charged particle within a Penning trap.

2.4 Detection of charged-particle motion

Charged particles in motion inside a Penning trap induce a small image current on the electrodes of the trap. This image current can be measured and thus the trapped particle's oscillation frequency can be measured non-destructively [33, 34]. We can approximate the ion trapped inside a Penning trap by

a test charge q moving between two infinite parallel conducting plates, a distance D apart. Then the current I induced in the electrodes is [35]:

$$I = \frac{q}{D}\dot{r} = \frac{q}{D}\omega r \qquad\qquad 2.15$$

Here r is the amplitude of the ion motion, and ω is the motional frequency of the ion. By determining the effective electrode distance, D, an electrode can be quantitatively compared to the infinite parallel plate conductor. For typical values, e.g. q the electron charge, the frequency around 1 MHz, D approximately 1cm and the radius below 1 mm, the current is of the order of a fA. Therefore, the signal needs to be amplified. This requires a low-noise boost of the signal's power and a high signal-to-noise amplifier. The first is typically done with at high-quality resonance circuit, while the latter requires a cryogenic FET amplifier (Figure 2.5).
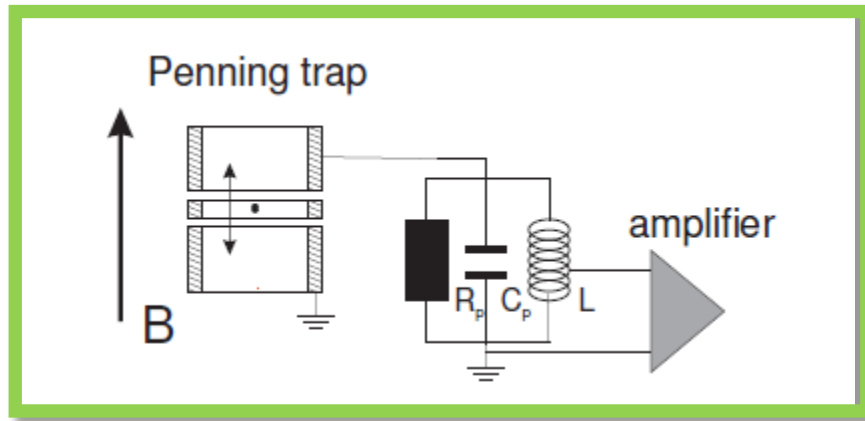
Figure 2.5: Ion detection scheme. On the left, the ion inside a trap, represented with three cylindrical electrodes. The signal is enhanced in a resonance circuit consisting of inductance L, and effective resistance R_p and parasitic capacitance C_p. Finally, a cryogenic amplifier boosts the signal. [32]

Resonance circuit

The ion-trap system can be modelled as an in-series RLC circuit [33, 34]. In this case, the motional frequency can be expressed in terms of a capacitance (c_{eq}) and an inductance (l_{eq}) such that $\omega_{eq} = 1/\sqrt{c_{eq}l_{eq}}$. The serial resistance of this equivalent circuit originates in the anharmonicity of the trapping potential and the possible ion-ion interaction in the case of multiple stored particles.

When a resistance is connected between both end-caps of the Penning trap (Figure 2.5), the current induced by the oscillation of the ion results in a voltage across the resistance. If the signal-to-noise ratio (S/N) is high enough, this voltage can be measured. A parallel resonance LC-circuit, on resonance

with the ion motion, improves this S/N. Such a circuit has a large resistance at its resonance frequency and thus creates a large voltage drop at that frequency. At any other frequency, the impedance is low and there the background noise is reduced. When at thermal equilibrium and $\omega_{eq} = \omega_{LC}$, the voltage in the tank circuit and the trap-equivalent circuit only differ by a phase-shift of π. As a result, the voltage at the resonance frequency drops to zero. There is a dip in the frequency spectrum at this frequency and hence this technique is commonly known as *dip detection*. Its line width is defined by the properties of the detector and the mass and charge of the particle [32, 34]:

$$\Delta v = \frac{1}{2\pi} \frac{R_p q^2}{m D^2} \qquad\qquad 2.16$$

If the ion is not at thermal equilibrium with the tank circuit, e.g. there is an external voltage driving the oscillation, the ion will deposit energy on the tank circuit. This will show in the frequency spectrum as a peak at the frequency at which the ion oscillates. This is commonly known as *peak detection*.

The tank circuit itself consists of the capacitance, C_T, of the pick-up electrodes, and an inductor L, connected to the electrodes. A parasitic capacitance C_P is added to the trap capacitance of the circuit. On resonance, with frequency ω_0, the effective parallel resistance is given by:

$$R_p = \omega_0 L Q = \frac{Q}{\omega_0 (C_T + C_P)} \qquad\qquad 2.17$$

Q is called the quality factor of the detection system. It quantifies the energy stored by the system with respect to the energy lost in the system per cycle. The Q-factor can be determined from the width of the resonance peak $\Delta\omega$, 3dB below the maximum, also known as the full-width-half-maximum.

$$Q = \frac{\omega_0}{\Delta\omega} \qquad\qquad 2.18$$

A high-quality resonance circuit can provide an effective resistance above 1 MΩ. This brings the voltage drop across the effective resistance of the resonance circuit due to the image current above 1 nV.

With the tank circuit acting as resistance, part of the energy of the ion dissipates in this resistance. The ion cools down to the physical temperature of the resistance, this is called resistive cooling. The cooling time constant is given by[34]:

$$\tau = \frac{1}{2\pi\Delta\nu} = \frac{mD^2}{R_p q^2} \qquad\qquad 2.19$$

Amplification

For a small axial frequency of $\omega_z/2\pi \approx 300\,kHz$, a 1 nV signal is still difficult to detect. To begin with, the signal needs to be transferred out of the Penning trap apparatus to the room temperature electronics. This makes it susceptible to both power losses and external noise sources. For that reason, there should be an amplification stage as close to the resonance circuit as possible. Typical amplifiers built for these detection systems are based on two stages of GaAs-field effect transistors (FET). Due to the small band gap of the material, they operate under cryogenic conditions [35-37]. The first stage provides a high voltage gain to lift the signal above the noise threshold. High input impedance matches the amplifier to the resonance circuit. The second stage typically is a source follower. It matches the output of the amplifier to the low 50 Ω impedance of the rf-lines [32].

2.5 Charged particle plasma inside a Penning trap

A large number of charged particles together we call a plasma. When different particle species are present, we call it a mixed plasma. In case the total positive charge is equal to the amount of negative charge, the plasma is neutral. In a Penning trap, ion species of opposite charge are typically stored besides each other in so-called nested traps. A plasma trapped inside a Penning trap has its own dynamics and offers new challenges and opportunities.

Dynamics

The Coulomb field of the particles counteracts the electrostatic trapping potential such that this Coulomb repulsion limits the maximum number of particles that can be stored inside the Penning trap.

Charged particles produce an electric field that modifies the trapping potential. Therefore, the simple harmonic picture is no longer valid. Figure 2.6 illustrates this for an arbitrary trap. Also, the ion cloud (partially) screens the potentials of the individual ions. When the size of the ion cloud is larger than the *Debye length* (λ_D), the plasma becomes correlated and collective properties become dominant.

$$\lambda_D = \left(\frac{\varepsilon_0 k_B T}{n q^2}\right)^{1/2} \qquad\qquad 2.20$$

T, n, q are the temperature, density and charge of the cloud, k_B is the Boltzmann constant and ε_0 is the dielectric constant. In this case, the density of the plasma is nearly constant up to its surface. There the density drops to zero within the size of the Debye length [38].
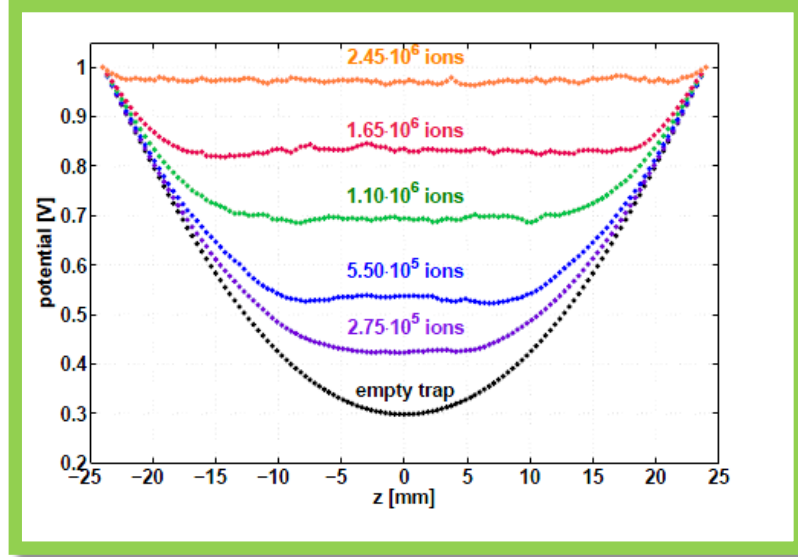
Figure 2.6: Electrostatic potential along the longitudinal axis for increasing number of stored particles. The initial potential is increasingly flattened until it completely cancels the confining voltage on the end caps. Small ripples occur as an effect of finite-size charges [39].

Inside the electric quadrupole potential of a Penning trap, the plasma is shaped like an ellipsoid. This ellipsoid rotates around its longitudinal axis. This is called the rigid rotor equilibrium [38]. In the rest frame of the plasma, the charges rearrange their relative positions such that an external electric field is shielded out. In the radial direction, the forces on the trapped particles are in equilibrium:

$$-\frac{mv_{rot}^2}{r} = qE_p + qv_{rot}B \qquad\qquad 2.21$$

In this equation, v_{rot} is the rotational velocity, r the radial position of the particle and E_p is the electric field caused by the plasma. If we take $\omega = v_{rot}/r$ as the rigid rotor frequency, then equation 2.21 can be written in terms of its motional frequencies:

$$-\omega^2 = \tfrac{1}{2}\omega_p^2 + \omega\omega_c \qquad\qquad 2.22$$

ω_p is called the plasma frequency. When written in the terms of equation 2.21 ($\omega_p = \sqrt{2qE_p/mr}$), the plasma frequency can clearly be seen as the individual particle interacting with the electric field of

the plasma. It can be seen as the speed with which the plasma restores itself when a single particle is displaced with respect to its equilibrium position.

While these frequencies describe the motion of the plasma as a whole, a plasma also undergoes internal motion. These plasma modes and their possible application are described in detail in section 4.4.

Electron cooling

When hot ions are brought into contact with cool electrons, the particles exchange energy with each other through Coulomb collisions. Thus, on average, the ions lose energy and cool down. In storage rings, electron cooling reduces the transversal emittance and longitudinal energy spread by merging a collinear electron beam with the circulating ions in a straight section of this storage ring[40]. In Penning traps, hot ions can be mixed with cold electrons or positrons to cool down the motion of the ions. Here both species are permanently stored during the cooling process [41-43]. The electrons stay cold through the emission of synchrotron radiation. Electron cooling is, therefore, a relatively fast method for cooling particles. After cooling, the light electrons can easily be separated from the heavy ions by collapsing the nested electron traps. In case positrons were used, briefly lowering and restoring the trap potential allows the light and fast positrons to leave the trap, while the heavy, and thus slower, ions stay behind.

3   The HITRAP Facility

Higher ionic states can be created through continuous bombardment of atoms or ions by energetic electrons. Thus the desired ionic state can be created. This "charge breeding" process may take place inside the ion trap itself or in a dedicated machine (EBIT/S or ECR), from where they are subsequently injected into the Penning Trap. Within the scope of this thesis, we are chiefly interested in highly-charged heavy ions such as hydrogen-like uranium, bismuth and lead. The binding energies associated with the innermost electrons are so high that charge breeding is very difficult, even in dedicated machines. Only the SuperEBIT produced a few U^{92+} ions. Another method is to create these ion species by in-flight stripping. This requires an accelerator facility.

Injection of ions produced at an accelerator into an ion trap requires that the ions are decelerated before. To this end the HITRAP facility has been constructed at GSI[44]. Its aim is to provide cooled and slow bunches of about 10^5 heavy and highly-charged ions for experiments.
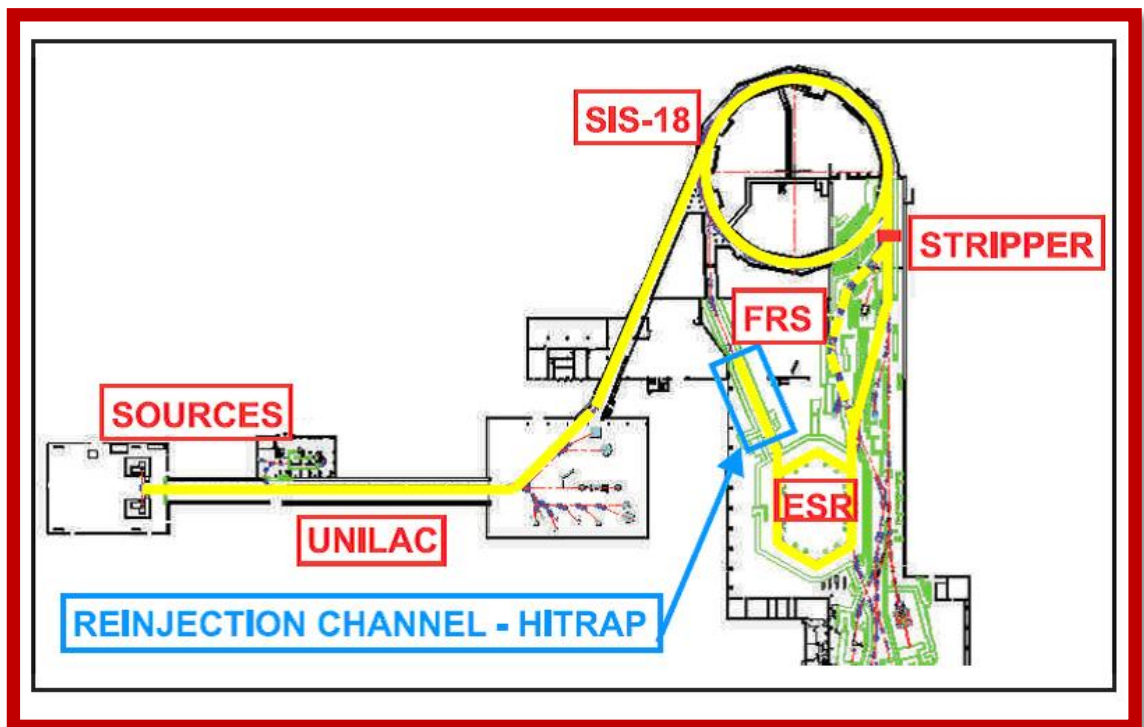
Figure 3.1: Overview of the GSI accelerator facility. The yellow line follows the path of the ion beam from the sources, through the Linac, SIS and ESR, to the HITRAP facility inside the reinjection channel.

3.1   Ion creation

At GSI (Figure 3.1), highly-charged ions (HCI) can be produced in several ion sources. The high charge states are obtained by shooting an accelerated beam through a thin foil. This is called 'stripping'. When the lowly-charged ions fly through the stripper foil, the ions lose their electrons by collisions with the material of the foil.

At GSI, heavy ions undergo two stripping steps: a first acceleration stage to 11.4 MeV/u in the UNIversal Linear ACcelerator (UNILAC) and consecutive stripping, of e.g. uranium, up to U^{73+}, and a second acceleration stage up to about 400 MeV/u in the synchrotron SIS-18 and stripping up to bare nuclei at a second stripper foil. From there on the ions travel through the Fragment Separator (FRS) which uses magnetic fields to select a specific charge state. Then the ions are transferred into the Experimental Storage Ring (ESR). The ESR is equipped with instrumentation for stochastic cooling and electron cooling which allows for the preparation of high-quality beams (small emittance)[44].
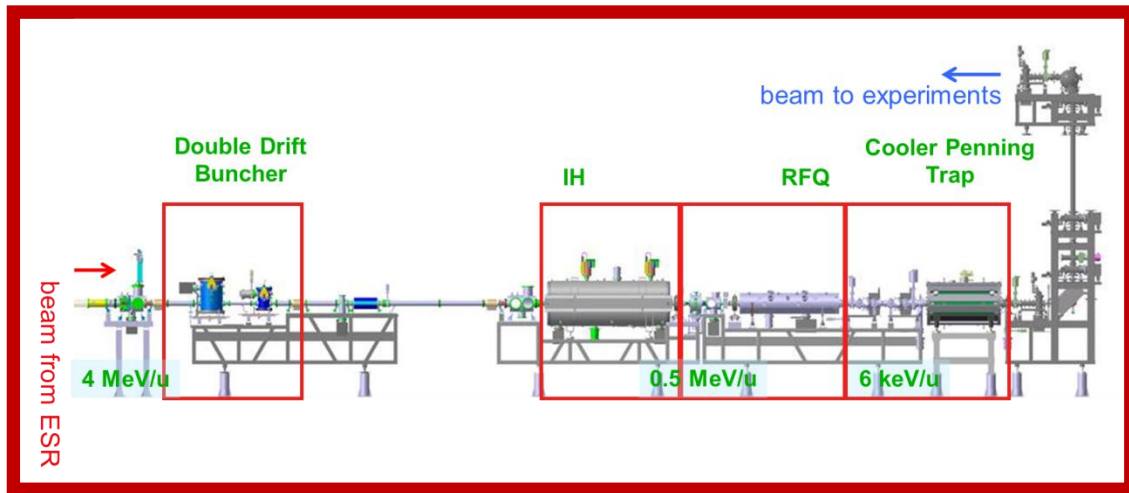
Figure 3.2: The HITRAP facility with the decelerating structures and the Cooler Trap below and, connected through a vertical beam line, experimental set-ups above.

3.2   Deceleration inside the IH and RFQ

The ESR delivers a beam of 4 MeV/u to the HITRAP facility for further deceleration and trapping. The HITRAP facility (Figure 3.2) is located in the former reinjection channel, a shielded tunnel formally housing a beam line for reinjection of ESR beams into the SIS-18. The first part of HITRAP consists of a Double Drift Buncher (DDB) [45], an Interdigital H-type (IH) linear decelerator [46] and a Radio Frequency Quadrupole (RFQ) [47].
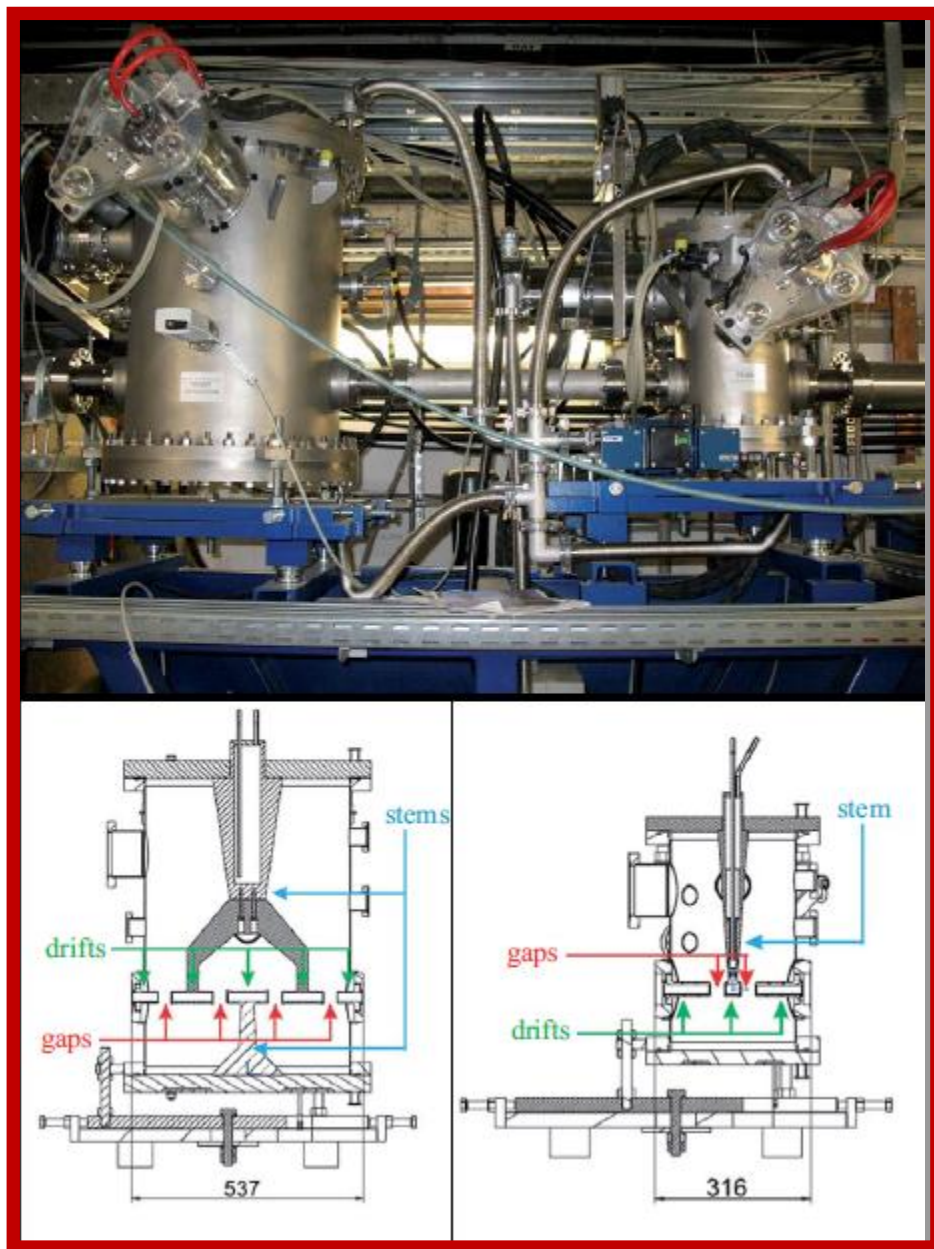
Figure 3.3: The Double Drift Buncher: The DDB inside the reinjection tunnel (above). A longitudinal view of both cavities (below).On the left the 4-gap 108 MHz cavity and on the right the 2-gap cavity, working at 216 MHz. All dimensions in mm. [45, 48]

Double drift bunchers

The beam, supplied by the ESR, is a 1 μs pulse. With a 9.2 ns period for the decelerating radio-frequency of IH-Linac this pulse can be treated as a DC pulse. The acceptance of the IH-Linac is between 10^0 and 15^0 out of the full 360^0 cycle. Therefore, the bunch is divided into ns bunches by the

DDB. This device consists of two RF cavities, one operating at 108.408 MHz, the other at 216.816 MHz. The DDB is shown in figure 3.3.

IH-Linac
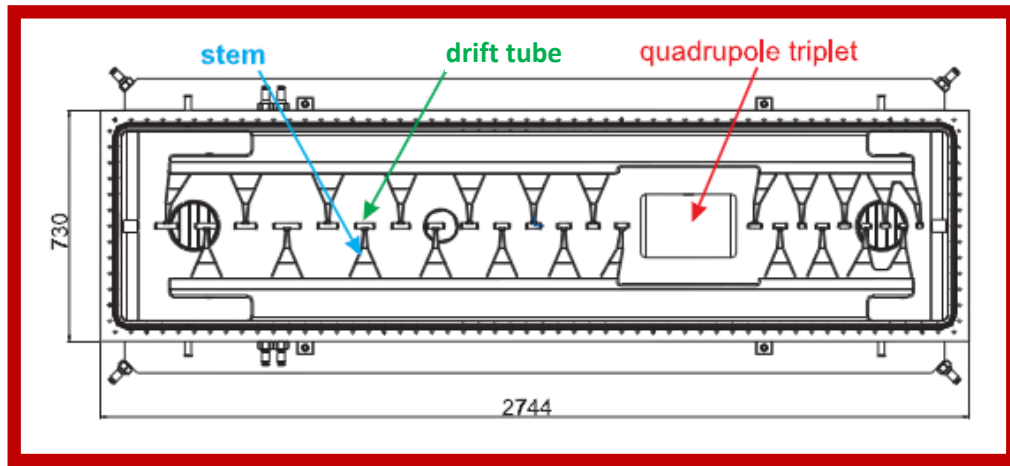
Figure 3.4: Schematic overview of the IH-Linac for HITRAP. It contains 25 drift tubes. The quadrupole triplet focusses the partially decelerated beam. All dimensions are in mm [45].

An IH-linac consists of a series of drift tubes in a resonant RF cavity. A charged particle, between the drift tubes, is subject to an accelerating or decelerating force. When the particle passes through the drift tubes, it is shielded from changes in the RF field. If the field changes polarity, exactly when the particle is shielded, there is a net force acting on this particle. This way an IH-linac can either accelerate or decelerate charged particles[49, 50].
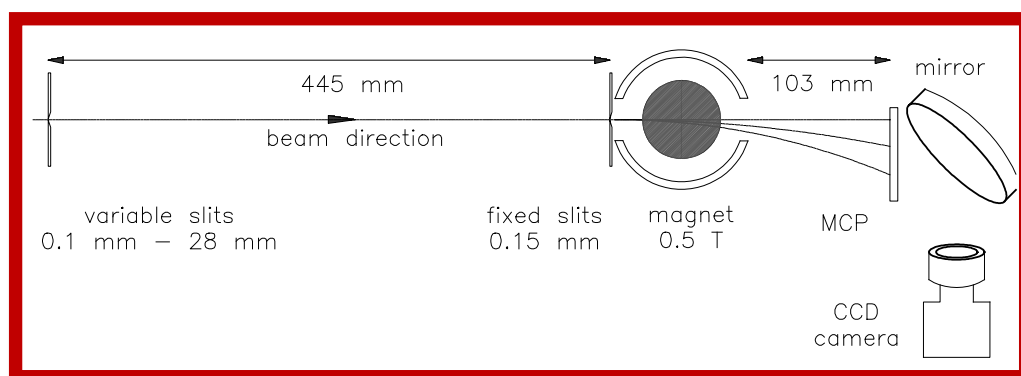
Figure 3.5: Schematic view of the energy analyser after IH-structure (The variable slit system was added in year 2011) [51].

Figure 3.4 shows the HITRAP IH-linac [46]. It consists of a 2.7-m long steel tank, drift tubes with 25 gaps and an internal quadrupole triplet lens for transverse focusing. It has been designed to decelerate 4 MeV/u ions with mass-to-charge ratio $M/Q \leq 3$ down to 0.5 MeV/u. The machine has been commissioned in dedicated beam times between August 2008 and October 2011.

During the commissioning process, several parameters had to be optimized. These parameters included: RF power in both the bunchers and the IH, relative phases between the two bunchers and between the bunchers and the IH, the input ion energy and the power distribution across the IH structure. Behind the IH, the beam can be detected on a micro-channel plate (MCP) with phosphor screen.

The beam leaving the IH contains a mixture of energies between the injection energy of 4 MeV/u and the fully decelerated energy of 0.5 MeV/u [51]. The energy mixture of each individual shot can be determined by a combination of moveable slits and a bending magnet, placed before an MCP. The schematic view of the energy analyser is shown in figure 3.5. The double slits create a narrow and straight beam. A 0.5 Tesla magnet bends the beam according to its energy. The beam is projected on top of the detector system. The combination of MCP, phosphor screen and CCD camera has single-particle sensitivity. The energy resolution of this set-up is 1% at 500 keV/u.
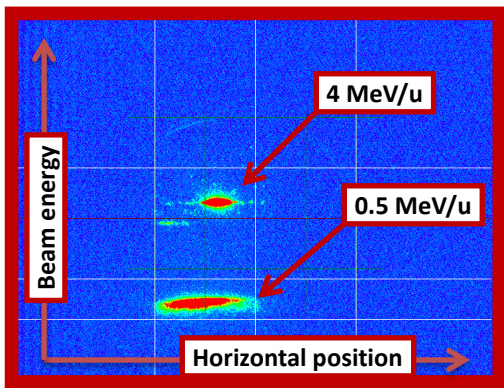
Figure 3.6: The original picture from the CCD camera of the energy spectrum of the ions after IH in false colour mode.
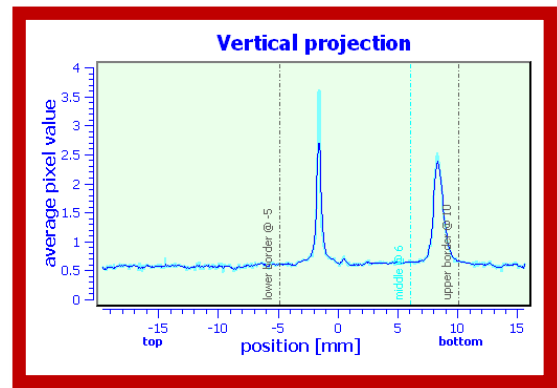
Figure 3.7: Vertical projection of the energy spectrum of the ions after the IH. The peak at -2 mm is the original 4 MeV/u beam while the decelerated beam results in a peak at the 'bottom' section.

Figure 3.6 and figure 3.7 show the energy spectrum of $^{136}Xe^{50+}$ ions after the IH, taken during the September 2011 run. Ions impinging on the MCP create an electron avalanche. As these electrons strike the phosphorous screen, light is emitted. The CCD camera records the intensity of the emitted

light. Figure 3.6 shows the CCD image. The intensity is shown with a coloured scale where red stands for a high intensity and thus a large number of ions. Blue reflects a low intensity and thus means an absence of ions. This picture shows two red areas. These correspond to two different ion energies, the original 4 MeV/u beam and the decelerated beam.

In figure 3.7 the CCD image is projected on the vertical axis. The area of each peak gives a measure of the number of ions. For this particular result, the ratio of the signal integrated in the two regions is 38% for the 4 MeV/u ions to 62% ions decelerated down to 500 keV/u. A more detailed analysis of the result is still under way.

Radio Frequency Quadrupole Linac

A radio-frequency quadrupole linac has 4 poles, or rods, that have a longitudinal modulation such that, when an RF-electric potential is applied to these rods, charged particles are confined in the transverse direction and decelerated or accelerated longitudinally at the same time [50].
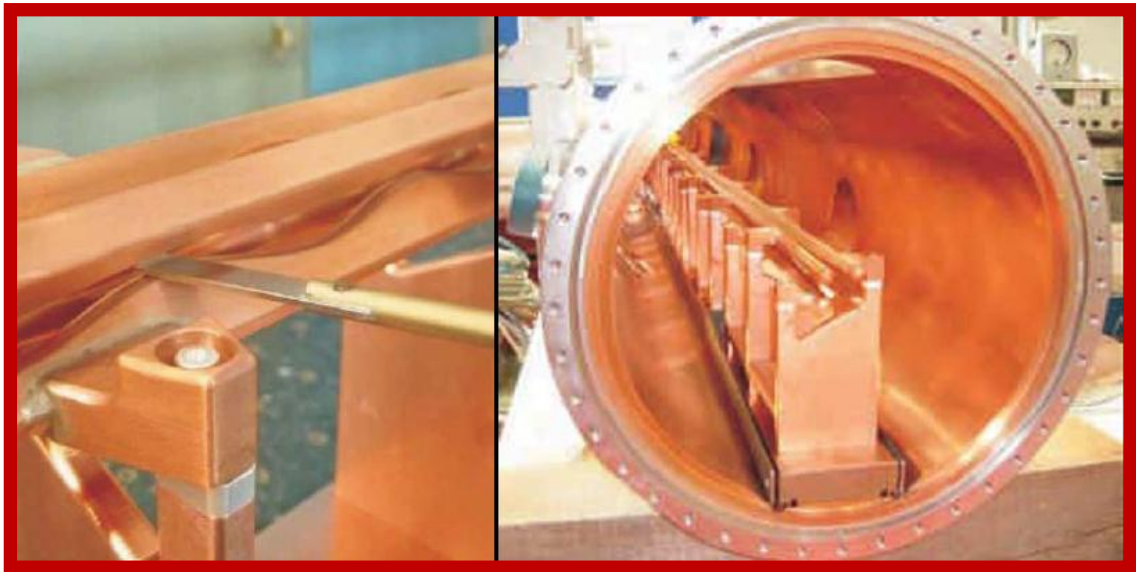
Figure 3.8: The RFQ is a 4 rod structure (right). The individual rods have a sinusoidally modulated shape [39].

Figure 3.8 shows photographs of the HITRAP RFQ. It has been designed to decelerate ion species with $m/q \leq 3$ from the IH output energy of 0.5 MeV/u down to 6 keV/u [52]. The longitudinal RFQ acceptance is 20° out of the full RF cycle, while the beam leaving the IH has a phase width of 45°. An additional 2-gap spiral rebuncher, placed between the IH and the RFQ, matches the 0.5 MeV/u beam to the RFQ acceptance. Between the RFQ and the Cooler Trap is a single harmonic debuncher. This

debuncher reduces the longitudinal energy spread after the RFQ from ±7% to ±4%. This will improve the trapping efficiency in the Cooler Trap.

To measure the energy distribution after the RFQ, an energy analyser, similar to the IH energy analyser but with lower magnetic field (0.1 Tesla), has been installed (Figure 3.9). The 0.1 Tesla magnetic strength can separate few keV/u ions from the beam onto the first MCP. The separation between the high energy fractions is then visible on a second MCP [51].

In April 2010, transport of a $^{86}Kr^{35+}$ beam through the RFQ has been achieved. However, deceleration did not yet succeed. Because the exact behaviour of the IH is still subject of study, commissioning of the RFQ with decelerated beam from the IH is difficult. Therefore the complete RFQ structure was moved to the Max Planck Institute for Nuclear Physics in Heidelberg where a Pelletron proton source provided a beam for commissioning.
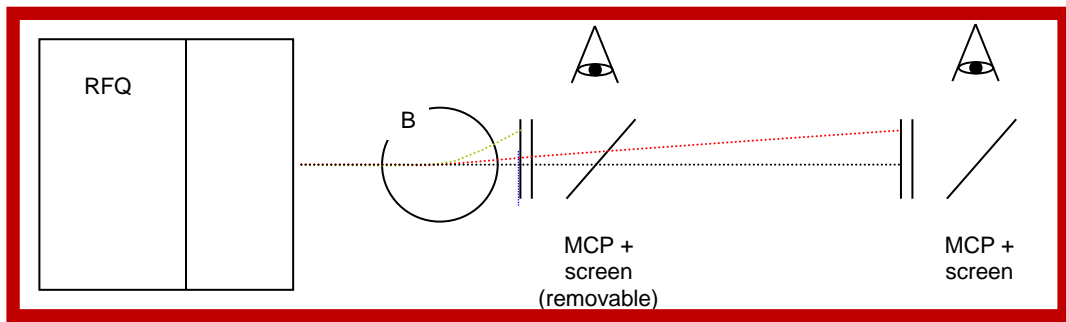
Figure 3.9: Energy analyser installed after the RFQ [51]. The beam comes in from the left. The first detector resolves 6 keV/u (green) beam. It is covered partly with a 5% mesh (blue dotted line) to suppress the high energy components. The second detector resolves the 500 keV/u component and the 4 MeV/u primary beam.

3.3   Cooler trap

Although now the ion beam has been decelerated as a whole, its internal energy spread is still high. Experiments require a well-defined ion bunch. Therefore, the decelerated ions will first be collected in a Penning trap, the Cooler Trap. The Cooler Trap will cool down the internal motion of the ion bunch to a temperature of 4 Kelvin. Then this bunch will be extracted from the Cooler Trap into the low energy beam line and supplied to several experiments. Chapter 4 deals with the Cooler Trap in more detail.

3.4   Vertical Beam line and experiments

Ions extracted from the Cooler Trap will be sent through a vertical beam line, seen in figure 3.10, up to the experimental platform. The transport energy of this section of the HITRAP facility will be 5 keV/q. A 90° double focussing dipole magnet will bend the beam upwards while at the same time clean the beam from any unwanted charge states incurred through charge recombination. From here on all other ion-optical elements will be electrostatic.
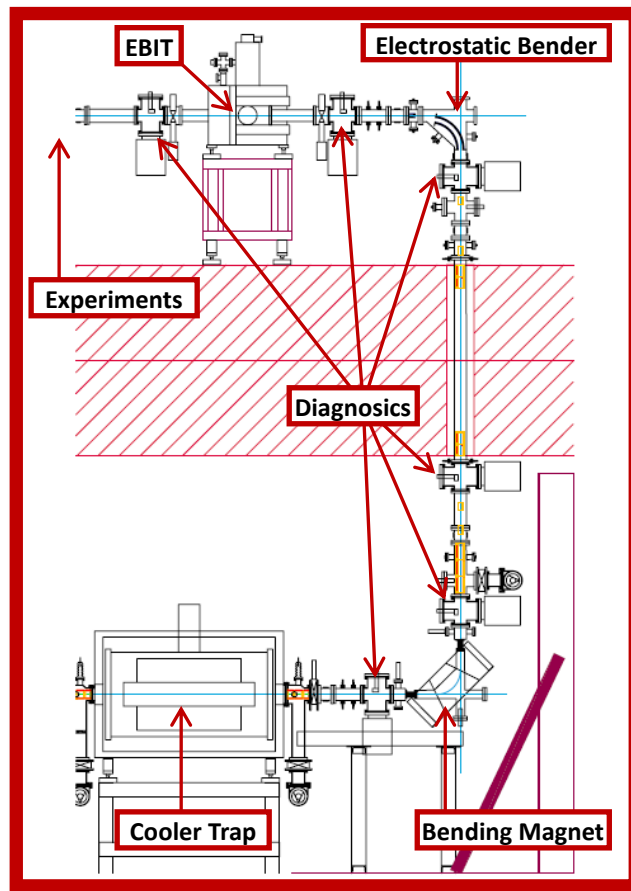
Figure 3.10: Vertical beam line. Ions will leave the Cooler Trap, the bending magnet will bend the beam upwards, after which it crosses the shielding. Then it is bent horizontally by an electrostatic kicker-bender. Additional ion optics such as lenses and kickers are coloured yellow.

The vertical beam line not only transports ions leaving the Cooler Trap. Electrons and light ions for testing will also be injected into the Cooler Trap through this beam line. It contains an electron source and magnetic coils that focus electrons and steer them into the magnetic field of the Penning trap. An additional test ion source can be mounted in this section as well. Chapter 4.1 discusses the injection of electrons and test ions in more detail.

On top of the experimental platform, a spherical electrostatic bender will bring the beam back into the horizontal plane. Here, on the experimental platform, several experimental stations will be serviced. Experiments besides the *g*-factor measurements include laser spectroscopy, mass-measurements, recoil reactions and surface reactions.

EBIT

An electron beam ion trap (EBIT) provides off-line ions to complement experiments based on ESR beam time. The EBIT can deliver medium-weight HCI up to Ar^{18+} and Xe^{46+} [53, 54]. These ions can be transferred in DC or in pulsed mode to several experimental set-ups. Also, they can be used for commissioning purposes. Through the vertical beam line, they can be sent down to the Cooler Trap as well.

Laser spectroscopy

The energy of the ground-state hyperfine splitting (HFS) scales with the atomic number (Z) as Z^3. For heavy and highly charged ions (Z > 60), the optical wavelengths allow laser spectroscopy. The lifetime of optically-pumped excited states scales with Z^{-9}. This strongly increases the fluorescence rate from magnetic dipole (M1) transitions. Therefore, in heavy HCI these M1 transitions can be probed. In heavy ions, nuclear effects play an important role. To first order, these effects can be ruled out by an accurate measurement of this transition in hydrogen-like and lithium-like ions of the same species. This allows the verification of bound-state QED effects on the atomic structure. In past experiments in storage rings [55, 56], the Doppler effect drastically limited the level of accuracy. In an EBIT [57-59], the poor signal-to-noise ratio limits the level uncertainty.

SPECTRAP is based on the former RETRAP [60] setup. A new electrode stack has a modified central ring to allow detection of the transition fluorescence. Rotating-wall compression [61] creates a high density of particles. The low ion energy reduces the Doppler shift and broadening. This will result in an expected accuracy that is three orders of magnitude better than for previous experiments [62].

Mass measurements

Particle masses are important parameters in physics. In particular, the knowledge of masses provides insight into nuclear and atomic structure. This information can be used to determine, amongst others, binding energies and reaction Q-values [63, 64]. At the same time, precise mass measurements provide input parameters to QED and the Standard Model [65].

The extended storage time offered by Penning traps and the high-accuracy frequency measurements these traps provide make them an ideal tool for mass spectrometry. The cyclotron frequency (Eqn. 2.12) depends directly on the mass of the ion. With the measurement of the cyclotron frequency for a well-known reference mass, m_{ref}, the mass of another particle, m_i, can be accurately determined through the relation:

$$\frac{m_i}{m_{ref}} = \frac{\omega_{ref}}{\omega_i} \qquad\qquad 3.1$$

Cyclotron frequencies can be measured destructively, using Time-Of-Flight (TOF), or by non-destructive detection of the image current induced by a single ion in the trap [66]. The latter method has achieved accuracies of the order of 10^{-11} on singly charged ions [67]. With the mass resolving power defined as:

$$R = \frac{m}{\Delta m} = \frac{\omega_c}{\Delta\omega_c} \qquad\qquad 3.2$$

It is clear that the precision of mass measurements is significantly improved for highly-charged ions. Due to the time necessary for ion preparation at HITRAP, these experiments are limited to stable nuclei or species with a lifetime of at least 20 s. A dedicated Penning trap experiment to measure masses with a relative precision of $\delta m/m < 10^{-11}$ is being built in Heidelberg [68].

Surface reactions

Another experiment at HITRAP will measure interactions between HCI and surfaces [69]. This set-up can measure electron emission as a function of charge state and energy of the ions and the properties of the surface [70]. The trampoline effect is the repulsion between the ionized surface and the partially recombined, but still positively charged, impinging ion [71]. This effect has, until now, never been observed. X-ray spectroscopy can be used to study the formation and decay of hollow atoms, i.e. multiply-excited states. This way, new information about level schemes in HCI can be obtained.

Collisions

A reaction microscope built up at MPI-K Heidelberg will study collisions between highly charged ions and a gas jet with the COLTRIMS (COLd Target Recoil Ion Momentum Spectroscopy) technique [72]. The set of detectors will track projectile, recoil ion and electrons, offering a complete reconstruction of the kinematics of the charge exchange processes, which dominate at low energy [73]. X-ray

spectroscopy of highly charged ions will be used in combination with this setup thanks to a series of solid-state detectors.

4   The Cooler Trap

4.1   Technical overview
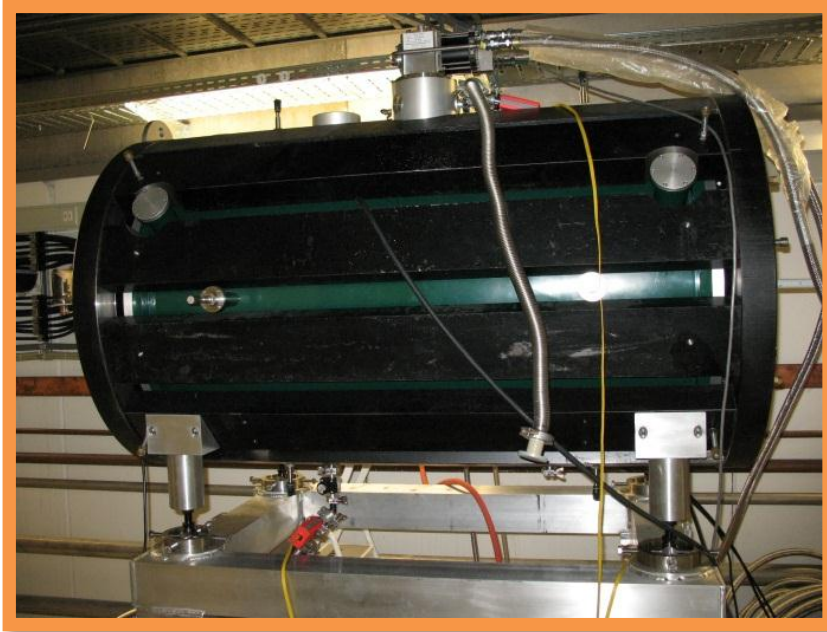
Figure 4.1: External picture of the Cooler Trap. The thick cables on the top lead to the cryo-cooler.

The Cooler Trap, seen from the outside in figure 4.1, is part of the HITRAP beam line. It resides at the end of the decelerating structures and it will capture and cool the decelerated hot ions. The Cooler Trap consists of a 6 Tesla superconducting solenoid magnet and an electrode stack with cryogenic electronics [39, 48]. The magnet system has a cold bore. This means that both the magnet and the bore of the magnet are cooled by the same cryo pump. This also means that the entire system must be cooled down before operation and heated up again afterwards. The vacuum system consists of two separate stages, see figure 4.2. The first stage is a pre-vacuum where the transition from room temperature to 60 Kelvin is made. The inner part, the second stage, mainly consists of the trap bore. It is separated by a heat shield and reaches 4.2 Kelvin. Inside the bore are the cryogenic electronics and trap electrodes. Inside the bore a high vacuum is required to prevent charge pick-up by the trapped ions.
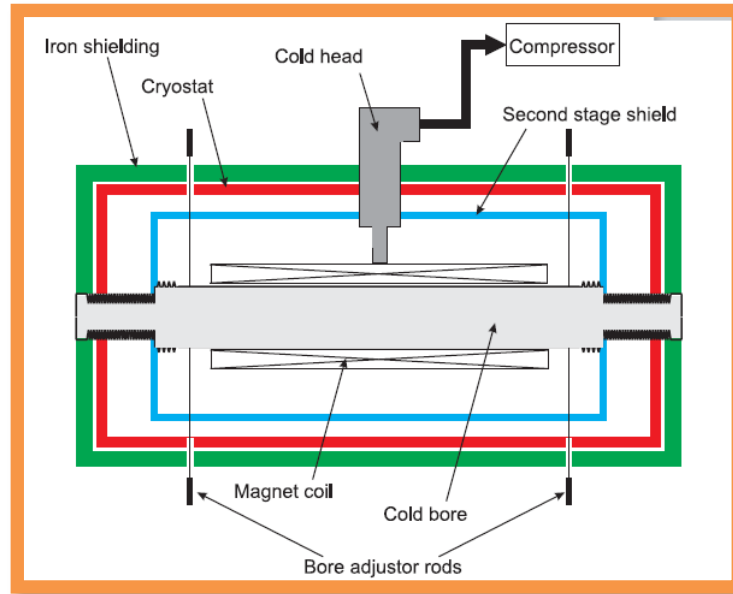
Figure 4.2: Schematics of the magnet system. The second-stage heat shield separates the transition between room temperature and 60K from the transition to 4 Kelvin. It also separates the two vacuum stages, with the experimental high vacuum inside and the pre-vacuum outside. Iron shielding passively shields the magnetic field.

Figure 4.3: The electrode stack with mounted electronics box. Kapton coated wires connect the electrodes with the electronics box and feedthroughs to the connection system.

The design of the electrode stack and the electrostatic characterisation was the topic of Giancarlo Maero's thesis [39]. The electrode stack, shown in figure 4.3 and figure 4.4, consists of 25 electrodes. The two outermost electrodes are electrically grounded. Next to those sit the end-cap electrodes. These are switched at high voltage for bunch trapping. Between the end-cap electrodes are the 21 inner electrodes. These carry a potential of up to 200 V and can be used for bunch cooling and manipulation. Three of these electrodes are split in two or more sections for azimuthal detection and

excitation or rotating wall compression. On top of the electrodes is the electronics box which houses the cryogenic electronics discussed below.
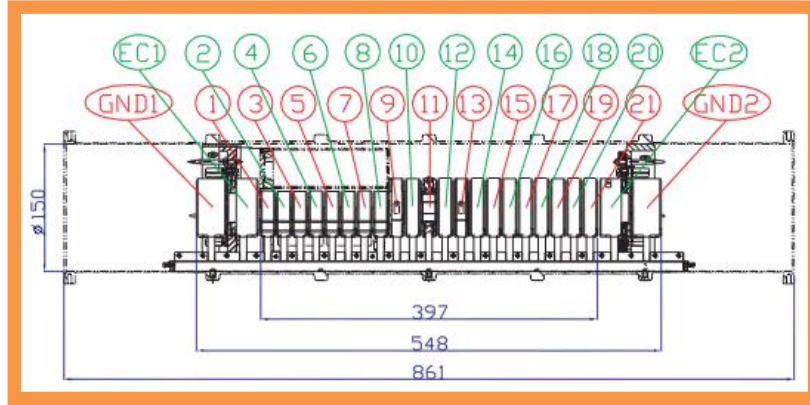
Figure 4.4: Schematic drawing of the Cooler trap electrode stack. End cap electrodes (EC1 & EC2) and ground electrodes (GND1 & GND2) are as labelled. All other electrodes are numbered from 1 to 21. Sizes are in mm.

The connection system

Figure 4.5: Outer electrode with feedthroughs for the electrode connections.

Because trapping the ion beam requires a high voltage, the entire electrode stack, as well as the cryogenic electronics and the connection system float at high voltage. The connection system connects the electrodes to the power supplies inside a high-voltage cage close to the beam line. It must be shielded from the ground potential of the magnet system and also crosses the two temperature transitions between the cryogenic trap and outside world. Finally, it must provide a

stable ground to the electronics inside and carry the ion and electron signals to the room-temperature electronics.
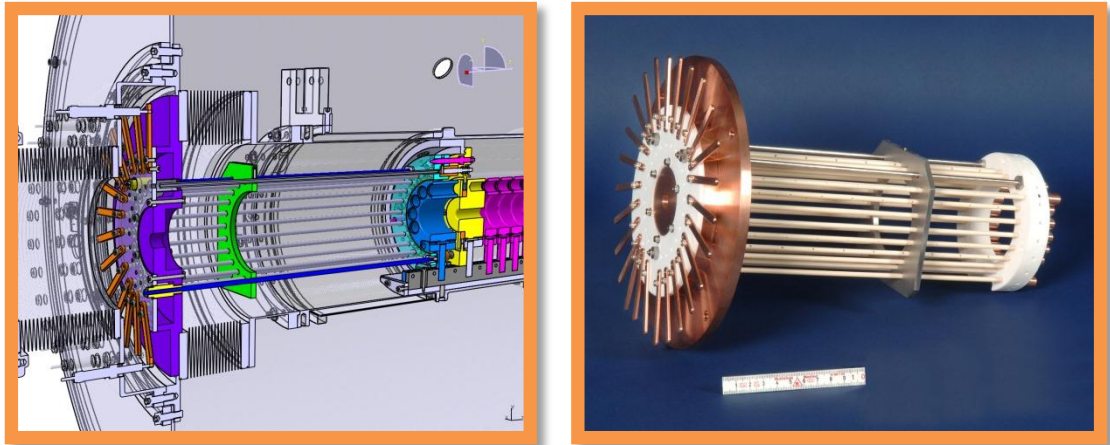
Figure 4.6: the connection plug. The in situ schematic drawing is on the left and a photograph on the right. The connection plug connects the cryogenic electrode stack (blue, yellow and purple) with the feedthroughs in the 60 K heat shield. The connection plug consists of a ceramic (light blue) ring that connects to the electrodes, constantan cables (dark blue) protected by ceramic tubes and a copper mounting ring (purple) with copper 'fingers' (orange) to connect with the feedthroughs in the heat shield.
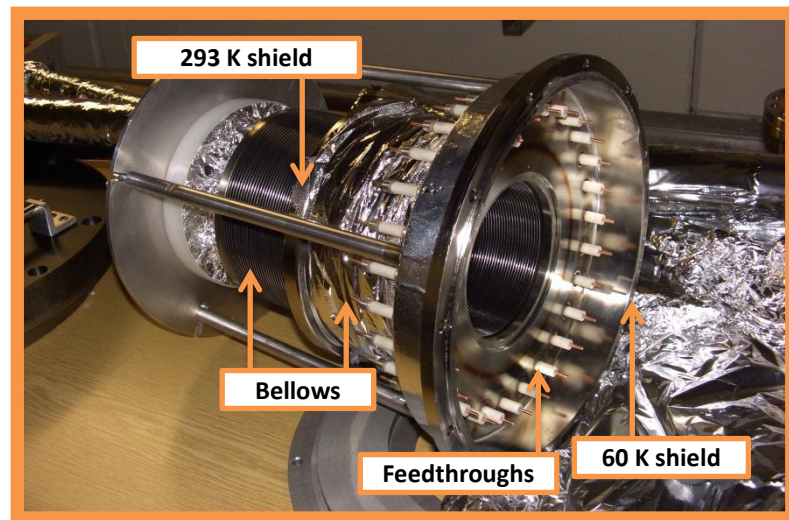
Figure 4.7: Heat shield with electronic connections. Important components are labelled.

Both the electrodes and the electronics box are connected to a series of feedthroughs in the outer electrodes. These feedthroughs are shown in figure 4.5. They connect to the connection plug shown in figure 4.6 that bridges the first temperature gap between 4 Kelvin and 60 Kelvin. The electrical contact

of the connection plug is made with a material with small thermal conductivity. On the 60 Kelvin side they are connected to strips of metal, called 'fingers', that act as an interface for the connection to room temperature through a heat shield in figure 4.7.

This heat shield (Figure 4.7) separates the trap vacuum from the pre-vacuum of the magnet system. It consists of three flanges and two bellows in between. The first flange contains feed-through pins that connect to the 'fingers' of the connection plug. Then a bellow makes the transition from 60 Kelvin to room temperature, and the second bellow and third flange connect the Cooler Trap to the rest of the beam line. From the heat shield, high-voltage insulated cables connect to flanges in the magnet barrel and the outside world.

Electronics box

The electronics box, shown in figure 4.3, houses the cryogenic electronics. Currently only the axial detection circuit has been installed. A detection circuit for the ion cyclotron motion, noise filters and amplifiers for the electron signal are foreseen. The electronics are described in more detail in section 4.3.

Beam line
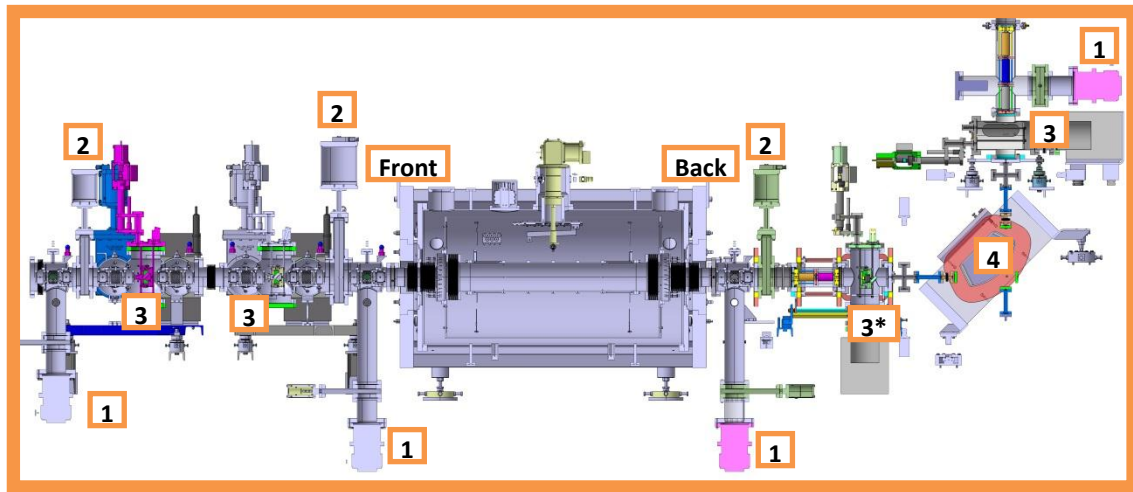
Figure 4.8: The HITRAP beam line before and after the Cooler trap. On the left the beam line starts where the RFQ ends. On the right the beam is bent upwards in the bending magnet (4). Turbo pumps (1), shutter valves (2), and diagnostic chambers (3) are labelled.

Figure 4.8 shows an overview of the beam line around the Cooler trap. Important components are labelled. The diagnostics chambers typically contain both a Faraday cup and a MCP with camera read-

out. The Faraday cup in the chamber after the trap (labelled with an asterisk) can be used from both directions.
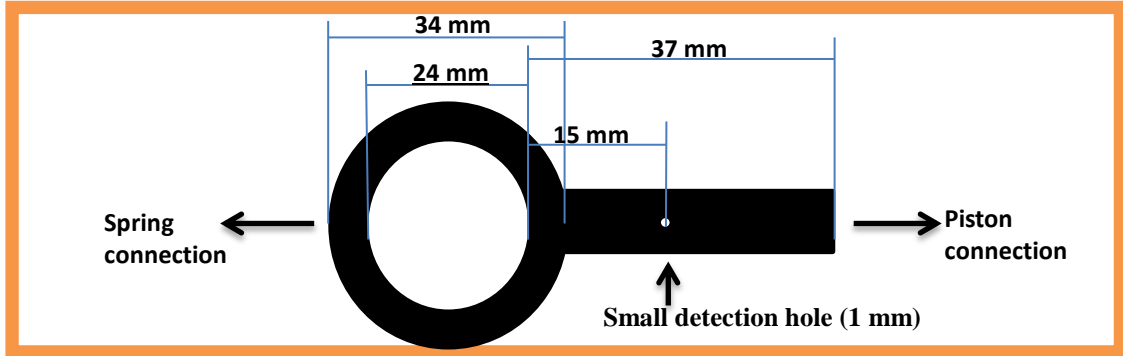
Figure 4.9: Schematic drawing of the Faraday cups FC1 and FC2 at the front and back of the Cooler trap. From one side, an air piston drives the detector into the beam line. A spring at the opposite side stabilises the construction. This assembly has two active areas: The large surface of the device itself and a little plate behind the small detection hole which should be in the centre of the beam when the detector is "in the beam". In the "out" position, the beam goes through the large central hole.
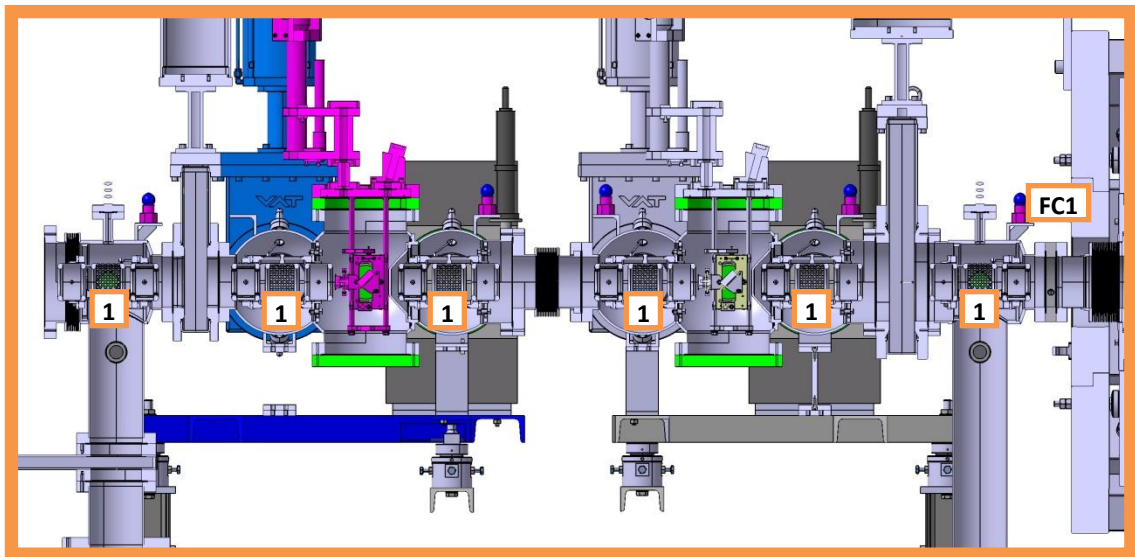
Figure 4.10: Beam line between the RFQ and the Cooler trap. This section contains several einzel lenses (1) with steerers to focus and steer the beam. At the entrance of the trap, a Faraday cup (FC1) can be brought into the beam line.

A more detailed view between the RFQ and the trap is provided in figure 4.10. Here the relevant ion-optical elements are labelled. 6 einzel lenses transport the beam into the trap. These lenses are split to allow horizontal and vertical steering. The Faraday cup (FC1) just before the trap can be used to

measure the electrons or ions leaving the magnetic field. This Faraday cup is shown and explained in figure 4.9.
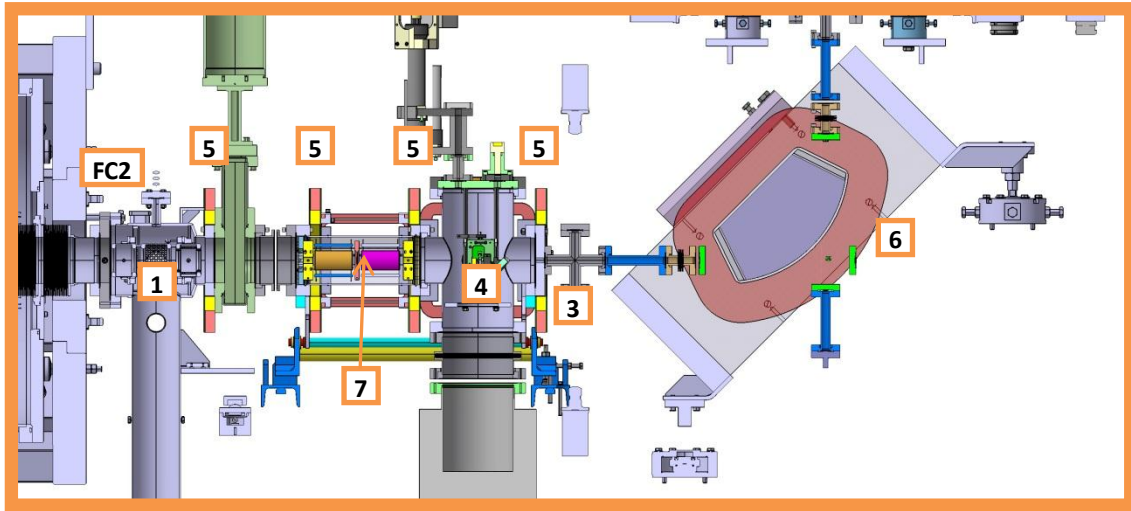
Figure 4.11: Beam line between the trap and the vertical section. This section contains an einzel lens (1) with steerers. Ion steering is also possible with an electrostatic quadrupole doublet (7). At the exit of the trap, a Faraday cup (FC2) can be brought into the beam line. This section also has a vertical slit system (3), a photo cathode (4) and magnetic coils (5) focus and steer the electron beam. An additional ion or electron source may be mounted after the bender (6).

The section after the trap is explored in figure 4.11. Here again a Faraday cup (FC2) is available. The einzel lens can be used for the extraction of ions, but also to inject ions from off-line sources. This section further contains an electro-static quadrupole doublet for ion manipulation. A photo-cathode creates electrons with kinetic energies of up to 100 V. They can be injected into the magnetic field, using magnetic coils for focussing and steering. Behind the bending magnet, a high energy electron source or a simple ion source may be mounted. The distance between FC1 and FC2 is approximately 1.7 meter. The electrode stack is exactly in the centre and has a length of 0.4 meter.

Injection

Charged particles can be injected into the trap from both sides. This allows for the trapping and cooling of ions from both on-line and off-line sources. E.g. ions can be produced in the EBIT on the platform and transported downstairs to the Cooler Trap is. Electrons can be produced by a photocathode close to the trap. The electrostatic ion-optics in the vertical beam line can be used for ions moving in both directions: away from the trap and towards the trap. Electrons are guided into the magnetic field with magnetic coils.

Charged particles should be injected into the strong magnetic field of the trap with minimum pick-up of transverse energy [74]. Especially electrons, with their low mass, are sensitive to the quality of the injection. The particles must be focussed such that they enter the magnetic field parallel to the magnetic field. In practice this means that there will be a narrow and parallel beam at the location of the Faraday cup on the back of the Cooler trap.
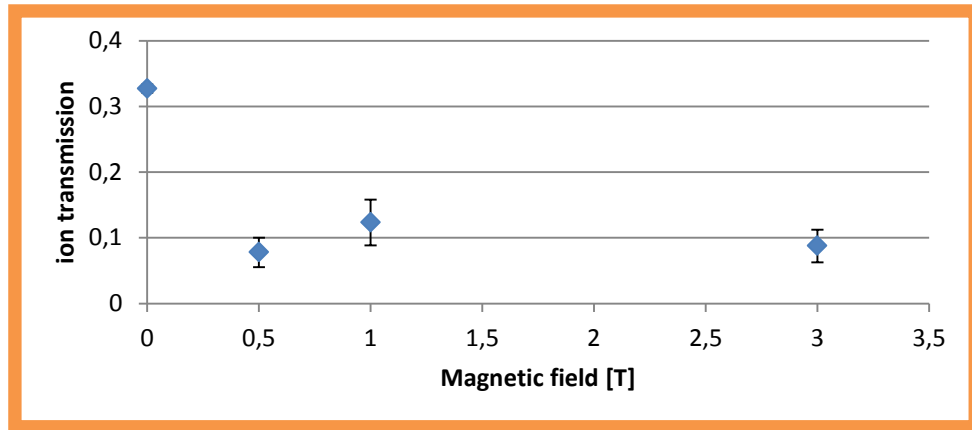
Figure 4.12: Transmission of 2 keV/q deuterons through the magnetic field of the Cooler trap compared to the emission current at the ion source. The errors largely come from the normalisation of the transmission.
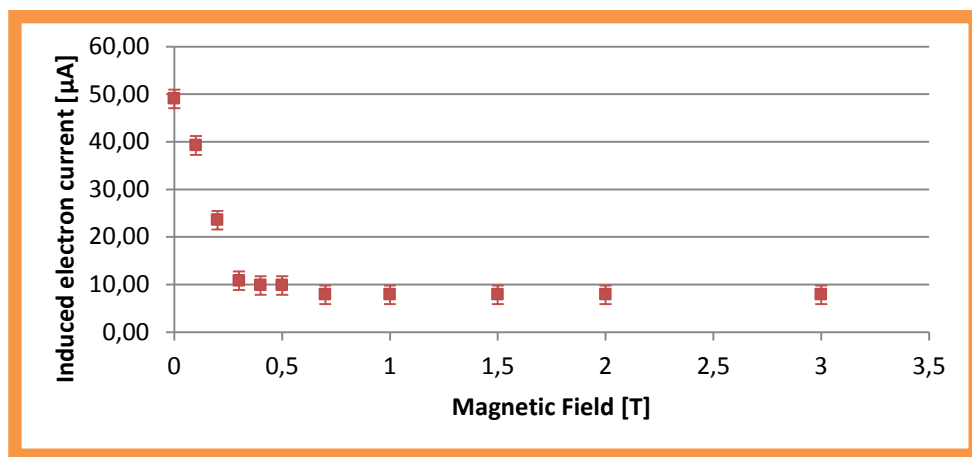
Figure 4.13: Induced electron current in FC2.

Using a Specs IQE 12/38 ion source, deuterons with an energy of 2 keV/q were injected into the magnetic field [75, 76]. A few data points are shown in figure 4.12. The signal of ions leaving the trap was measured on FC1. This signal was compared to the signal of the ions entering the trap, measured at FC2. The transmission was largely independent of the magnetic field strength. Without magnetic

field the transmission was much larger. This shows that good control over the ion injection is very important. During this test, only the focussing and steering of the ion source itself were used. Using the lens and quadrupole may improve these results.

Electrons were injected into the magnetic field as well. Figure 4.14 shows the magnetic field dependence for electron transmission through the Cooler trap. At low magnetic field, the electrons easily disperse, while a strong magnetic field keeps the electron beam focussed. The signal at FC1 was compared to the current induced in the ring of FC2 to calculate the transmission. The induced current is shown in figure 4.13. Below 0.3 Tesla the values for the induced current are relatively large while above 0.3 Tesla the induced current is independent of the magnetic field. It may be the case that the electrons are not yet completely focussed and the outer parts of the beam scrape the inside of the ring in the Faraday cup, depositing charges directly onto FC2. This behaviour is not fully understood and therefore no transmission is calculated for magnetic fields up to 0.3 Tesla.

For electrons with an energy of 30 eV and a 3 Tesla magnetic field, the measured transmission was 36%. In this case a total of $0.9 \cdot 10^9$ electrons per pulse was measured at FC1 compared to $2.5 \cdot 10^9$ electrons entering at FC2.
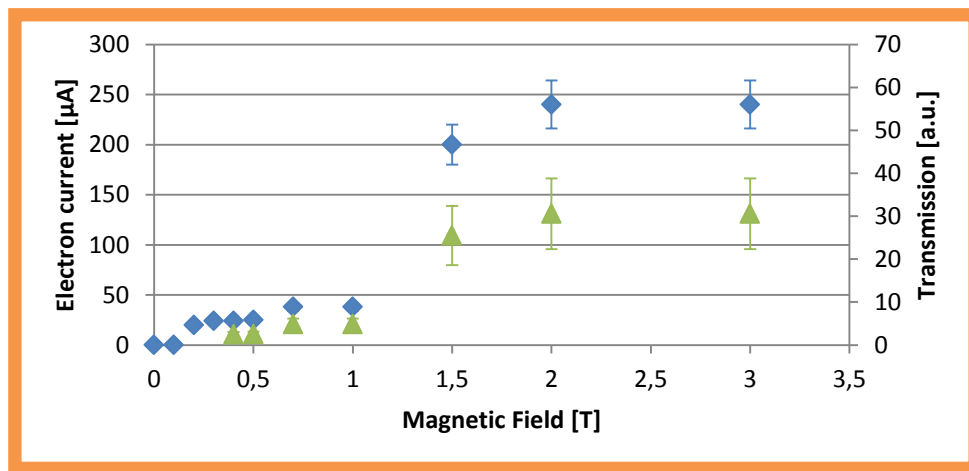
Figure 4.14: Electron injection into the magnetic field for 100 eV electrons. Blue dots give the signal of the electron current collected at FC1. The green dots give the transmission compared to the induced current at FC2.

42

4.2   Operation

Trapping of electrons

The first particles to be loaded into the Cooler Trap are electrons. Low energy electrons are produced at the photocathode. Using the steering coils, they are injected into the magnetic field, entering the electrode structure from the back. The last electrode, in this case the #1 electrode next to the front end cap is on a blocking potential, preventing the electrons from leaving the Penning trap. When the electrons are inside the electrode structure, also the potential at the #21 electrode, at the back, is raised, effectively trapping the electrons axially and blocking access to the trap for the electrons still outside. This requires accurate timing and fast switching of the electrode voltages. In this case, the trap was closed 5.4 µs after the electrons were created at the photocathode.

Electron energy [eV]	Velocity [m/s]	TOF 1 [µs]	TOF 2 [µs]
100	6×10^6	0.28	0.06
80	5×10^6	0.34	0.07
50	4×10^6	0.43	0.09
30	3×10^6	0.57	0.12

Table 4.1: Calculated electron velocities and time-of-flight between FC2 and FC1 (TOF 1) and the time between entering the electrode stack and leaving the electrode stack at the opposite end (TOF 2).

Table 4.1 lists the flight times for electrons with different energies. Signals were read out at a 300 MHz scope. This allows a 4 ns resolution. With this, a time-of-flight of 0.34 µs between FC2 and FC1 was measured. This is in good agreement with the calculations. For trapping, the electrons travel twice the length of the electrode stack. The timing of the voltage switch that closes the trap must be accurate compared to this time scale. A Quantum 9514 pulse generator created TTL timing pulses. These pulses have a resolution of 1 ns with a jitter of less than 400 ps. GSI-HV-switches deliver the DC-voltage to the electrodes. Their switching time was measured to be 200 V/µs. The time resolution and jitter of these switches is not known exactly. From experience the temporal accuracy is at least better than 50 ns which is good enough for electron trapping.

The Faraday cup at the front of the Cooler trap is used to detect particles leaving the magnetic field. While the 1st electrode is on blocking potential, no electrons are detected. By lowering this front electrode first, trapped electrons leave the Penning trap through the front and are detected on the Faraday cup. The timing of the extraction can be varied to measure the trapping time. Figure 4.15 shows the number of electrons trapped inside the Cooler trap for 2 different centre potentials. For both measurements, 60 eV electrons were trapped at -100 V with a magnetic field of 4 T. For the

second series, however, the central electrodes were raised to -50 volts, immediately after closing the trap. The first and last electrode remained at -100 V.
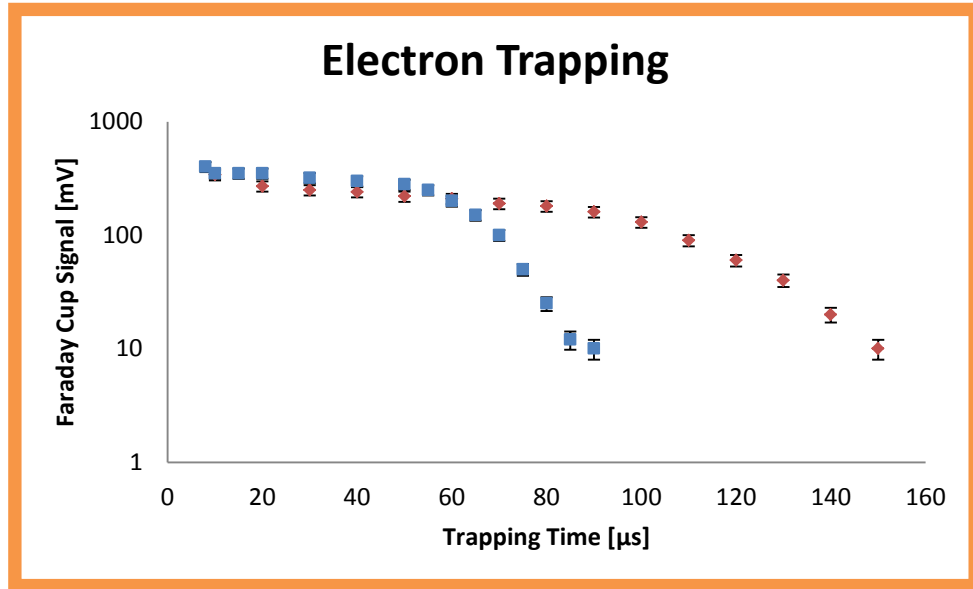
Figure 4.15: Electron trapping times inside the Cooler trap for a square well potential. For the blue markers the centre of the trap is at ground. For the red markers, the centre of the well is raised after trapping to a potential of -50 Volt.

Under ideal conditions, the trapping time for electrons is expected to be near infinite. For the initial tests at the Cooler trap, electrons could not be detected leaving the trap after roughly 100 µs. Several factors may contribute to reducing the measured trapping time.
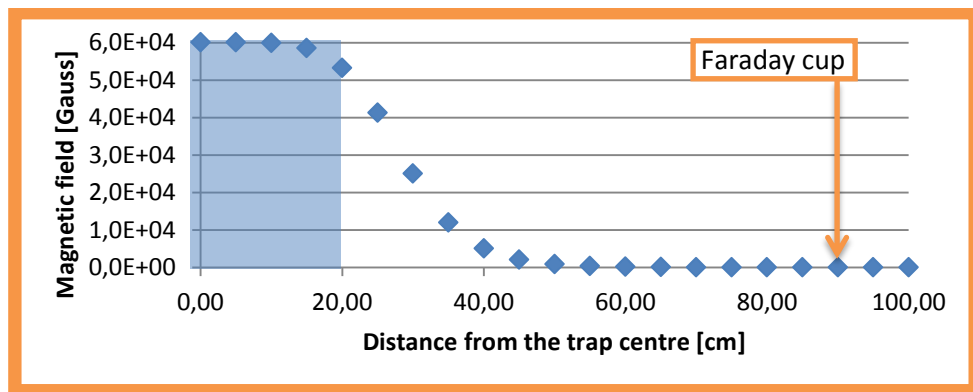
Figure 4.16: Magnetic field along the beam line, starting at the trap centre. The blue zone indicates the position of the electrode stack. The arrow gives the location of the Faraday cup. The magnetic field strength is less than 1 Gauss at this location.

The Faraday cups in front of and behind the Cooler trap are placed outside the magnetic field. Electrons, with their low mass, will follow these field lines as they enter and leave the magnetic field. If, while trapped, the electrons change their radial position, they will leave the magnetic field at an increased angle and miss the detector. This can happen if the magnetic and electric fields are misaligned with respect to each other. Alternatively, in this test, the electrons may not feel the electric potential from the electrodes while they are in the centre: the end cap electrodes are relatively far apart and all other electrodes are at ground potential. The electric field in this configuration is not as smooth as it would have been for a harmonic potential. As they approach the end caps, the electrons suddenly start to feel the electric field. At this moment they might change their magnetron radius. Lastly, the Coulomb interaction between the electrons could easily change their radial distribution.

Since the observed trapping time changes with the potential configuration of the trap, it is likely that the observed trapping time depends mainly on the electric field configuration. In the future the electric field must be properly aligned with the magnetic field. Also, a harmonic potential distribution inside the trap should be used.

Trapping of ions
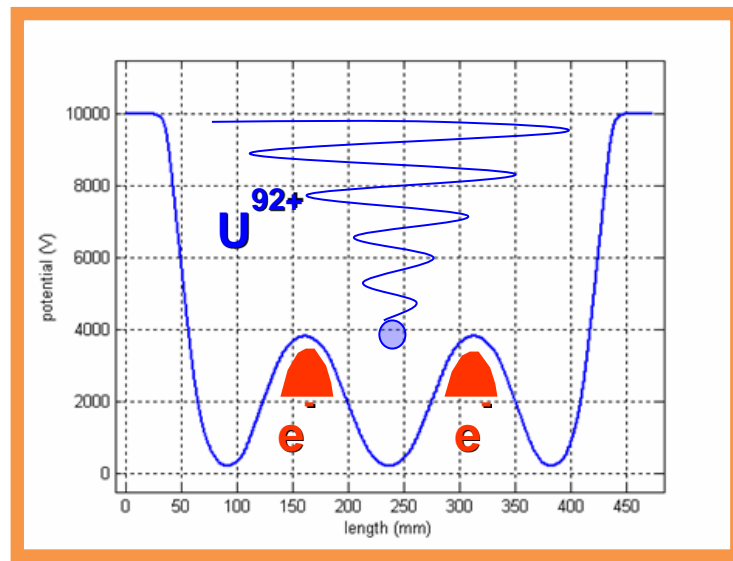
Figure 4.17: Hot ions are trapped by the electric potential of the Cooler trap. They gradually lose their energy against the cold electrons trapped inside a nested potential.

Ideally, the electrons will rapidly cool down to the wall temperature of 4 Kelvin through the emission of synchrotron radiation in the strong magnetic field. Then ions can be loaded into the trap both from the front and the back. From the front, highly-charged ions, coming from the HITRAP decelerator will

45

be trapped. From the back it is possible to receive ions from the off-line ion source behind the bending magnet or from the EBIT on the upstairs platform. On both sides of the trap is a set of electrostatic ion optics (lenses and benders) to focus and steer the beam into the magnetic field.

To trap the ions, one of the end cap electrodes will be at a high-voltage blocking potential. The other electrode will be switched to a high voltage after the ions enter the trap. The ions, coming from the decelerator, will have a kinetic energy of 6 keV/u [47]. For $^{209}Bi^{82+}$ this is the same as 16 keV/q. The required minimum trapping voltage is of the same magnitude. For this a high-voltage Behlke switch will be used [48].

Cooling

The trapped ions will initially have a kinetic energy of several keV/q. As the ions interact with the cold electron plasma, they will lose their energy and cool down, see figure 4.17. After some time, the ion cloud reaches thermal equilibrium with the electrons. When the kinetic energy of the ions approaches the energy of the electrons the rate of charge pick-up increases. Therefore, electron cooling is halted at roughly 10 eV and the nested electron traps are collapsed and the electrons released. At this stage resistive cooling against the cryogenic tank circuit takes over and cools the ions to 4 Kelvin [39].

Extraction

After cooling, the ions can be ejected from the trap in a single cooled bunch. In this case the back electrode is switched fast and all the ions leave together. Alternatively, the electrode can be ramped slowly. Now only the hottest ions can escape. This will create a quasi-continuous beam of ions. The ion optical elements behind the trap then guide the ions to the experimental stations.

4.3   Ion detection

The Cooler Trap will capture large numbers of ions and electrons. For the ions, the combination of high charge state and large particle number greatly enhances the signal strength picked up by the trap electrodes. This relaxes the requirements for the sensitivity of the detection electronics.

Ions, trapped inside the Cooler Trap, will be detected by their axial motion. The cyclotron motion can be measured as well to determine the mass-to-charge ration and thus, for a known isotope, their ionization state. Cyclotron detection is foreseen for the future. Therefore, only the axial image current, induced in the electrodes will be amplified with a resonant LC circuit and cryogenic amplifier. Additionally, the electron plasma will be studied by measuring induced currents in the trap electrodes.

The dynamics of the electron plasma is described below in section 4.4. Cryogenic amplifiers for these electron signals have been foreseen as well. 1.1

Axial detection circuit
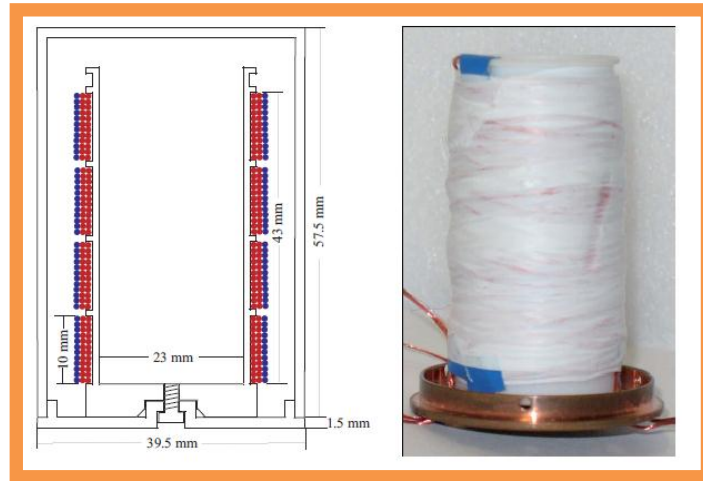
Figure 4.18: Axial detection coil for the Cooler trap [48]. A schematic drawing of the coil and the resonator shield is shown on the left. The primary coil (red) and the secondary coil (blue) can clearly be distinguished. The right-hand side shows a photograph of the coil without its shield.

The axial detection circuit was build and tested at room temperature within the scope of Stephen Koszudowski's PhD thesis [48]. The detection circuit has 2 main components: a copper coil and a cryogenic amplifier. Figure 4.18 shows the coil. Together with the parasitic capacitances in the circuit, the primary coil forms a resonance circuit. A secondary coil picks up the signal and is connected to the amplifier. The primary coil consists of 400 windings, made out of 50x0.04 mm diameter stranded wire. The secondary coil has 80 windings and it made out of the same material.

At room temperature, the resonance frequency for this coil was determined to be 463 kHz. A Q-Value of 87 was reached. At 77 Kelvin, these values changed to 428 kHz for the frequency and 136 for the Q-value. In the course of this work, the resonator shield has been goldplated to improve the Q-value and the original coil was replaced by a replica. Also the amplifier has been modified slightly (see below). The result of these changes is a frequency shift at room temperature to 400 kHz. The Q-value of the complete assembly, mounted inside the electronics box was measured at room temperature to be 120. In this case it is important to note that the electronics box provides electrical shielding and that the PCB base wiring improves the quality of the circuit a little as well.
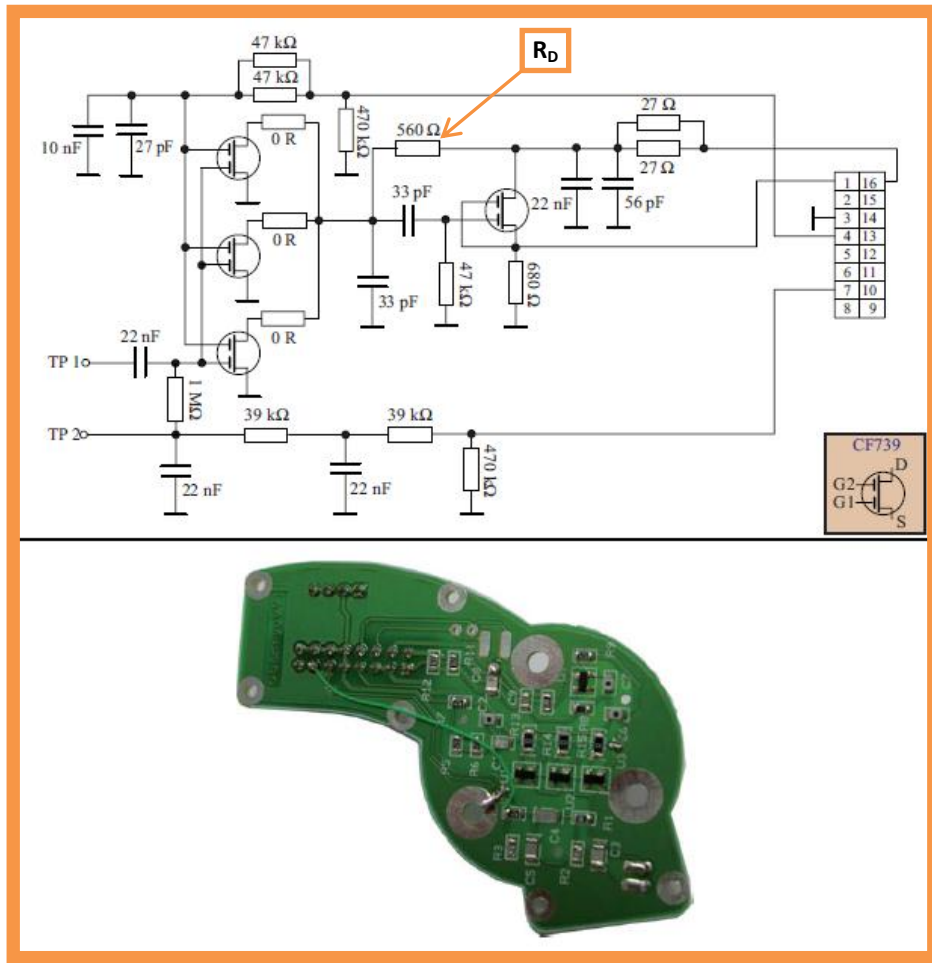
Figure 4.19: Axial amplifier diagram and circuit board [48]. The two ends of the secondary coil are connected to TP1 and TP2. The drain resistor (R_D) is labelled. All transistors are of the CF739 type.
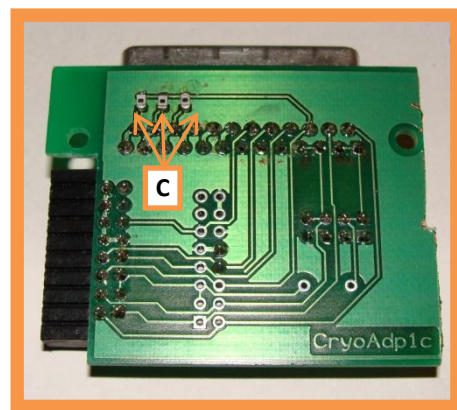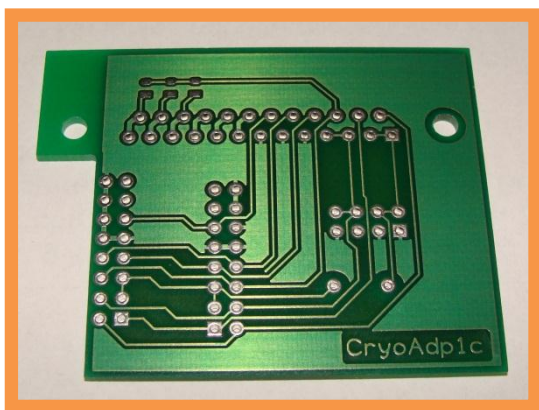
Figure 4.20: The unmounted (left) and mounted (right) interface board between the amplifier and the feedthroughs in the electronics board. The board on the right is mounted with the connectors and the coupling capacitors (C).

Figure 4.19 shows the lay-out of the axial amplifier. In the first stage, three CF739 transistors amplify the voltage signal of the ions. A second stage, consisting of only one FET, acts as a buffer stage. The input of the amplifier (TP1) is connected to the secondary coil. The other side of this coil is connected to TP2, which provides an effective grounding of the coil. Although optimum biasing voltages can be determined experimentally for different temperatures, it is important to notice that these voltages also depend on the connections to the power supply. In particular, the constantan connections from room temperature to the amplifier at cryogenic temperature have a non-zero resistance. In the presence of leak currents at the gates, the bias voltages will drop a little across this resistance. The same thing goes for the drain supply, where the voltage drop across the wiring is proportional to the drain current. Experimentally obtained values can only be used as guidelines and the amplifier will always have to be tuned *in situ*.
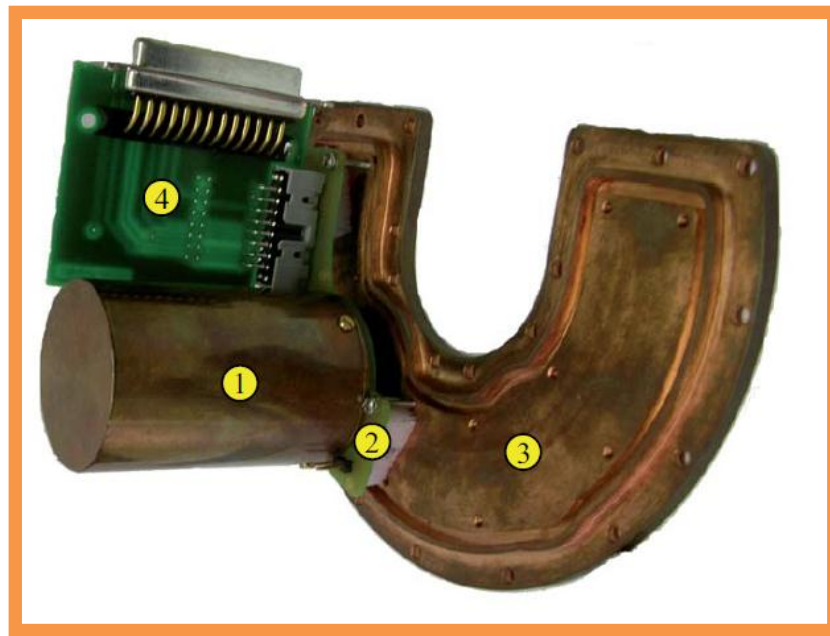
Figure 4.21: Assembled axial detection circuit [48]. The coil (1) is attached to the amplifier board (2). The entire assembly is mounted on the lid of the electronics box (3) for thermal contact and electrical grounding. An interface board (4) connects the feedthroughs of the electronics box to the amplifier.

The complete assembly of the electronics is shown in figure 4.21. The coil-amplifier combination is mounted on the lid of the electronics box. The amplifier is connected through an interface board (Figure 4.20) to a feedthrough in the electronics box. Here, the gate biasing, ground and drain supply are connected. Also the signal leaves through this connection to the connection system. The ion signal is picked up at electrodes 4, 10 and 16. These electrodes are capacitively coupled together on the

interface board. The capacitance of 47 pF has been chosen experimentally to optimise the signal transmission and quality of the circuit. The combined signal is fed into the primary coil.

Cryogenic tests

The axial detection circuit for the Cooler trap has now also been tested at liquid nitrogen (LN2) temperatures and at 4 Kelvin. For testing at the temperature of LN2, the entire amplifier, together with the resonator was submerged in a bath of LN2. For the 4 Kelvin test, the amplifier combination was firmly attached to the cold-head of a cryo-pump. This assembly was then cooled down to the required temperature and the relevant tests were performed. In the cryogenic tests the amplifier in combination with the coil was found to be oscillating. This behaviour could not be reproduced at either room temperature or in LN2. To stabilise the behaviour of the amplifier combination, the drain resistance (Figure 4.19) was increased from 560 Ω to 1 kΩ. After successful tests at room temperature and in LN2, the amplifier was tested at 4 Kelvin again. The results of this test are shown in figure 4.22. A region of stable operation has been found for a drain voltage of 3 Volt. However, the 3.9 V series shows that the amplifier still oscillates easily. The result of this oscillation is that the amplification and the Q-value are reduced dramatically. The resonance frequency was measured to be 457 kHz.
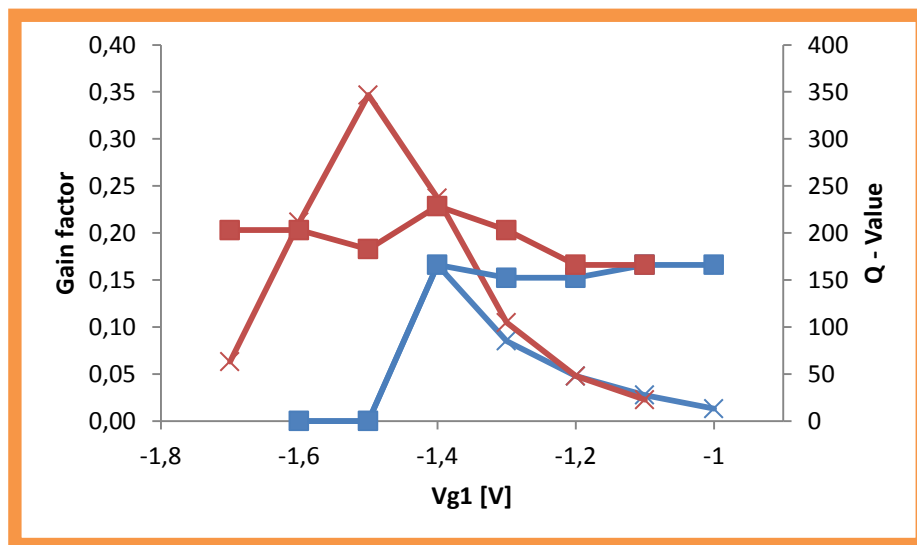
Figure 4.22: Amplifier response at cryogenic temperature with a 1 kΩ drain resistance for a drain voltage of 3 Volt (red lines) and 3.9 Volt (blue lines). Solid square markers are the measured Q – Value and crosses give the voltage gain of the amplifier.

As an alternative an amplifier board was prepared with only 1 FET in the first stage. Here the drain resistance was left at 560 Ω. Figure 4.23 shows the results. Although a larger Q-value is reached, this goes at the expense of amplifier gain. These results might be improved by increasing the drain

resistance here as well. For the moment, the original amplifier with increased drain resistance is used for the Cooler trap.

For the Cooler trap, a final Q-value of 800 is foreseen [48]. This allows a broad range for detecting particles while still having efficient cooling. The current copper coil has a Q-value of maximum 350 at 4 Kelvin. Additionally, when installed at the trap, the Q-value might deteriorate further on account of the additional wiring to the trap and interference caused by imperfect RF shielding inside the Cooler trap. If this will lead to cooling problems, a superconducting coil can be constructed to replace the copper coil.
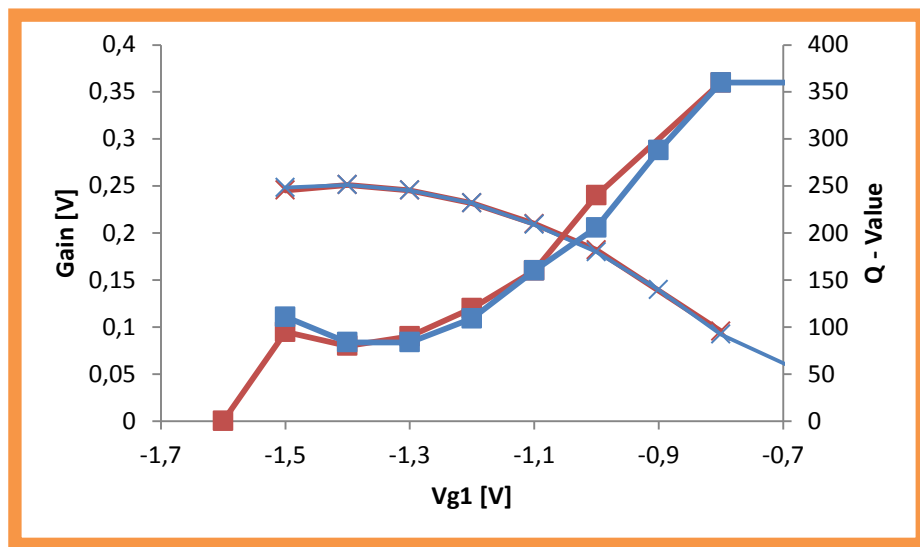
Figure 4.23: Amplifier response at cryogenic temperature with only a single FET in the 1st stage. The drain voltage is 3 Volt. For red lines Vg2 = 0.8 V. For blue lines Vg2 = 0.6 V. Solid square markers are the measured Q – Value and crosses give the voltage gain of the amplifier.

4.4   Plasma diagnostics
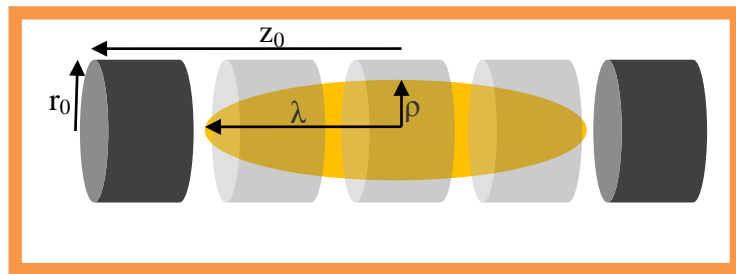
Figure 4.24: Schematic overview of a cylindrical 5 pole electrode structure. The dark electrodes are called the end-caps. The yellow area represents an ion cloud.

51

The dynamics of charged particles inside a Penning trap depends on the electrostatic and magnetic fields of the Penning trap. The Cooler Trap is a cylindrical Penning trap that consists of 21 low voltage electrodes between a pair of high voltage capture electrodes. This allows for several trap geometries. For our purpose we are interested in two specific scenarios: the minimum 5 pole trap and the full length trap. Initially, particles are trapped in a long trap. In this configuration I assume all electrodes except the outer end-caps grounded. The end-cap electrodes have a potential U_{long}. Later the particles are contained within the five-pole trap potentials. In such a trap, the outer, end-cap electrodes are at a potential U_{short} relative to the central electrode. The other two electrodes are the correction electrodes and their potential can be tuned to make the potential inside the trap harmonic.

	Five-Pole Trap	Full-length Trap
Number of electrodes involved	5	23
Trap Length (z_0)	29.5 mm	201.5 mm
Trap Radius (r_0)	17.5 mm	17.5 mm
Plasma Radius (ρ), assumed	5 mm (assumed)	5 mm (assumed)
Plasma Length (λ), assumed	59 mm	2*201.5 mm
Trap Size (d)	16 mm	201.5 mm
Harmonic term (C_2)	0.26	1 (assumed)
Potential (U)	100 V	100 V
Magnetic field strength (B)	6 T	6 T

Table 4.2: Parameters for the short five-pole trap and the full-length trap. The plasma radius is taken to be equal to the smallest trap aperture.

Table 4.2 lists the basic properties for both configurations. A few of the geometrical parameters are shown schematically in figure 4.24. The trap size ($d = \frac{1}{2}\sqrt{z_0^2 + \frac{r_0^2}{2}}$) combines length and radius of the trap [28]. The harmonic term (C_2) is defined in equation 2.6. It makes the trap size comparable to an ideal hyperbolic Penning trap.

Basic plasma properties

To predict the plasma dynamics, a few basic plasma properties need to be determined. They can either be estimated or be calculated *ab initio*. The latter obviously has the advantage of precision. Important, for any calculations, is knowledge of the plasma constituents. Inside the Cooler Trap, the plasma is mixed. The HITRAP decelerator is expected to supply in the order of 10^5 highly charged ions. These ions will be mixed, during electron cooling, with electrons. The maximum number of electrons depends strongly on the trap parameters, but for now we assume that this number will be many orders of magnitude larger than the number of ions. Therefore we can, initially, only look at the dynamics of a pure electron plasma.

The Brillouin limit

To begin we need an estimate for the particle density (n) inside the trap. The maximum particle density trapped by a magnetic field B is called the Brillouin limit [77].

$$n_B = \frac{\epsilon B^2}{2m}$$

4.1

Here ϵ is the dielectric constant *in vacuo* and m is the charged particle mass. In a Penning trap, the magnetic field only provides radial confinement. For axial confinement there is an electric field. To reach the Brillouin density, the electric field must be strong enough to provide the same level of confinement. For the Cooler Trap, with its 6 T magnetic field, this will not be the case.

The electric field limit

For densities well below the Brillouin limit, we can assume a cylindrical shape of the ion cloud as well as a prolate shape. The maximum number of charges that can be contained by an electric field, assuming a cylindrical ion cloud, is given by [78]:

$$N_q = \frac{4\pi\epsilon L U_d}{q}\left(1 + 2ln\frac{r_0}{\rho}\right)^{-1}$$

4.2

Where $U_d = U_0(1 - D_0)$ is an effective potential, depending on the geometry factor D_0. For the Cooler Trap, where $\frac{L}{2r} > 2$, $D_0 = 0$ for both configurations. The 5 pole trap can thus hold 11.7×10^8 electrons within a plasma volume of $4.6\ cm^3$, giving the maximum density: $n_{max} = 2.5 \times 10^8$ cm^{-3}. We assume that the actual density of electrons in the trap will be of the same order of magnitude.

Density and aspect ratio

Figure 4.25 shows that the plasma density will change a lot for plasma radii smaller than the trap's defining aperture. Therefore, a density dependent study of the plasma frequencies will be presented below as well.

Another important parameter is the aspect ratio $\alpha = \frac{\lambda}{\rho}$ of the plasma. Initially, we can use the basic trap parameters listed in table 4.2 to predict the aspect ratio. But in the next chapter we will find a more reliable method of calculating α.
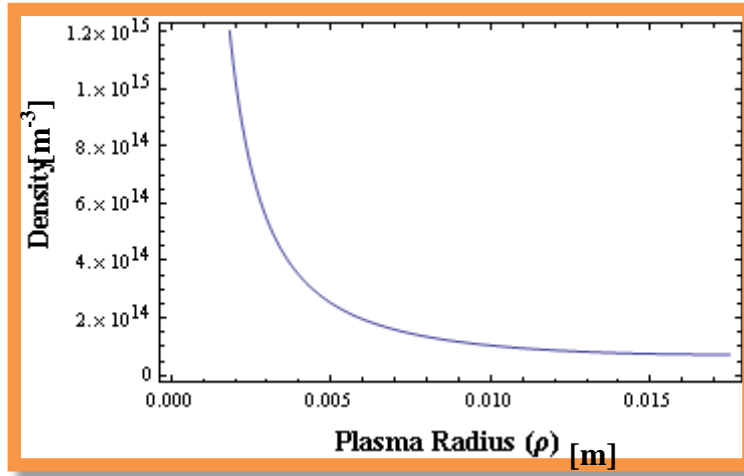
Figure 4.25: Particle density in the five-pole trap as a function of plasma radius. The number of trapped particles is kept constant in this calculation.

Fundamental frequencies

The plasma modes represent collective motion within the one-component plasma. For the plasma modes, two fundamental frequencies are important. These are the axial frequency (ω_z), and the plasma frequency (ω_p). The first is the motion of the entire cloud within the electric potential, the latter is associated with the restoring force of small perturbations within the plasma.

Assuming a harmonic potential, undisturbed by space-charge effects, the axial frequency is given by [28]:

$$\omega_z = \sqrt{\frac{qU_{eff}}{md^2}},$$

4.3

with $U_{eff} = U_0 \times C_2$ the effective potential of the cylindrical trap. As more and more charged particles are added to the trap, the harmonicity of the potential is destroyed. In this case, the frequency is difficult to predict. Depending on the number of particles, the frequency can easily be reduced by 10%.

The plasma frequency for a spheroidal plasma is given by [79]:

$$\omega_p = \sqrt{\frac{nq^2}{\epsilon m}}$$

4.4

54

From now on, we assume a prolate shape of the plasma. For an ellipsoidal plasma, these two frequencies can be used to accurately determine the aspect ratio [79, 80]:

$$\frac{\omega_z^2}{\omega_p^2} = \frac{1}{\alpha^2 - 1} Q_1\left(\frac{\alpha}{\sqrt{\alpha^2 - 1}}\right) \qquad 4.5$$

Here $Q_1(x)$ is a Legendre polynomial.

Mode frequencies

The plasma modes for an ellipsoidal plasma divide in axial modes and radial modes [79, 80]. Because the Cooler Trap is radially symmetric, and because we will detect mainly in the axial direction, only the axial solutions are given. These follow the dispersion relation:

$$1 - \frac{\omega_p^2}{\omega_l^2} = \frac{k_2}{k_1} \frac{P_l(k_1)\dot{Q}_l(k_2)}{\dot{P}_l(k_1)Q_l(k_2)}, \qquad 4.6$$

with $P_l, \dot{P}_l, Q_l, \dot{Q}_l$ again Legendre polynomials and their derivatives and l the mode number. The parameters k_1 and k_2 are given by:

$$k_1 = \frac{\alpha}{\sqrt{\alpha^2 - 1 + \frac{\omega_p^2}{\omega_k^2}}}$$

$$\qquad 4.7$$

$$k_2 = \frac{\alpha}{\sqrt{\alpha^2 - 1}}$$

Also, it is worth to note that the first mode is the axial frequency. Also, above the 2nd mode, the modes split up into multiple frequencies. The solutions to equations 4.5 and 4.6 are listed in Table 4.3.

Frequency	Five-Pole Trap	Full-length Trap
Density	2.5×10^8 cm^{-3}	2.5×10^8 cm^{-3}
Aspect ratio	9.4	39.3
Plasma Frequency	143 MHz	143 MHz
Axial Frequency	21 MHz	6.7 MHz
2nd mode	33 MHz	11 MHz
3rd mode	43 MHz	15 MHz
	6.9 MHz	1.7 MHz
4th mode	52 MHz	18.2 MHz
	12 MHz	3.03 MHz

Table 4.3: Cooler Trap electron frequencies ($\nu = \omega/2\pi$) for a 5 pole trap.
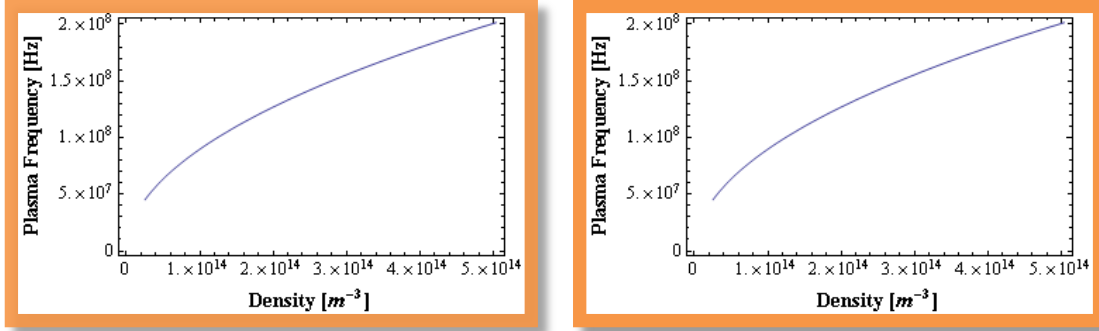
Figure 4.26: Plasma frequency as a function of density for the five-pole trap (left) and the full-length trap (right).
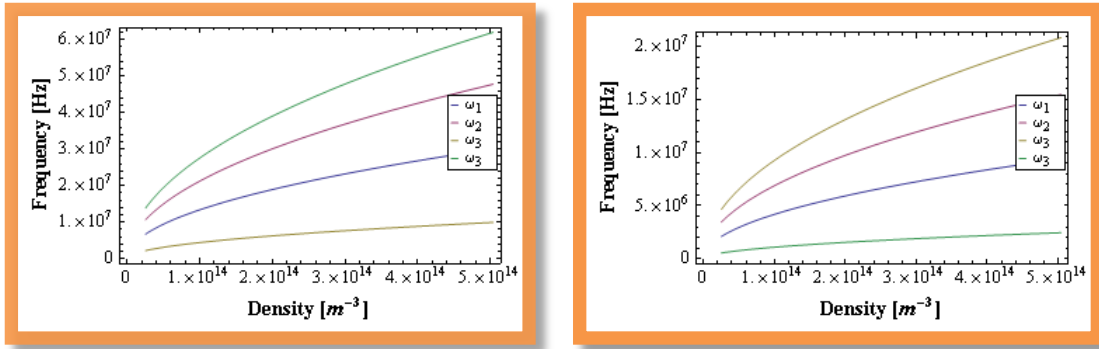
Figure 4.27: Mode frequency as a function of plasma density for the first three plasma modes. The third mode is split into two branches. The left hand side shows the modes for the five-pole trap and on the right it shows the modes for the full-length trap.
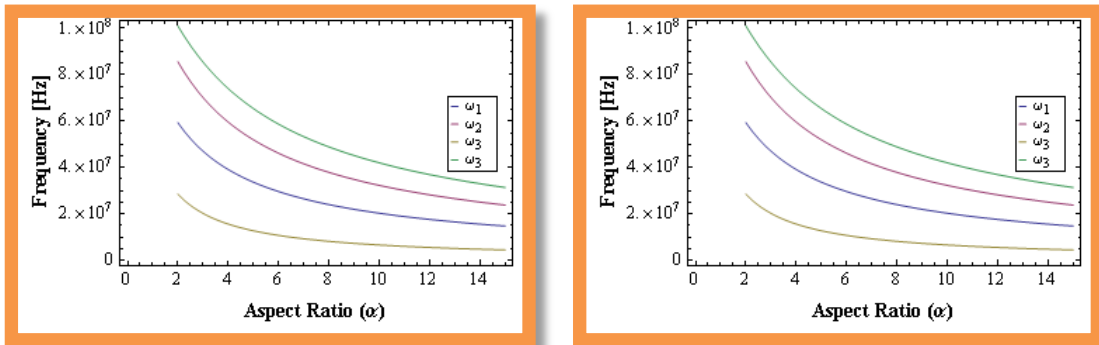
Figure 4.28:Mode frequency as a function of aspect ratio for the first three plasma modes. The third mode is split into two branches. On the left it shows the modes for the five-pole trap and the modes for the full-length trap are shown on the right.

It is important to remember that all the predicted values strongly depend on the exact properties of the plasma. As mentioned above, some of these, such as the plasma radius, cannot be known exactly a priori. For plasma at 0 Kelvin, the defining parameters are the aspect ratio and the density. Figure

56

4.26 shows how the plasma frequency develops as a function of density for both trap configurations. The change of the mode frequencies as a function of density is shown in figure 4.27, while the mode frequency as a function of aspect ratio is shown in figure 4.28.

Temperature shift

For non-zero plasma temperature, the dispersion relation is given by [79, 80]:

$$\varepsilon_3 = \sqrt{\frac{\alpha^2 - \varepsilon_3}{\alpha^2 - 1} \frac{P_l(k_1)\dot{Q}_l(k_2)}{\dot{P}_l(k_1)Q_l(k_2)}} \qquad 4.8$$

For a single-species plasma, ε_3 is:

$$\varepsilon_3 \sim 1 - \left(\frac{\omega_p{}^2}{\omega^2 - {3k^2 k_B T}/{m}}\right), \qquad 4.9$$

with $k = \pi\frac{(l-1)}{2\lambda}$. For $T = 0\ K$, equations 4.8 and 4.9 will give the same results as in the previous section. A non-zero temperature, however, results in a shift of the mode frequencies as depicted in figure 4.29.
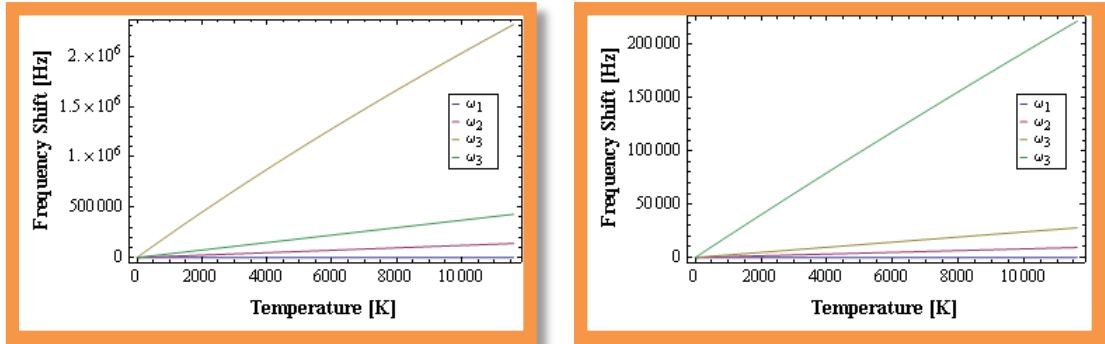
Figure 4.29: Temperature shift of the mode frequencies for the first three plasma modes in the five-pole trap (left) and the full-length trap (right).

Measurement

The oscillating motion of the charged particle plasma induces an image current in the electrodes of the Penning trap. For an axial frequency of 10 MHz and 10^8 electrons at an approximate electrode distance of 30 mm, the image current induced will be approximately 0.1 mA. This signal will carry all the way through the DC-supply lines of the Cooler Trap electrodes to the outside world where they may be measured. Because the Cooler Trap will be floating at several kV, all measurement hardware

must be placed inside a dedicated high voltage cage. Therefore, all hardware was designed with remote read-out in mind.

Hardware

To separate the AC ion signal from the DC power line, a capacitive coupler has been designed. This, so-called in-coupler is similar to a basic RC high-pass filter. The signal is coupled in through a 10 nF capacitor and a 50 Ohm resistor is used to match the impedance of the system. Special care was taken to make sure that the upper cut-off frequency is well above the plasma frequencies. This upper cut-off frequency results from the non-ideal nature of the individual components. This resulted in a stable band pass between 112 kHz and 160 MHz. Between 160 MHz and 500 MHz the signal still gets through the circuit, but at an additional attenuation of roughly 5 dB.

The power supplies to the electrodes provide a voltage of up to 250 V. Therefore, components were chosen to allow for such voltages.

As the plasma cools off, the signal from the plasma modes reduces in amplitude. By applying broadband noise in the frequency region of interest, the plasma modes can be excited and they will become visible.

For plasma diagnostics, a Rohde & Schwarz signal generator and an ADVANTEST frequency analyser are available. With the signal generator a FM modulated signal in the neighbourhood of the predicted frequency mode can be generated and applied to one of the end-cap electrodes of the 5 pole trap configuration. The frequency analyser can be used to measure a signal on the opposite end-cap electrode.

5   Measurement of the *g*-Factor of HCI's

Previous *g*-factor measurements were performed on a single ion, created and stored in a Penning trap [5-7]. The measurement uses the continuous Stern-Gerlach effect to measure the *g*-factor[81]. Here, the magnetic moment of the ion aligns with the magnetic field. Microwave radiation is used to induce spin flips which are subsequently measured through a change in the axial frequency. Finally, the spin flip probability is measured with respect to the microwave frequency, giving the *g*-factor through the following relation:

$$\hbar\omega_{mw} = g_J \mu_B B \qquad\qquad 5.1$$

Here ω_{mw} is the resonant microwave frequency, B is the magnetic field, $\hbar$ and μ_B have the usual physical meaning and finally g_J is the electron *g*-factor.

The Stern-Gerlach experiment is very well suited for systems where the total angular momentum is ½. For systems with non-zero nuclear spin, the experiment becomes more complicated. There are more than two Zeeman sub-levels in the ion's ground-state. This makes it more complicated to identify spin-flips.

The hyperfine splitting of high-Z hydrogen-like ions has been measured in storage-ring and EBIT experiments [55-58]. Also the transition probability was measured. This transition probability depends on the magnetic moment, and thus on the *g*-factor, of the system[8]. Although an experimental *g*-factor for hydrogen-like lead could thus be extracted, its experimental uncertainty is very large due to the principle limitations of lifetime measurements.

5.1   *Laser-microwave double-resonance spectroscopy*

Alternatively, laser-microwave double-resonance spectroscopy can be used to measure the ionic *g*-factor in ions with non-zero nuclear spin [16]. The transitions between the hyperfine levels of heavy highly-charged ions lie in the optical regime. These can therefore be probed by a laser field. In the homogeneous magnetic field of the Penning trap, the hyperfine levels of the ion split up in their Zeeman sub-levels. The transition frequency between the sub-levels is in the order of a few tens of GHz, thus in the microwave regime.
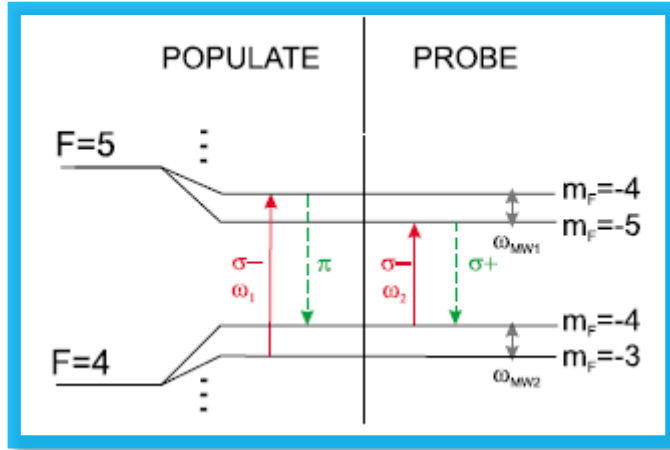
Figure 5.1: Scheme of the Zeeman-split hyperfine energy levels in the ground-state of a H-like ion with I=9⁄2 and the measurement principle for the double-resonance technique. Solid arrows indicate excitation laser and microwave photons [16].

Figure 5.1 depicts the concept of the double-resonance technique. Briefly, the measurement is performed in 2 steps. First, polarised lasers populate one of the extremal sub-levels, this is called optical pumping. After that, circularly polarised light is used to drive the transition between two extremal sub-levels of different hyperfine state. The fluorescent light from this drive is observed and thus probes the population of the extremal state. When an on-resonance microwave field is applied, the population of ions in the extremal state decreases. This results directly in an observable decrease in the intensity of fluorescent light.

Depending on the nuclear spin and the sign of the nuclear magnetic moment, the level scheme of the ion can look different from the one shown above. A negative nuclear moment, for instance, inverts the scheme. Another possibility is that the nuclear spin *I=1/2*. In this case, the ground-state is *F=0* and does not split into separate Zeeman sub-levels. In this last case, optical pumping is clearly not possible. However, with circularly polarised light, the transitions between the Zeeman sub-levels in the excited state can still be probed by exploring the polarisation of the emitted fluorescence photons. Thus, the double-resonance technique can still deliver a measurement of the ionic *g*-factor [16].

Figure 5.1 also shows that two different Zeeman transitions can be probed, ω_{mw2} in the ground state and ω_{mw1} in the first excited state of the ion. Both give a different g_F as the main quantum number *F* is different. The underlying electronic and nuclear *g*-factors are still the same. Thus, when both transitions are measured, g_I and g_J can be obtained individually [16].

This experimental method would be performed on a cloud of ions, rather than on a single ion. Therefore, enough statistical data can be acquired easily. In a laser-microwave double-resonance experiment, the accuracy and resolution of the microwave scan govern the accuracy to the *g*-factor measurement. An accuracy in the order of 10^{-9} for determining the microwave transition frequency has been predicted [16]. The magnetic field can be accurately determined by measuring the motional frequencies of a single ion and using the invariance theorem in equation 2.14. The measurement of the magnetic field on a single ion must be alternated with the spectroscopy measurement.

5.2   Injection into the magnetic field and Penning trap

Ions leaving the Cooler Trap pass through the vertical beam line and the experimental beam line at a transport energy of 5 keV/q to the *g*-factor trap. The estimated length of the ion bunch is 250 mm. These ions must be guided into the magnetic field and be decelerated down to the trapping velocity of 100 eV/q before they can be confined in the *g*-factor Penning trap.
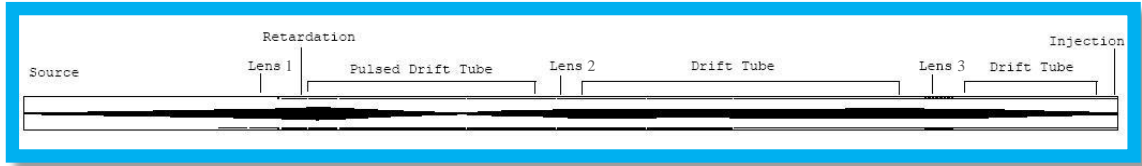
Figure 5.2: Simion simulation of the einzel lens structure of the g-factor injection line. The source corresponds to the focal point of the electrostatic bender. A series of lenses and a pulsed drift tube will inject the beam into the injection point of the magnetic field[82].

Design

A kicker-bender combination, built at KVI Groningen, will divert ions from the experimental beam line into the *g*-factor injection line. The highly charged ions will be injected electrostatically into the magnetic field of the *g*-factor Penning trap, employing a scheme similar to that of the ISOLTRAP experiment at CERN [74]. Figure 5.2 shows the schematic overview of the injection line as well as the simulated beam envelope [82]. Starting at the focal point of the electrostatic bender, the ions are shot through a pulsed drift tube (PDT), several einzel lenses, retardation electrodes and normal drift tubes. The entire line will electrically shield the ions from the outside world. This way the background potential can be easily controlled. This also means that the electrostatic line is effectively a tube within a tube, with the outer tube being the vacuum system of the beam line. Especially at close proximity to the trap, the available space is limited and therefore the inner diameter of the injection optics cannot be larger than 50 mm.

61

The retardation electrode at 2.3 kV and a pulsed drift tube (PDT) at 4 kV slow down the ions to about 1 keV/q[82]. The retardation electrode is necessary to smooth the potential transition into the PDT. When inside the pulsed drift tube, the potential will be ramped down to -0.9 kV. The remaining part of the injection line, up to the Penning trap, maintains this as its ground potential. H-like uranium ions with kinetic energy of 1 keV/q move with a velocity of 40 km/s. With a bunch length of 250 mm and a PDT of 440 mm length, the time between the tail of the bunch entering and the front of the bunch reaching the start of the fringe field (see below) is 3.5 µs. The voltage on the PDT must be switched within that time frame. Fast HV-switches (e.g. Behlke switches) exist that provide a rise time below 60 ns for voltage differences of 16 kV [83].

	P [mm]	L [mm]	Comments
Kicker-bender	0	395	Starting point of the injection line
Entrance tube	395	60	Grounded and part of lens 1
Einzel lens 1	455	60	Focal element
Retardation electrode	516	60	Smoothens the decelerating potential of PDT
Pulsed Drift Tube	577	445	Switched between 4 kV and -0.7 kV
Fixed tube	1022	60	Part of lens 2
Einzel lens 2	1082	60	Focal element
Fixed tube	1143	60	Part of lens 2
Segmented tubes	1204	4 x 60	Mostly as drift tubes
Drift tube	1442	390	Also part of lens 3
Einzel lens 3	1830	60	Focal element
Drift tube	1890	330	Also part of lens 3
Injection point	2225	0	Focal point for injection

Table 5.1: List of components and sizes that make up the electrostatic injection line into the g-factor trap. The beam line will be an electrically closed system, starting at the entrance electrode. The injection point is where the beam should be focussed for an optimum injection. P denotes the start position of the element and L its length. All elements, starting with the entrance electrode, have an inner diameter of 50 mm.

Three einzel lenses provide focussing. After injection into the B-field, the ions will be strongly confined radially as they travel towards the trap. They will lose most of their remaining velocity against the ground potential of the trap. The ions will finally enter the trap with an energy of 100 eV/q and they can be trapped easily. Table 5.1 provides an overview of the different components of the injection line. Einzel lenses always consist of three rings, with a voltage between the central ring and the outer rings. In the table the central ring is labelled as the focal element. The tubes before and after assume the role of outer ring.

The static behaviour of the injection beam line was studied using SIMION. The purpose of this study is to determine if ions can be focussed sufficiently at the injection spot. Injection studies at ISOLTRAP show that, once the ions are injected into the magnetic field, they will maintain their focus [74]. The 1st high voltage electrode of the capture trap forms the limiting aperture for injection. This electrode

has an inner radius of 2.5 mm. This then is the maximum spot size at the injection point. In general, a smaller spot size leads to a smaller magnetron radius when inside the trap.

The voltages will be given in this study as the ions feel them. So, for a part of the beam line floating at e.g. 4 kV, a voltage of -1 kV means 3 kV with respect to the absolute ground. The simulations were performed using a H-like uranium beam with an initial energy of 5 keV/q. The ions were generated on axis at the position of the focal point in the kicker-bender. As initial distribution a circular spot with a radius of 1 mm was chosen. The divergence of the beam was 1 degree.
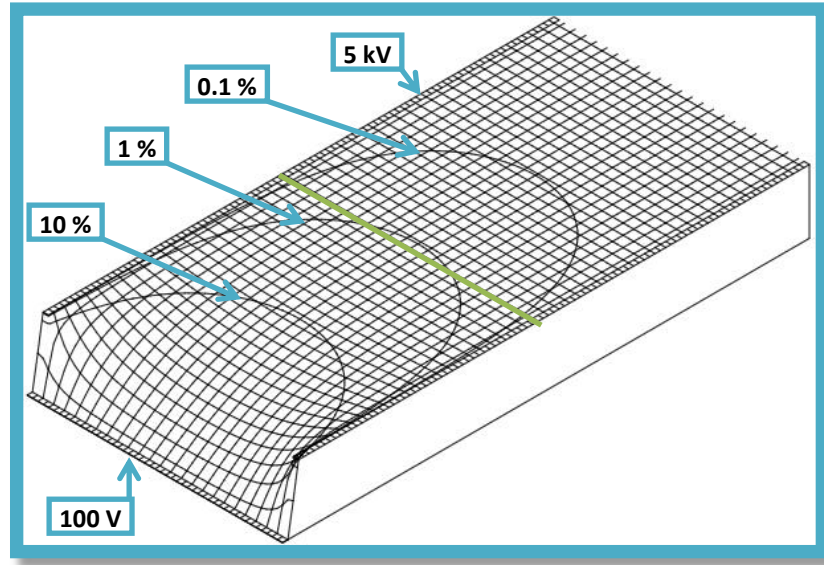
Figure 5.3: Fringe field inside a cylindrical tube for a potential difference of 4.9 kV. The equipotential lines of the fringe field are indicated relative to the tube potential of 5 kV. At the green line the distance from the entrance to the tube is equal to its diameter.

Fringe fields

In this study the pulsing of the PDT was not simulated. Instead, the line after the PDT was maintained at the same 4 kV potential of the PDT in order to simulate the smooth transition potential for the ions leaving the PDT. As the PDT would be pulsed with the ions inside, the ions would not feel the changing of the potential and the result would be the same as long as fringe fields the ions feel are small enough. The size of the fringe field is shown in figure 5.3. At a distance l into the tube, where $l/d \geq 1$ and d is the diameter of the tube, the influence of the fringe field on the potential in the tube is only 1% or smaller. Since the diameter of the PDT is 50 mm and the length of the ion bunch is 250 mm a PDT of 440 mm sufficiently shields the ions from the change in potential during switching.

Retardation
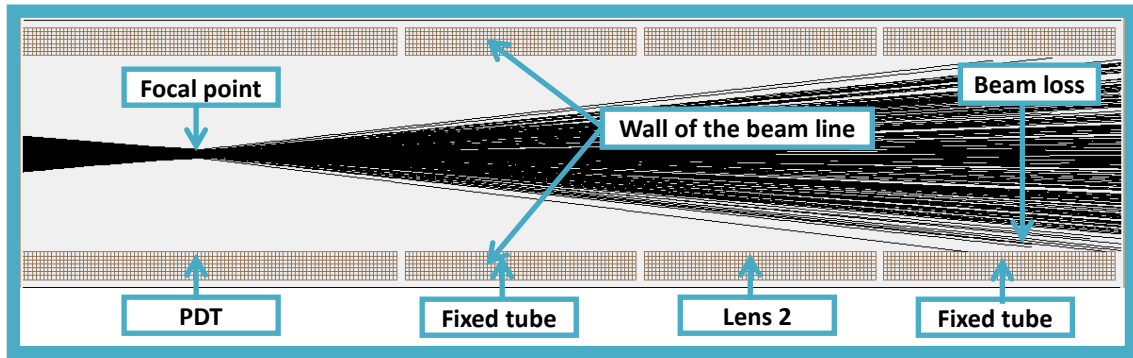
Figure 5.4: Beam focus and consecutive loss against the wall of the beam line. Ion-optical elements are as labelled.
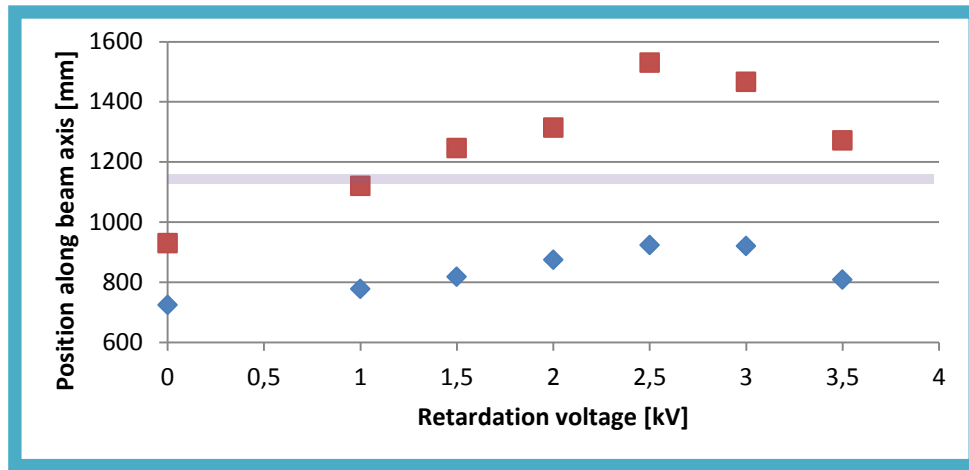
Figure 5.5: Effect of the retardation electrode on the ion beam without any additional focussing. The purple line gives the approximate position of the 2nd einzel lens. Blue dots give the position of the first focal point. Red dots give the position where the beam is lost.

The decelerating potential on the PDT also strongly focusses the beam. After the focal point, the beam spreads out again and is lost against the wall of the beam line. An example of this is shown in figure 5.4. Figure 5.5 and figure 5.6 show the effect the retardation electrode has on the beam when particles decelerate against the PDT voltage. The most important point is to prevent the beam from colliding with the beam-line wall before the 2nd lens has the opportunity to refocus the beam. Figure 5.5 shows that a retardation potential is necessary to prevent the beam from being lost inside the PDT. Without a retardation potential the particles directly decelerate against the PDT and are subsequently lost inside the PDT itself.
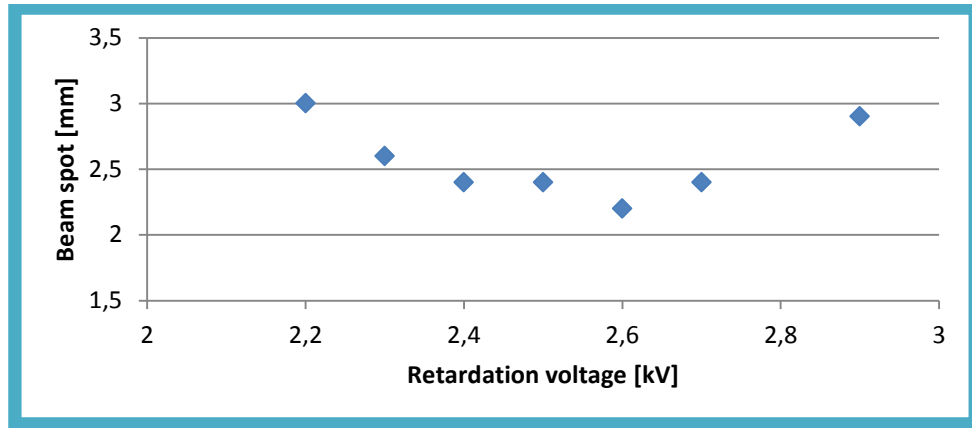
Figure 5.6: Effect of the retardation electrode on the spot size at the injection point. Lens 1 has a voltage of -100 V, lens 2 is on a -2.3 kV potential and lens 3 is on a voltage of -1.45 kV.

Ion optics
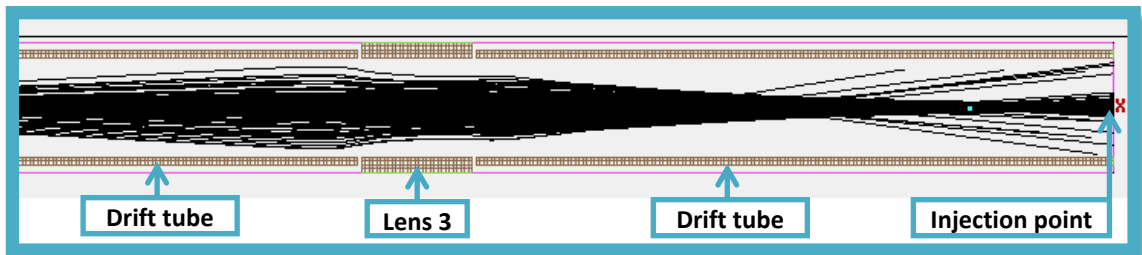
Figure 5.7: Simulated ion trajectories through lens 3 and onto the injection point. All elements are as labelled. Some stray particle trajectories hit the wall before arriving at the injection point.
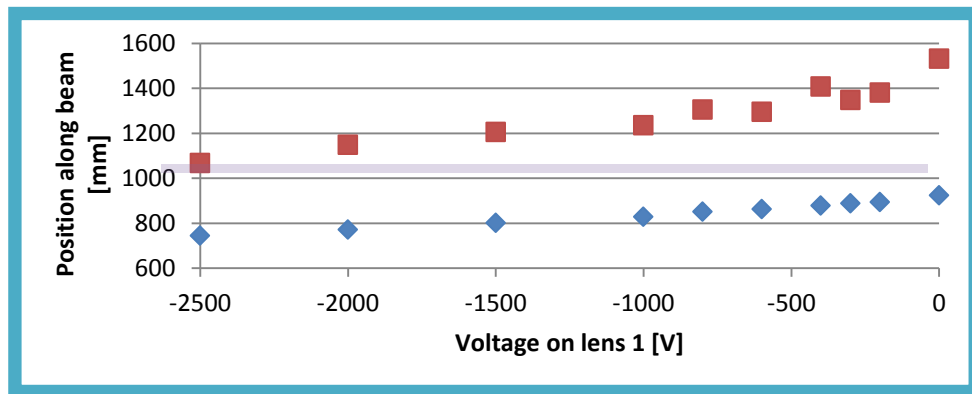
Figure 5.8: Characterisation of lens 1 together with a retardation voltage of 2.5 kV. All other lenses are grounded. The red dots give the location where the beam is lost while the blue dots give the position of the focal point. The purple line marks the location of lens 2.

Figure 5.7 shows how lens 3 focusses the ion trajectories at the injection spot. However, when ions are simulated close to the wall of the beam line, their trajectories are influenced by the discrete nature of the geometry. This results in trajectories that deviate significantly from the beam envelope. In the simulations below, great care has been taken to avoid these stray trajectories.

Lens 1

The first lens is situated before the retardation electrode. Figure 5.8 shows how the focal point and beam loss depend on the voltage at lens 1. In figure 5.9 the simulated beam spot is shown for different settings of lenses 2 and 3. In this figure, settings for which the beam was lost are given a beam spot of 30 mm. This value is chosen well above the radius of the beam line to avoid confusion.
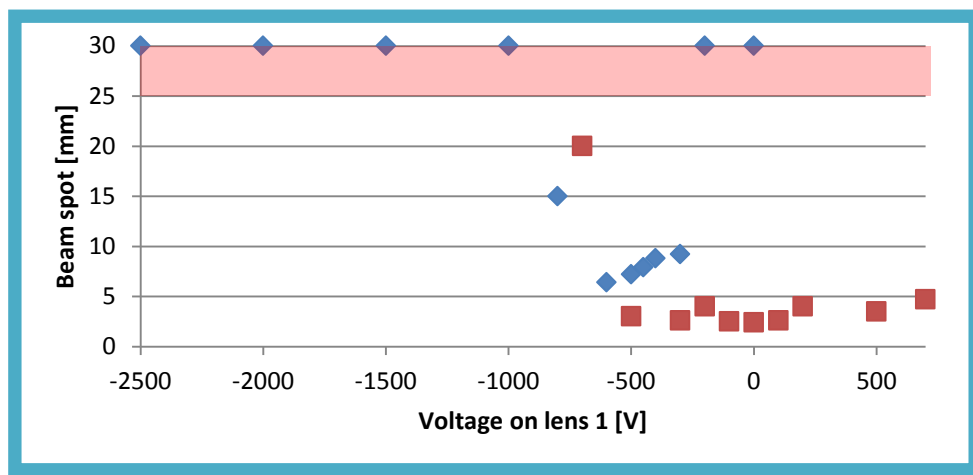
Figure 5.9: Beam spot at the injection point for different voltages on lens 1. For the blue curve, the retardation voltage is 2.5 kV, lens 2 is at -1.5 kV and lens 3 is grounded. For the red curve, the retardation voltage is 2.5 kV as well, lens 2 is at -2.3 kV and lens 3 is at -1.45 kV. The red zone marks the wall of the beam line. Points larger than the electrode radius ($r_{max} = 25\ mm$) are configurations for which the beam was lost before the injection point.

Lens 2

Lens 2 is the first lens after the pulsed drift tube. It refocuses the beam leaving the PDT and prepares the beam for lens 3. This is shown in figure 5.10. Figure 5.11 shows several graphs of the spot size at the injection point for different settings of lenses 1 and 3. As before the settings for which the beam hits the wall are given a value of 30 mm and are clearly marked outside the width of the beam line.
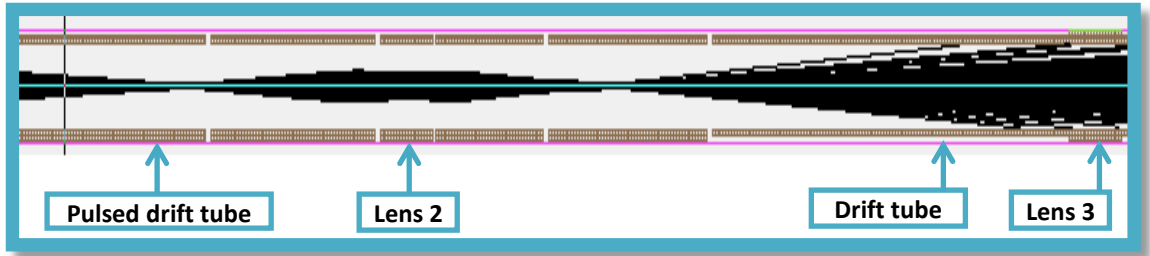
Figure 5.10: A part of the beam line surrounding lens 2. The divergent ion beam leaving the PDT is refocused by the lens 2 voltage.
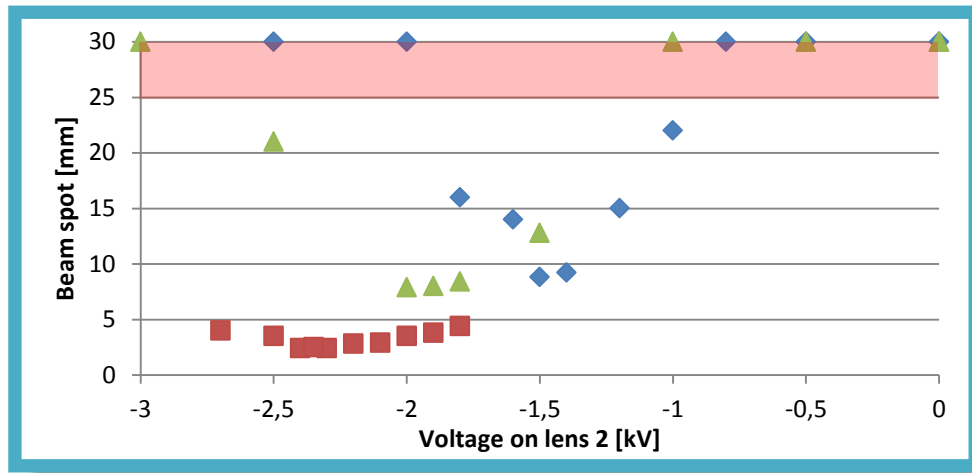
Figure 5.11: Beam spot at the injection point for different voltages on lens 2. The green curve represents simulations where the retardation voltage is 2.5 kV and both the other lenses are grounded. For the blue curve, the retardation voltage is 2.5 kV, lens 1 is at -400 V and lens 3 is grounded. For the red curve, the retardation voltage is 2.5 kV as well, lens 1 is grounded and lens 3 is at -1.45 kV. The red zone marks the wall of the beam line. Points larger than the electrode radius ($r_{max} = 25\ mm$) are configurations for which the beam was lost before the injection point.

Lens 3

Figure 5.12: The simulated beam envelope between the ion source and the injection point. In this simulation the retardation voltage was 2.6 kV. Lens 1 was at -100 V, lens 2 at -2.3 kV and lens 3 at -1.45 kV. The injection spot has a radius of 2.2 mm. The width of the picture has been enlarged compared to its length for visual reasons.

Lens 3 is the last optical element before the ions are injected into the magnetic field. With this lens, the ion beam must be focused onto a 2.5 mm spot at the injection point. Simulation results for the

behaviour of lens 3 with different settings of lens 1 and lens 2 are shown in figure 5.14. Figure 5.12 shows the complete beam envelope for the best solution achieved in this simulation. For a retardation voltage of 2.6 kV, lens 1 at -100 V, lens 2 at -2.3 kV and lens 3 at -1.45 kV the radius of the beam spot is 2.2 mm. Figure 5.13 shows the last section of this simulation, starting just before lens 3. In this figure, the final focal point of the beam coincides with the point of injection.
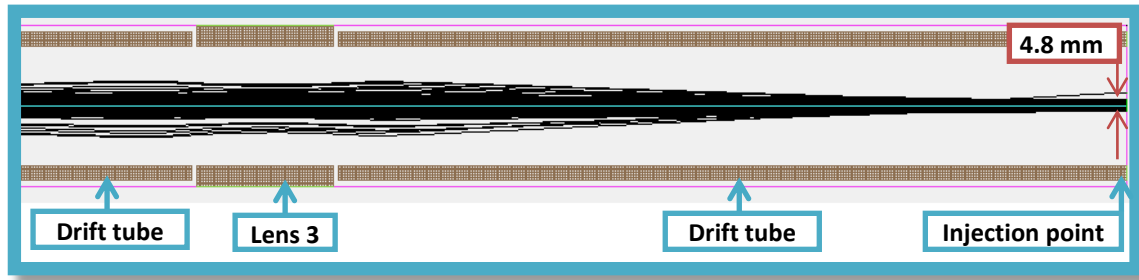
Figure 5.13:The simulated ion beam for lens 3 and the injection point. The settings and final result are the same as for figure 5.12. The different ion-optical elements are labelled and the diameter of the beam spot is indicated.
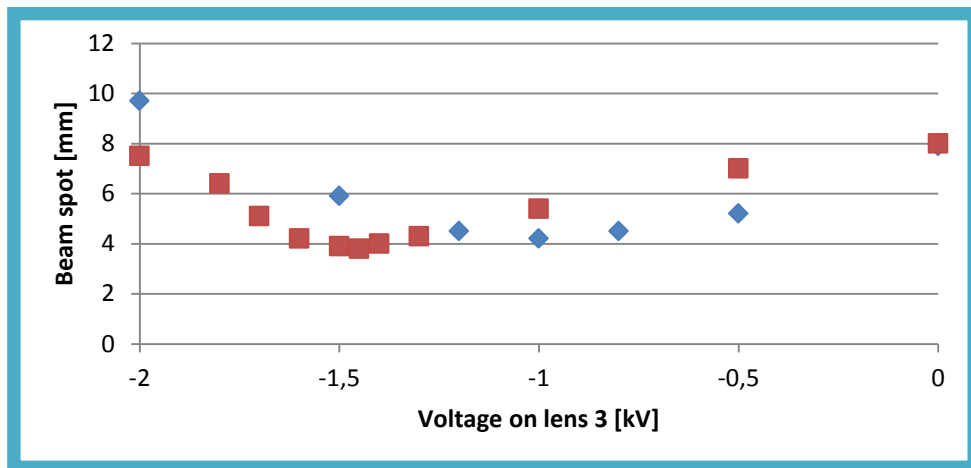
Figure 5.14: Beam spot at the injection point for different voltages on lens 3. For the blue curve, the retardation voltage is 2.5 kV, lens 1 is at -450 V and lens 2 is at -1.5 kV. For the red curve, the retardation voltage is 2.5 kV as well, lens 1 is grounded and lens 2 is at -1.9 kV.

Steering

To correct for misalignments, steering in the transverse direction to the beam is necessary as well. To achieve this, some of the ring elements should be segmented in the X and Y direction. Preferably the rings that are on a ground potential or on a floating ground will be used for steering. Simulation of the steering effects will be necessary as well.

Diagnostics

To shield the beam electrically from the outside, the entire injection line is physically closed as well. In particular large objects such as detectors for intermediate diagnostics cannot be moved into the beam line easily. To solve this, one of the diagnostic boxes that are used elsewhere in the HITRAP beam line may be modified to hold a single tube section from the injection line. In this case, the stepper motor may move this tube out of the beam line to replace it with either a Faraday cup or an MCP. To prevent fringe fields from disturbing the flow of ions, this detector should be made to match the section it replaced. Preferably the same floating ground should be applied.

5.3   The g-factor trap

The superconducting magnet

Using equation 5.1, the *g*-factor of the ion can be inferred from the energy difference between Zeeman sub-levels. This requires an extremely stable and homogeneous magnetic field. To this end, a special superconducting magnet was installed (Figure 5.15).
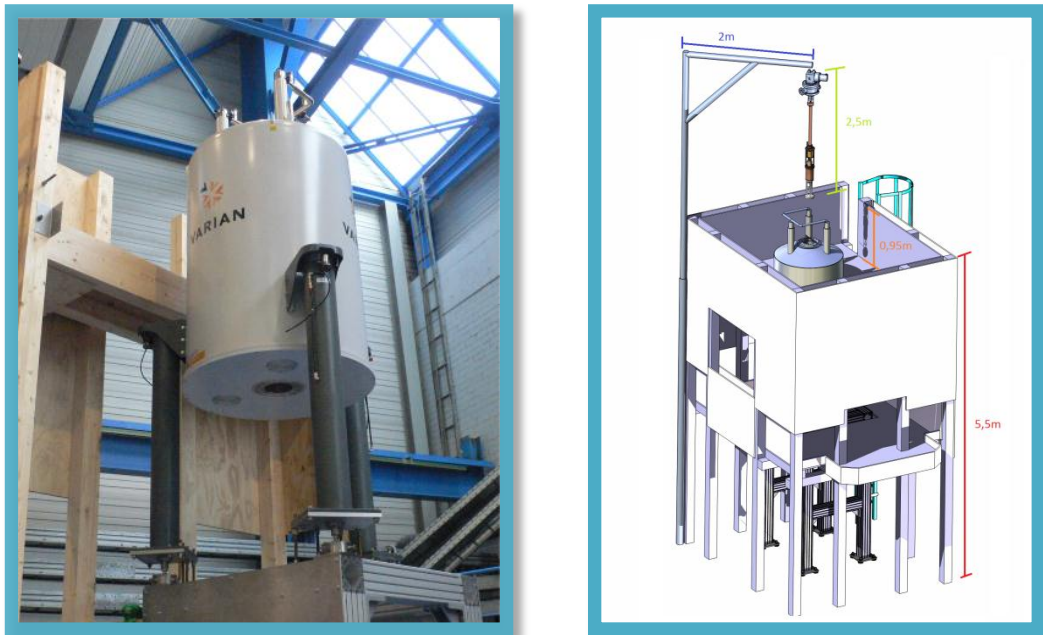
Figure 5.15: The g-factor superconducting magnet and its support structure. Left, a photograph of the magnet barrel and parts of the experimental platform are shown. On the right is an impression of the final structure. A crane will lift the Penning trap and cryocooler into the magnet bore.

The highly homogeneous superconducting magnet provides a field strength of 7.0 Tesla [84]. The magnet is housed in a low-loss cryostat with a vertical room temperature bore with a clear bore size of 160mm diameter. A schematic overview is shown in figure 5.17.
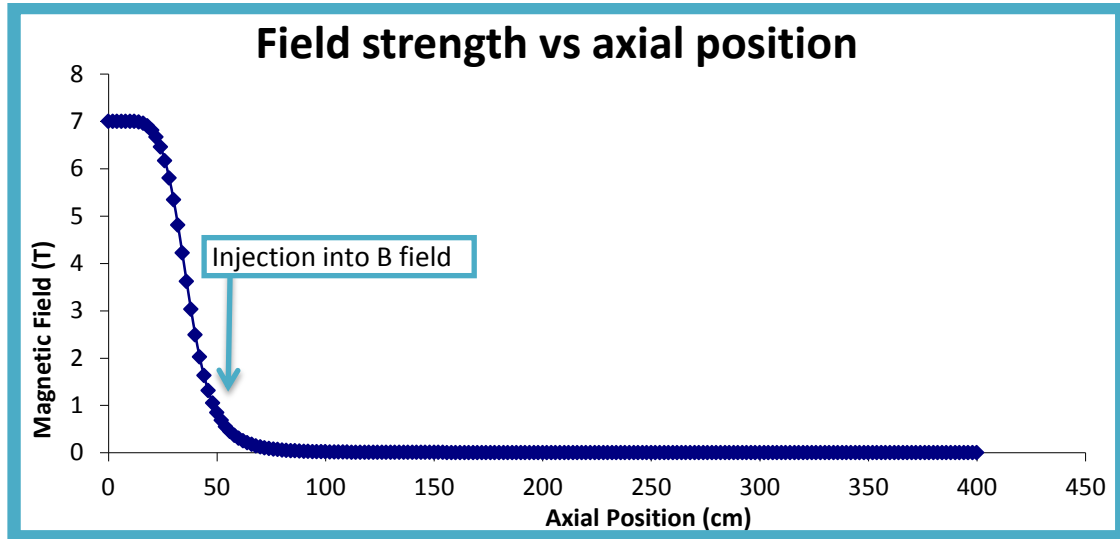
Figure 5.16: Field plot of the g-factor magnet along the vertical axis. The injection point for ions into the magnetic field is labelled.
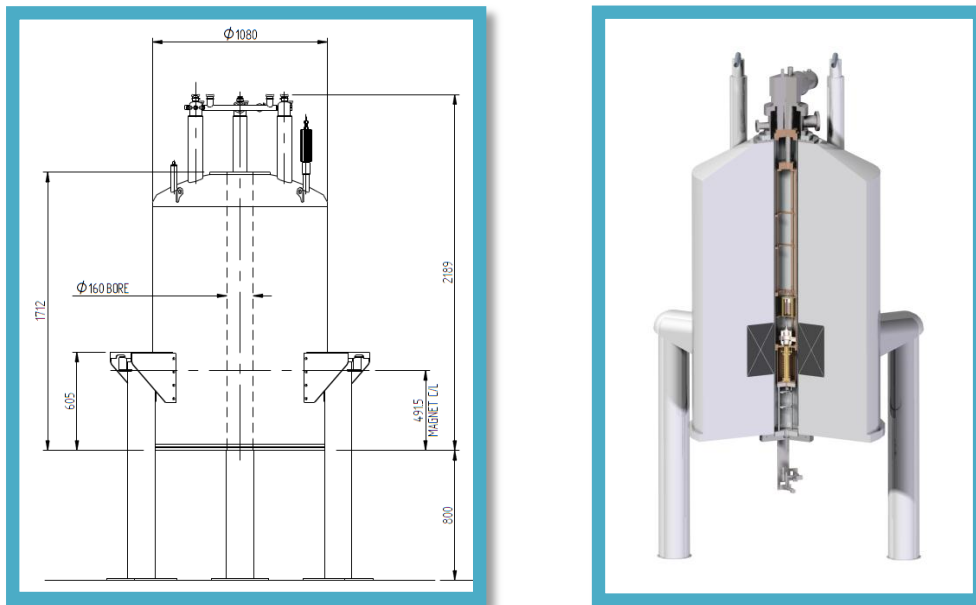
Figure 5.17: Schematic overview of the g-factor magnet barrel. The left hand side shows the outside dimensions. The right hand picture gives a cut-through view of the magnet with the experiment installed inside the magnet bore.

The stability of the magnetic field is better than 1 ppm/hour. The field homogeneity is better than 0.1 ppm over a 1 cm^3 cubic volume. Furthermore, around this is a larger cylindrical volume with 0.5 cm

diameter and 10 cm length over which the field homogeneity is smaller than 10 ppm. The main field strength along the vertical axis is plotted in figure 5.16.

Cryocooler

The *g*-factor measurement will take place at a cryogenic temperature. With the trap at 4 Kelvin, residual gas in the trap area will freeze to the wall, greatly improving the vacuum and thus storage time. Also, the cryogenic temperature is necessary for the resonator coils of the detection electronics (discussed in section 5.4) to become superconducting.

A SRP-082B cryocooler cools the experiment down to this cryogenic temperature. The cryocooler delivers 1 Watt cooling capacity at 4.2 Kelvin. Vibrations, produced by the cooling process, are only 9 micron. This should have a minimal impact on the experimental accuracy.

Electrode structure
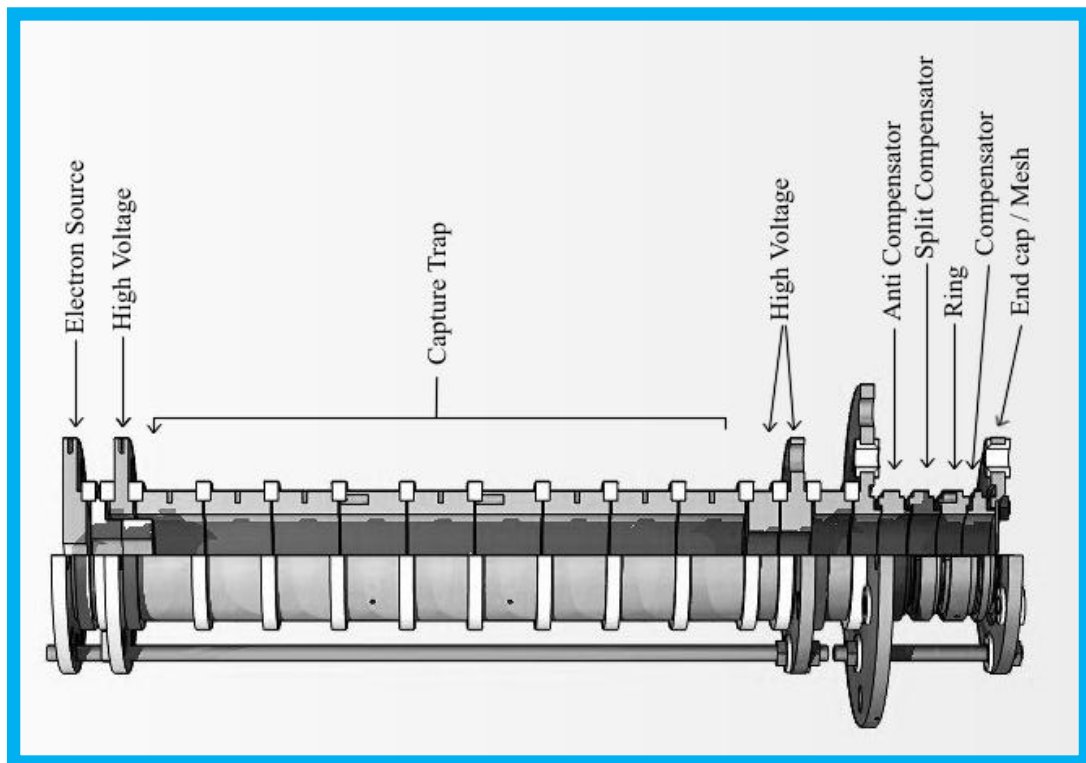
Figure 5.18:Full electrode stack of the g-factor set-up. All separate components are as labelled.

Figure 5.18 shows the complete stack of electrodes that make up the *g*-factor trap. The electrode stack consists of two parts. The first part, the capture trap, was designed to capture, cool and prepare

ions for the actual experiment. In the second part, the spectroscopy trap, the actual measurement takes place. Naturally, the demands on both sections are very different. Separating the two traps is a set of high voltage electrodes. During capture they provide the blocking potential, but afterwards they will act as transport electrodes. This restricts their maximum length, hence they are axially split.

Housing and assembly

The electrode stack is suspended from the base plate shown in figure 5.19. The base plate contains 20 low-voltage feedthroughs and 5 high-voltage feedthroughs. A viewport allows optical access. Instead out of normal glass, the viewport is made out of UV-transparent quartz. It also acts as the top flange to the ultra-high vacuum (UHV) chamber that houses the electrode stack. The cryogenic electronics and detectors are mounted on top of the base flange.
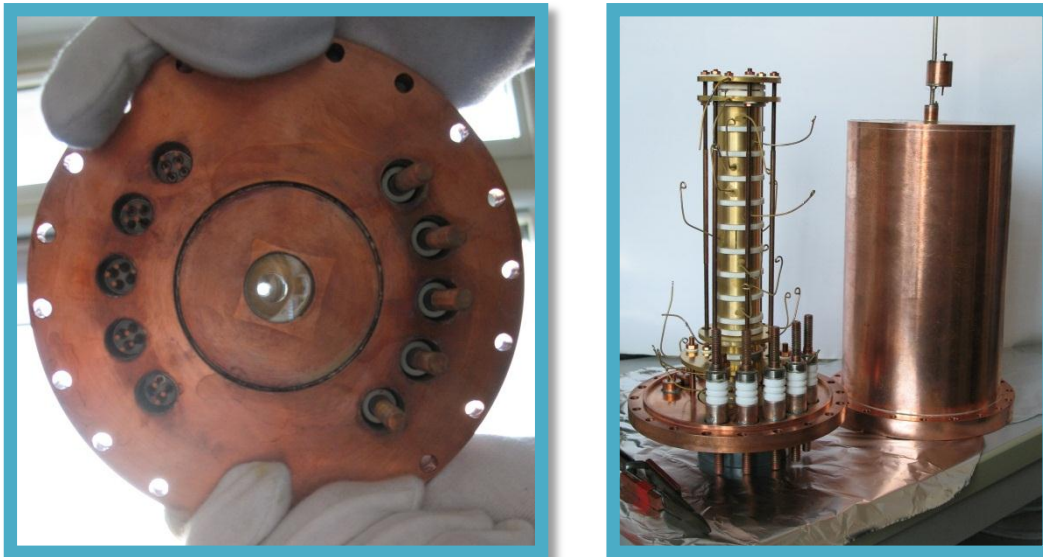
Figure 5.19: Trap assembly. Left is the top view of the base flange with view port in the centre and the feedthroughs around. The picture on the right shows the complete trap assembly with the UHV chamber housing next to it.

The electron source

Similar to the Cooler Trap, electron cooling can be used in the first phase of ion cooling. Also, electron impact ionisation can be used to create ions in the trap itself. These electrons are produced by a field-emission point at the entrance side of the electrode stack [85, 86]. The design is shown in figure 5.20. Electrons, emitted by a tungsten tip, will be accelerated into the capture trap. There they ionise medium-heavy ions such as argon. It is expected that ions at least up to Ar^{13+} can this way be produced inside the trap.
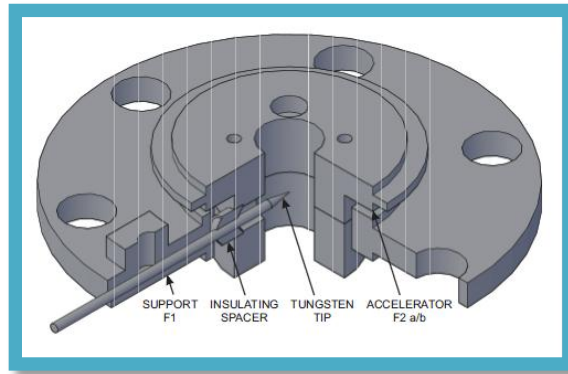
Figure 5.20: Field-emission point. A tungsten tip at a large potential difference to the surrounding electrode emits electrons. The accelerator electrode can give them enough energy to create ions inside the trap.

The capture trap

This first part of the electrode stack combines several functions. First of all, its outer electrodes can create a high-voltage trapping potential of up to 1kV. These potentials switch quickly to capture ion bunches coming from the HITRAP facility. In order to maximize the number of ions inside the trap, the trap length should be as large as possible.

The next task of this section is to cool the ions from their transport energy down to 4 Kelvin. This will be done first by electron cooling and secondly through resistive cooling. Thus, the Penning trap needs to hold both positively charged ions and the negatively charged electrons.

Finally, the electrode structure should allow for manipulations of the ion cloud. These manipulations include cleaning and splitting of the ion cloud and transportation of either a single ion or a whole ion cloud to the precision trap.

To this end, an electrode stack has been designed and built that consists of two high-voltage electrodes and nine low-voltage electrodes. The high-voltage electrode between the Capture Trap and the Spectroscopy Trap is split into two ring electrodes to allow smooth transport between the two traps[82]. The 9 low-voltage electrodes have a length that is 1.203 times their diameter[28]. These dimensions create a mechanically compensated trap with harmonic potential. With alternating potentials, the Capture Trap actually consists of nine individual harmonic traps of opposite potential with virtual end caps in between.

Additionally, the fourth and sixth low-voltage electrodes are radially split. They can be used to measure and manipulate the radial component of the ion motion. All capture electrodes are listed in

Table 5.2. The trap dimensions are given in their room temperature value without gold plating. Gold plating with a silver diffusion barrier added an estimated 0.015 mm layer to the electrodes. The electrodes are separated by ceramic rings. These insulating rings keep the low-voltage electrodes separated by 0.4 mm. The high-voltage electrodes are separated by 0.7 mm to prevent discharge.

Electrode number	Dimensions	Description
H-19	ID: 5.046; IH: 4.986	High voltage entrance electrode
C-13, C-15	ID: 17.513; IH: 14.13	Split low voltage electrode
C-10, 11, 12, 14, 16, 17, 18	ID: 17.513; IH: 14.13	Low voltage capture electrode
H-8, H-9	ID: 10; IH: 6.5	High voltage/transport electrode

Table 5.2: Capture-trap electrode descriptions and inner dimensions in mm (Inner Diameter, Inner Height). Technical drawings are provided in the Appendix A.

The spectroscopy trap
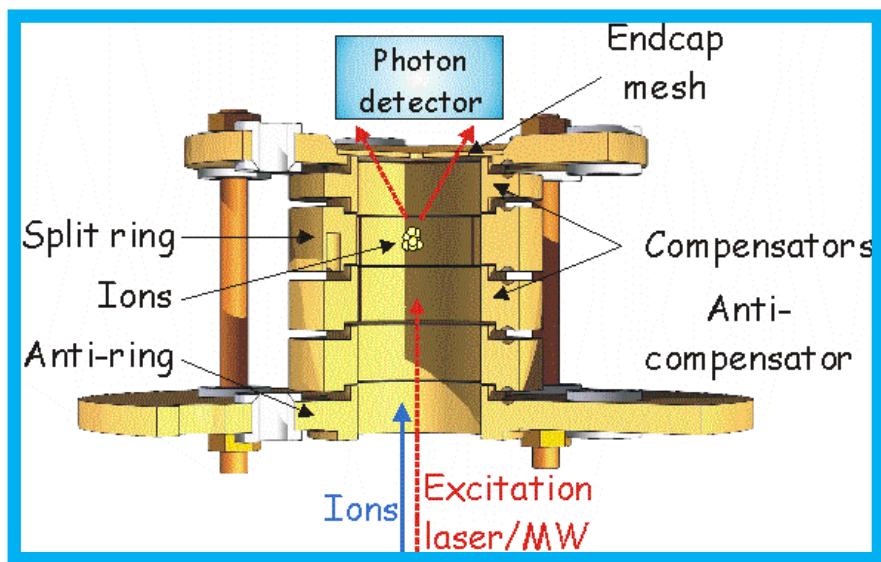
Figure 5.21: Spectroscopy section of the g-factor Penning trap. The ring is a 4-fold split electrode. The lower compensator is 2-fold split. The end-cap consists of a mesh that will let through fluorescent light but at the same time defines the potential.

Figure 5.21 shows the electrode structure of the spectroscopy trap. Ions will enter the trap from below where there is the capture section. Laser access is possible either from below or from the top through a transparent mesh while the fluorescent light can be collected close to the trap behind the end-cap mesh. Close proximity of the detector provides a large solid angle and optimises the fluorescence signal.

The electrode structure is based on the 5 point orthogonal trap with closed end caps[28]. On one side of the trap, the end cap is formed by a copper mesh. This shields the electric potential and is optically

74

transparent at the same time. In order to allow injection of ions, the opposite end cap needs to be open. A near perfect harmonic potential is achieved by adding electrodes to replace the end cap[82]. They mimic a mirror trap on opposite potential. When the potentials of the mirror trap are carefully chosen, both the potential and the potential gradient between the real and the mirror trap will be the same as on the mesh end-cap. This creates a virtual end cap and artificially symmetrises the trap. Figure 5.22 shows the trap configuration and potentials. The trap depth is normalised to 10 V. Figure 5.23 displays the deviation from harmonicity along the longitudinal axis. This figure shows a large area of 6 mm over which there is a near perfect harmonic potential.

Electrode	Voltage	ID	IH	D	Description
T-7	4.025 V	17.513	8		Transport electrode
S-6	10.207 V	17.513	5.729		Anti-ring electrode
S-5	7.994 V	17.513	6.220		Anti-correction electrode
S-4	-7.994 V	17.513	5.893		Correction electrode, split
S-3	-10 V	17.513	5.380	31	Central ring electrode, four fold split
S-2	-7.994 V	17.513	5.893	32	Correction electrode
S-1	0 V			29	End cap with optically transparent mesh

Table 5.3: Spectroscopy-trap electrode descriptions and inner dimensions in mm (Inner Diameter, Inner Height). For appropriate electrodes the effective distance, D, (in mm) is given. Technical drawings are provided in the Appendix B. The end cap is a flat surface and therefore has no dimensions listed. Voltages scale linear while maintaining a harmonic potential.
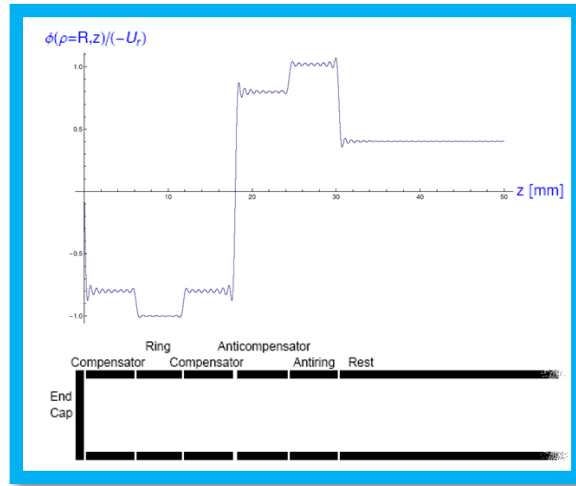
Figure 5.22: Design electrode potentials for the spectroscopy trap. This configuration will create a harmonic potential.

Even with careful construction and tuning, this geometry will lead to small asymmetries[85]. The mechanical uncertainty from machining and handling is 10 micron. This leads to the expansion coefficients C_k that are given in Table 5.4. The odd coefficients largely originate from the asymmetric

structure of the electrode stack. Assuming a trapping potential of 10 V and a single $^{209}Bi^{82+}$ ion with an axial energy of 60 Kelvin, equation 2.9 gives a shift in axial frequency of $\Delta\omega_z/\omega_z \sim 6 \cdot 10^{-11}$.

The ring electrode has been split into 4 equal sections. With this a rotating wall potential can be applied to manipulate the physical size of the cloud. One of the correction electrodes has been split as well. This way the radial motion can be detected and manipulated. The electrodes that make up the spectroscopy trap are listed in table 5.3. The trap dimensions are given in their room temperature value without gold plating. Gold plating added an estimated 0.015 mm layer to the electrodes.

C_1	C_2	C_3	C_4	C_5	C_6
1.6×10^{-5}	0.522644	1.8×10^{-5}	1.4×10^{-5}	1.1×10^{-5}	1.8×10^{-5}

Table 5.4: First 6 expansion coefficients for the g-factor trap [85].

Separating the electrodes are high-precision sapphire rings. They have been individually machined and matched to the electrodes to create a distance between the electrodes of exactly 0.2 mm. Between the anti-correction electrode and the corrections electrode, the distance is 0.4 mm to keep a perfect harmonic potential. The gap between the electrodes has a chicane-like shape to protect the spacers from charge pick-up. Sapphire balls separate the different sections of the split electrodes.
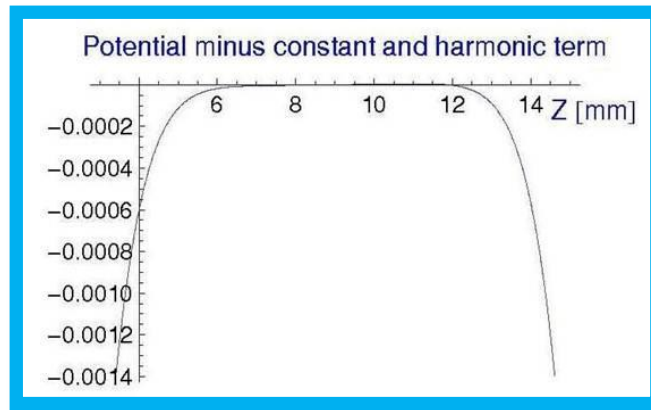
Figure 5.23: Anharmonic term in the trap potential along the longitudinal axis.

Laser access

There are two possibilities for laser access into the trap. A fibre-optic cable can be let into the trap and to a lens system mounted close to the quartz window. However, optical fibres are only an option for a limited range of wavelengths. Especially in the UV, e.g. for the 243 nm hyperfine transition of H-Like bismuth, no single-mode fibres exist. In this case, a laser can enter the trap directly from below. To this end, a straight path from below into the trap is kept optically clear.

Electronics housing

Above the electrode stack, space is reserved for the cryogenic electronics and optical detection. A copper frame to house the electronics and physically support the UHV chamber with the trap is shown in figure 5.24. This frame not only houses the electronics but also provides the thermal connection between the cryo-cooler and the Penning trap.
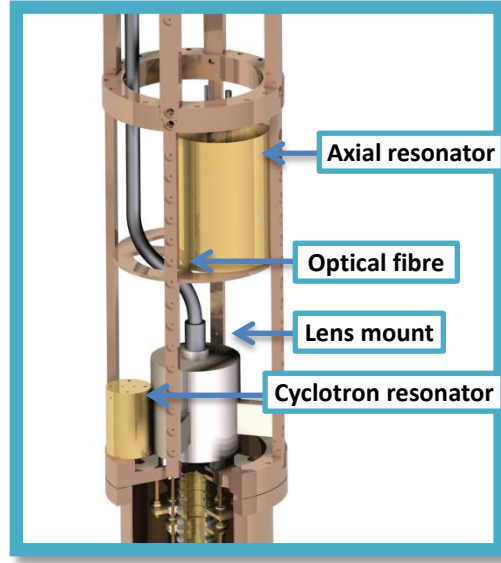
Figure 5.24: Electronics section on top of the UHV chamber. Resonators and the optical detection system are indicated.

5.4   Detection and measurements inside the trap

Detection of ions and the measurement of the *g*-factor take place non-destructively inside the precision section of the Penning trap. Particle number and ion species can be inferred from the motional frequencies. Fluorescence detection determines the splitting between Zeeman sub-levels, while an accurate measurement of the magnetic field requires a combination of the axial and the radial frequencies.

Axial detection

A dedicated resonance circuit in combination with a cryogenic amplifier has been designed to measure the axial frequency of the trapped ions. The resonance circuit consists of a high-quality resonator in parallel with the parasitic capacitance of the trap. For a 10 V potential, the axial frequency of a single $^{209}\text{Bi}^{82+}$ ion is 0.29 MHz. At 100V, the frequency for the same ion will be 0.92

MHz. During the experiment, the voltage can be tuned between these values to match the ion frequency to the resonance frequency of the resonance circuit.

Resonant LC circuit

The total parasitic capacitance consists of the capacitance of the pick-up electrode, the wiring, the amplifier input, the feedthrough between UHV chamber and electronics section and also the self-capacitance of the coil inside the resonator. Altogether this capacitance is estimated at 20 pF. Together with a resonator inductance of 15 mH, this will set the resonance frequency of the circuit to 0.29 MHz. Alternatively, with an inductance of 1.5 mH, the upper frequency of 0.92 MHz is achieved.

Assuming a single-particle amplitude of 50 micron at thermal equilibrium, the current induced in the pick-up electrode is 6 fA. To get at least 10 nV across the detection circuit, the parallel resistance of the circuit needs to be larger than 2 MΩ. For dip-detection, a minimum line width of 1 Hz is required. Using equation 2.16, this gives a minimum parallel resistance of 13 MΩ. The latter value being the largest, it is used to design the resonator.

For resonators at room temperature, the physical dimensions of the coil and the copper shield can be easily calculated [87]. The inductance of the coil at cryogenic temperature is only slightly different from the coil at room temperature. It is also assumed that the inductance is material independent. The Q-value of the coil, however, will change with temperature and choice of material. In fact, the Q-value does not only depend on the geometry and material, but for NbTi coils strongly depends on the quality of the connections [88].

	10 V	100 V	Copper 1	Copper 2	NbTi
Frequency	0.29 MHz	0.92 MHz	0.32 MHz	0.96 MHz	0.66 MHz
Capacity	20 pF	20 pF	47 + 11 pF	22 + 10 pF	22 pF
Inductance	15 mH	1.5 mH	4.4 mH	0.9 mH	2.6 mH
Resistance	13 MΩ	13 MΩ			8.9 MΩ
Q (x10³)	0.47	1.5	0.039	0.169	0.82
Windings			500	235	225
Shield diameter			76.2 mm	76.2 mm	76.2 mm
Shield length			101.6 mm	101.6 mm	101.6 mm
Coil radius			21.6 mm	21.6 mm	21.6 mm
Coil length			49 mm	64 mm	34

Table 5.5: Resonator design parameters. The first two columns give the requirements of the resonator for a 10 V and 100 V potential. The last three columns give the real values for different coils. For the copper coils, the capacity has two parts. The first capacity is the parallel capacity used to create the LC circuit, the 2nd capacity is the measured parasitic capacity of the coil.

Table 5.5 gives the design parameters of a resonator for both the 10 V and 100 V. The frequency and inductance of the final coil should be somewhere between these given values. For the Q-value, we use the 100 V as a minimum requirement for single-ion detection.

Figure 5.25: Superconducting resonator. The coil in the front is made out of superconducting NbTi. Behind is a gold plated copper resonator shield.
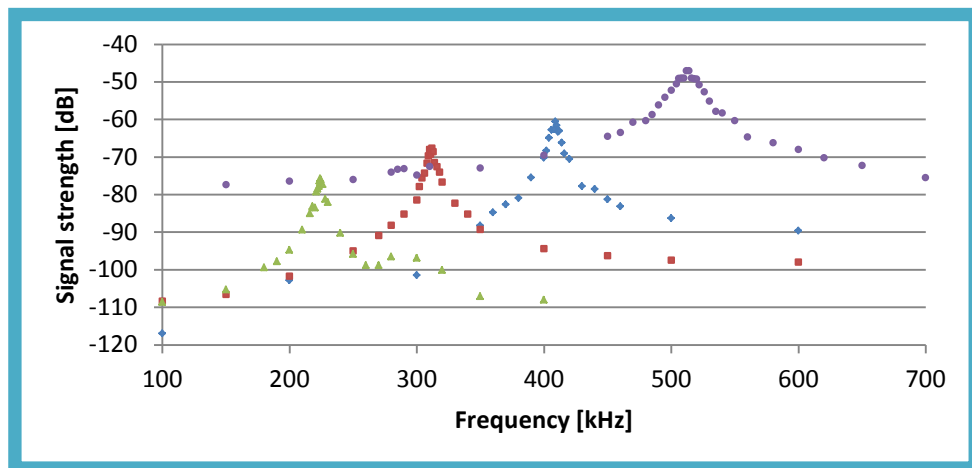
Figure 5.26: Resonance curves for copper coil 1 connected in parallel to a capacitance of 10 pF (purple), 22 pF (blue), 47 pF (red) or 100 pF (green).

As prototypes, several copper coils were constructed and tested. Figure 5.25 shows the resonator with the final NbTi coil in front. The shield is made out of gold-plated copper and the coil is wound around a thin Teflon tube. The relevant design parameters for the real coils and the results of the

79

measurements are given in Table 5.5. Figure 5.26 shows the measured resonance curves for the copper coil with 500 windings for different parallel capacitances. Using the resonance frequency for several capacities, both the inductance of the coil and the parasitic capacity of the coil were calculated. For a coil, the residual resitance can be calculated from measured values of Q, L and C:

$$R_{serial} = \frac{1}{Q}\sqrt{\frac{L}{C}} \qquad\qquad 5.2$$

For coil 1 the residual resistance is then $2 \times 10^2 \ \Omega$. A resistance of 150 Ω for coil 1 was measured across its terminals, which is in agreement with the experimental value for the residual resistance.

For a fixed capacity of the circuit, the resonance frequency depends on the coil length and the number of windings [87]. The Q-value depends on both the geometry of coil and shield as well as on the chosen material.
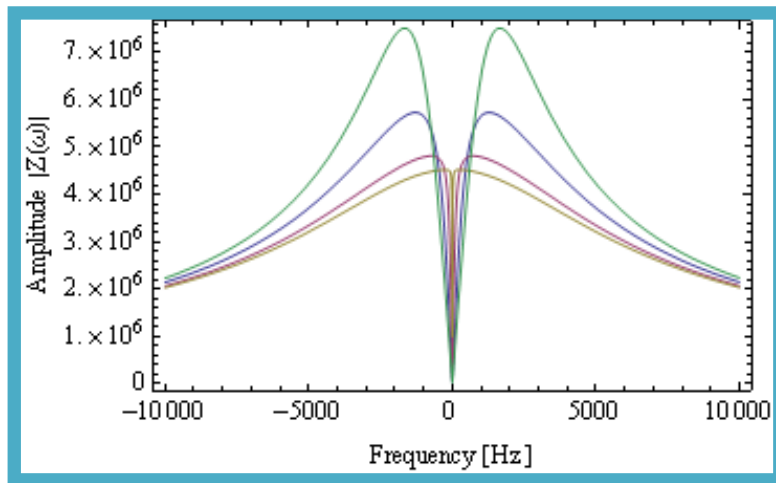
Figure 5.27: Simulated particle-detector interaction in the g-factor trap and resonance circuit for several particle systems. The picture shows the amplitude of the impedance of systems with 10 (yellow), 100 (red), 300 (blue) and 500 (green) trapped $^{209}Bi^{82+}$ ions. The 'Frequency' is the difference between the ion frequency and the resonance frequency of the LC circuit.

For copper non-superconducting coils, the required Q cannot be reached. Therefore, a NbTi coil was constructed as well. From table 5.5 it is clear that this greatly improves the Q-value of the resonator. A value of 820 has been reached. As discussed in section 2.4, a particle in a Penning trap can be described by an equivalent series RLC circuit. In parallel with the tank circuit this leads to a resonance peak with a dip at the frequency of the ion. This is shown for $^{209}Bi^{82+}$ ions brought in resonance with the g-factor resonator in figure 5.27. The amplitude of the impedance was simulated for different ion

numbers. When more than 1 ion is trapped, the width of the 'dip' scales with the number of ions. This can be used to measure the number of trapped ions. For small particle numbers (N) equation 2.16 becomes [34]:

$$\Delta v = \frac{N}{2\pi} \frac{R_p q^2}{mD^2} \qquad\qquad 5.3$$
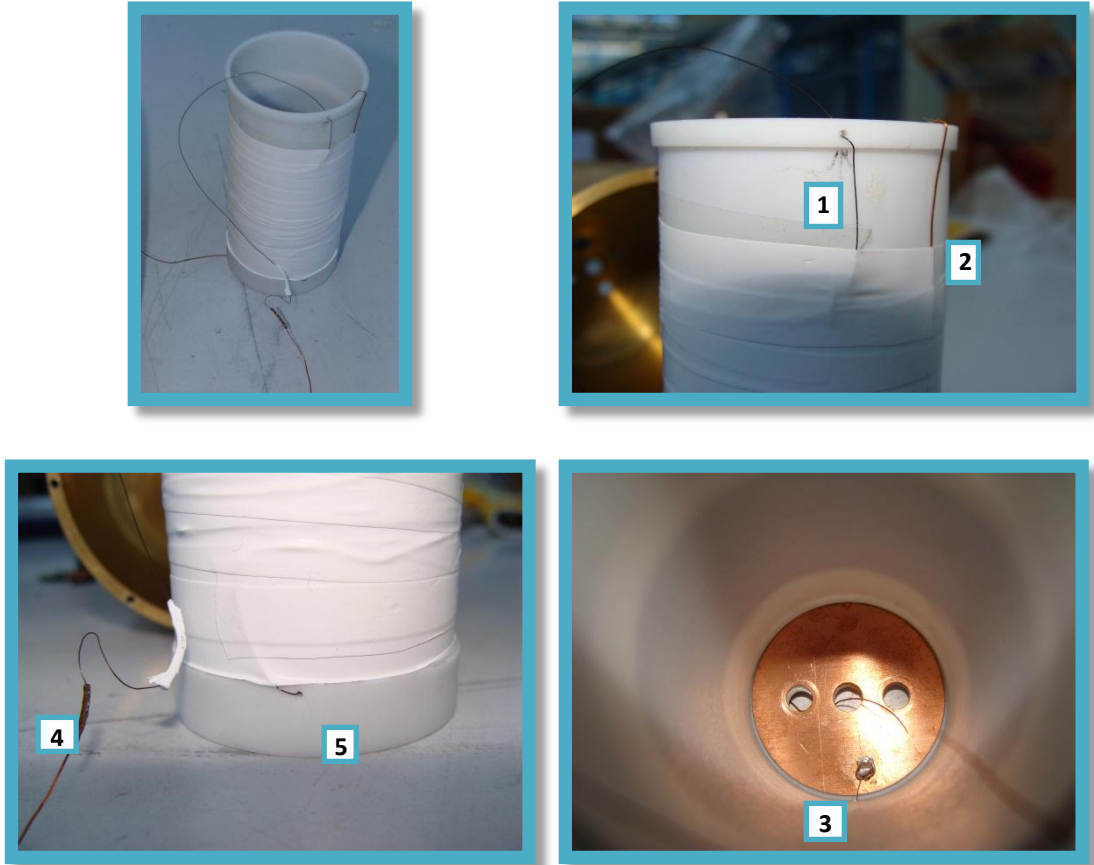
Figure 5.28: Overview of the connections to the axial superconducting coil. Clockwise, starting at the top-left picture. The NbTi coil is wound around a PTFE body, and fixed to this body with PTFE tape. Connections to the pick-up electrode (1) and from the tap point to the amplifier (2). The ground lead is soldered onto the copper ground plate (3). The pick-up lead is fixed to a copper wire (4) and the ground lead enters the coil body (5).

Broadly speaking, two aspects of the resonator could further improve its quality. First of all, the copper shield can be replaced with a NbTi shield. Also the connections to the coil can still be improved upon in several ways. These possibilities are labelled in figure 5.28. The superconducting material is connected with copper wires to the outside. Thicker copper wires will reduce the parasitic resistance of the copper[88]. The entire NbTi wire should also be firmly attached to the Teflon tube for better

thermalisation. Currently, the coil is grounded straight, with the NbTi wire, to the shield. This means that part of the NbTi is hanging loose here as well. First connecting the NbTi wire to a copper wire and then attaching the copper wire to the shield can remedy this. The same goes for the connection from the pick-up electrode to the coil. This last connection and the connection between tap point and amplifier could be improved with a thicker copper wire as well.

Amplifier
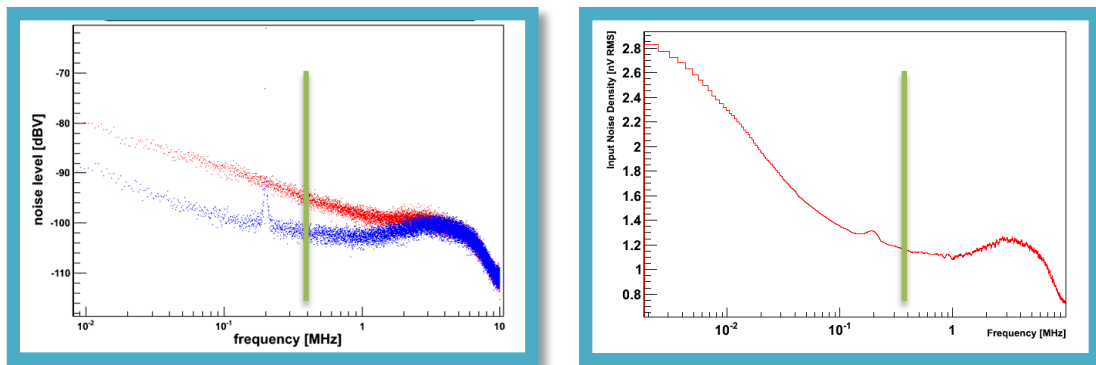
Figure 5.29: Input voltage noise for the CF739 FET as a function of frequency. On the left, the red data give the input noise at room temperature while the noise at 4 Kelvin is in blue. The peak in the blue series at 200 kHz is a reference signal. On the right is the input noise in $nV/\sqrt{Hz}$ at 4 Kelvin. The bump around 200 kHz is a leftover of the reference signal. The drop at the end of the data series in both graphs is a cut-off from the electronics and does not represent the behaviour of the FET. The green line at 400 kHz marks the axial frequency.
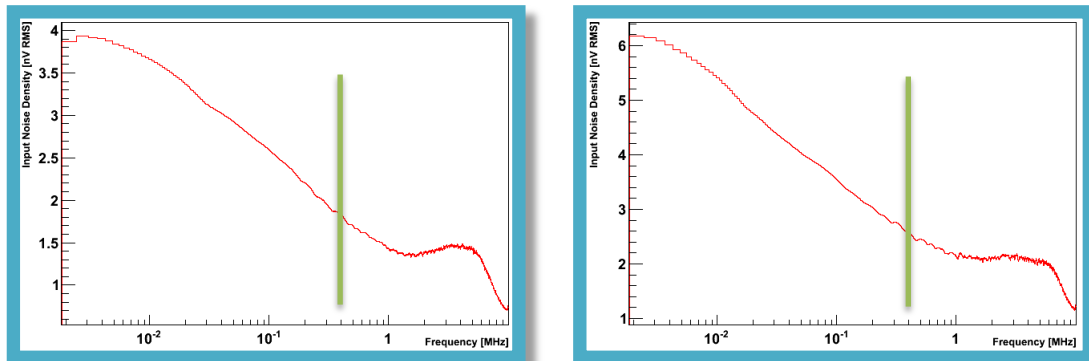
Figure 5.30: Input voltage noise for the 3SK164 (left) and 3SK166 (right) FET's as a function of frequency. The input noise is given in $nV/\sqrt{Hz}$ at 4 Kelvin. The drop at the end of the data series in both graphs is a cut-off from the electronics and does not represent the behaviour of the FET. The green line at 400 kHz marks the axial frequency.

The axial amplifier is built around the CF739 dual-gate field effect transistor (FET). An important parameter for these transistors is the input noise which is amplified together with the signal throughout the amplifier. Especially the input noise on the first stage is important as it will be

amplified at every stage. The signal strength for a single particle will be roughly 10 nV. This limits the allowed input noise to only a few nV.

The input noise is measured by dividing the background noise at the output of the amplifier with the amplification factor of the FET. This amplification factor is measured by comparing a known signal, supplied at the input, to the amplified signal at the output. Figure 5.29 and figure 5.30 show measured input noise for several transistors. For low frequencies, the input noise behaves as pink noise. It is inversely proportional to the frequency. At large frequency, frequency independent white noise dominates. For reliable operation the axial signal should be in the white noise dominated domain. In the case of the CF739, the data show that at 4 Kelvin this is the case for a 400 kHz axial frequency. The input noise density is here $1.2 \ nV/\sqrt{Hz}$. Both the 3SK164 and 3SK166 FET still suffer from pink noise at the axial frequency.

Another important parameter is the power dissipation inside the circuit. Since the power dissipation is equivalent to a heat source, it should be kept to a minimum. The main source of heating is the drain current. This gives the power dissipated in the amplifier:

$$P = I_D V_{DS},$$
5.4

with I_D and V_{DS} the drain current and drain-source voltage, respectively. As a rule of thumb, the drain current should be approximately 3 mA.
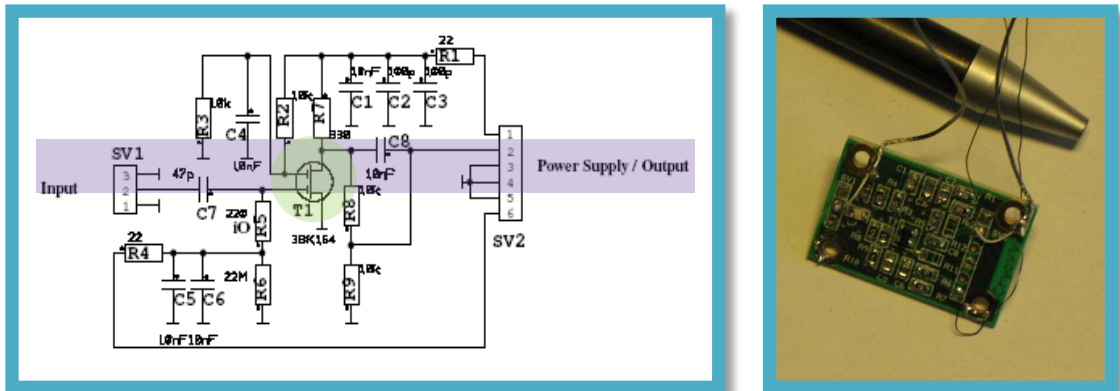
Figure 5.31: Single-stage cryogenic amplifier. In the circuit diagram (left) the FET is highlighted in green, while the flow of the signal is highlighted in purple. The picture of the amplifier board is on the right.

The cryogenic amplifier consists of two stages. The first stage is a simple transistor amplifier. Its purpose is to amplify the voltage signal. The second stage is a buffer stage. Its voltage amplification is close to 1 but it matches the output impedance of the amplifier to the signal cables leading to the

room temperature electronics. Figure 5.31 shows the first stage circuit and amplifier board. RC filters ensure stable bias conditions. At 4 Kelvin, a voltage gain of 4.9 was measured. The drain current was measured to be 2.2 mA and the power consumption then is 11 mW.

Figure 5.32 shows the circuit diagram for the complete cryogenic amplifier, including the second buffer stage. Schottky diodes protect the input and output of the amplifier against voltage spikes. The physical board is shown in figure 5.33. The stand-alone amplifier has been tested at room temperature. A maximum voltage gain of 3.7 and power consumption of 21.6 mW was measured[89]. At 4 Kelvin the amplifier has only been tested in combination with the coil.
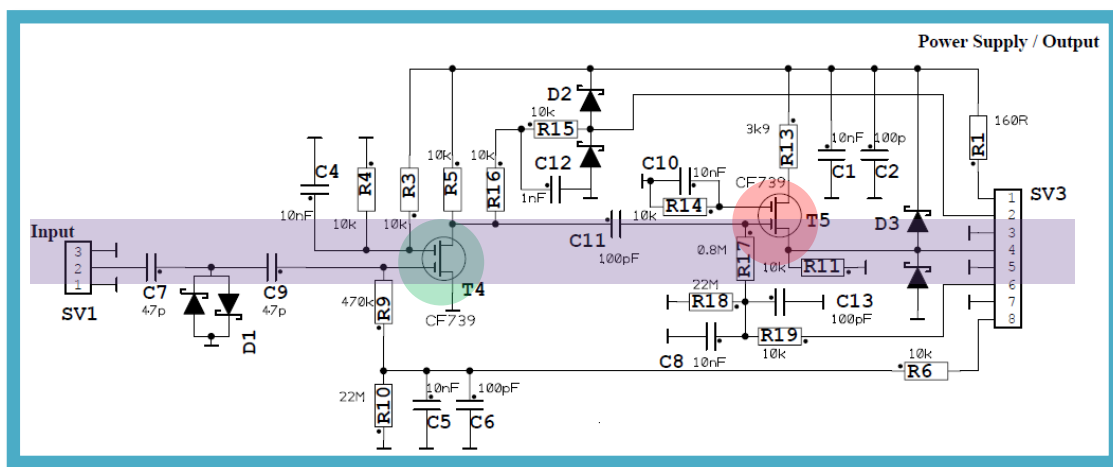
Figure 5.32: Two stage axial signal amplifier. The first amplifier stage is highlighted in green, while the buffer stage FET is highlighted in red.
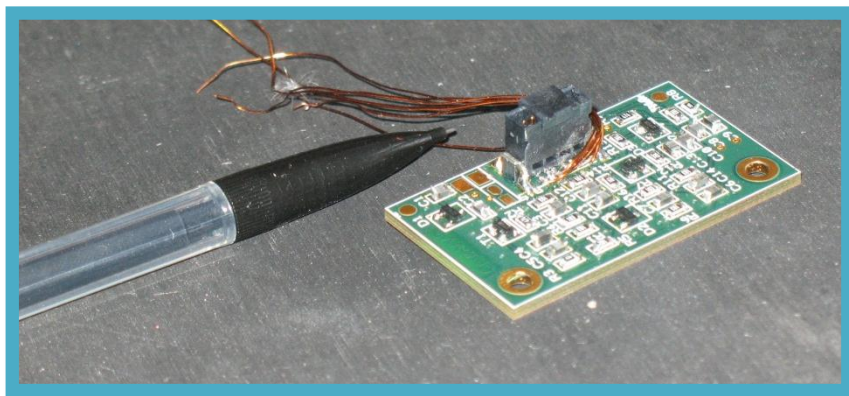
Figure 5.33: The two stage cryogenic amplifier board. Copper wires are attached as temporary connection. In the final implementation the board is connected by the plug (black) soldered on top of the board.

Cyclotron frequency measurement
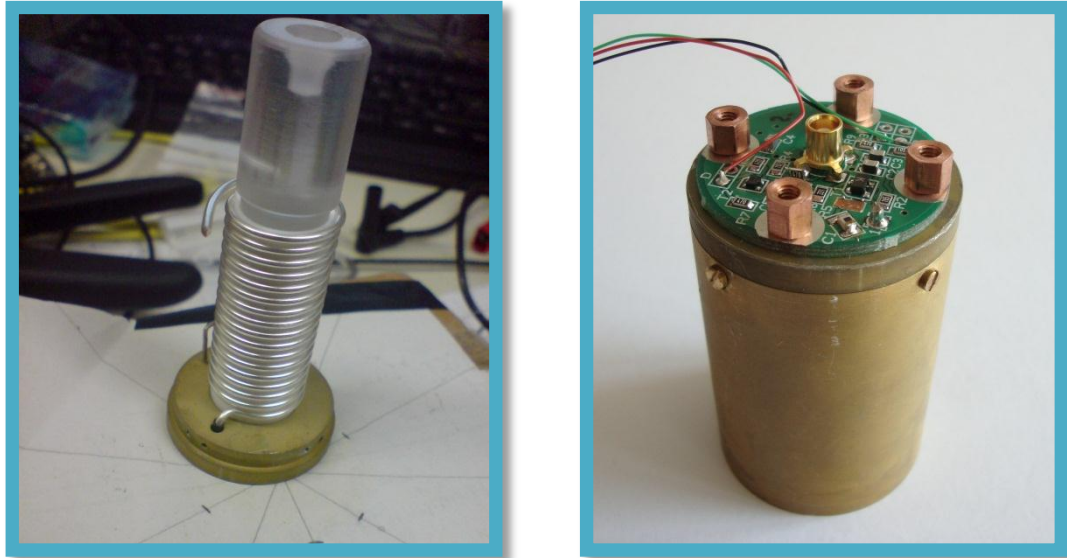
Figure 5.34: Cyclotron resonator coil (left) and the amplifier mounted on top of the resonator (right).

The development of the detection circuit for the cyclotron frequency was the subject of the bachelor thesis of Markus Huellen [90]. Pictures of both the coil and the amplifier are shown in figure 5.34. This circuit was designed for Ar^{13+} ions in a 7 T magnetic field. The cyclotron frequency for this system is 35 MHz.

At cryogenic temperature, the resonance frequency of the coil was measured at 34.7 MHz with a Q-value of 490. The amplifier again has 2 stages. The first stage is based on a single 3SK166 dual-gate FET and the second stage uses an NE3508 FET. A voltage gain of $G = 3$ was measured at cryogenic temperature.

The cyclotron frequency depends on the magnetic field and the mass-to-charge ratio of the ion. Both cannot be changed during the experiment. In the case of the cyclotron frequency the ion cannot be tuned to the resonance circuit. Therefore the circuit must be tuned to the ion instead. There are 2 shifts that should be taken into account: temperature shifts and difference in m/q for different ions.

First of all, the cryogenic frequency will be different from the design frequency. To compensate for this, a variable capacitor has been included that allows a frequency shift of the entire circuit of up to 800 kHz.

With different ions the mass-to-charge ratio is also different, for example $^{40}Ar^{13+}$ has $m/q = 3.1$ and $^{209}Bi^{82+}$ has $m/q = 2.55$. This is a 17% difference and this in turn changes the cyclotron frequency by

17% or 6 MHz. The simple variable capacitor will not be enough. The tuned circuit could be replaced for each new ion species. Alternatively, an additional tuning circuit, similar to the circuit in earlier *g*-factor experiments can be implemented [91].

Fluorescence

For a cloud of N ions, in a laser field with intensity I_L, the scattering rate is given by [92, 93]:

$$\gamma_p = N \frac{S_0 \, {}^\gamma/_2}{1 + S_0 + \left(\frac{2\delta}{\gamma}\right)^2} \qquad\qquad 5.5$$

Here γ is the decay rate of the state, δ is the detuning of the laser and $S_0 = I_L/I_s$ is the saturation parameter. For the remainder of this discussion we assume that the laser is on resonance, so that $\delta = 0$. The saturation intensity depends on the wavelength (λ) and lifetime ($\tau = 1/\gamma$) of the transition such that:

$$I_s = \frac{2\pi^2 \hbar c}{3\lambda^3 \tau} \qquad\qquad 5.6$$

And with the decay rate, or transition probability, for a magnetic dipole (M1) transition between two hyperfine states, given by [94]:

$$\gamma = \frac{32\alpha\pi^3 \hbar I (2\kappa + 1)^2}{27\lambda^3 m_e^2 c^4 (2I + 1)} \qquad\qquad 5.7$$

Here $\kappa = \sqrt{1 - (Z\alpha)^2}$. Table 5.6 lists the hyperfine transitions for several isotopes of interest. In particular ^{209}Bi is a good candidate for the *g*-factor experiment, as both for the H-like and Li-like state the hyperfine transition are within the optical regime.

For ^{207}Pb^{81+}, ^{235}U^{91+} and ^{209}Bi^{80+} the transition is easily saturated. In the case of $S_0 = 1$, equation 5.5 becomes simply:

$$\gamma_p = N \, {}^\gamma/_4 \qquad\qquad 5.8$$

When the intensity of the laser is much lower than the saturation intensity, equation 5.5 approaches:

$$\gamma_p = N \frac{3\lambda^3}{4\pi^2 \hbar c} I_L \qquad\qquad 5.9$$

The expected scattering rates for the different ions are listed in table 5.6.

Isotope	λ (nm)	γ [1/s]	I_s	γ_p [1/s]
B-Like $^{40}Ar^{13+}$	441.255 68(26)	104.5	25,3 mW/m^2	26×10^4
H-Like $^{207}Pb^{81+}$	1019.5(2)	20	18 μW/m^2	$5,0 \times 10^4$
H-Like $^{209}Bi^{82+}$	243.87(2)	2849	500 mW/m^2	$7,1 \times 10^6$
H-Like $^{235}U^{91+}$	1538*	9	3 μW/m^2	$2,2 \times 10^4$
Li-Like $^{209}Bi^{80+}$	1514	12	7 μW/m^2	$3,0 \times 10^4$

Table 5.6: Measured values for the ground-state hyperfine splitting in H-like and Li-like heavy ions. For ions labelled with an *, only a theoretical value is available [55, 56, 95-97]. Wavelength (λ), transition probability (A) and saturation intensity I_s are given. Also the scattering rate for 10^4 ions is calculated at saturation. For H-Like bismuth it is assumed that a laser intensity of 10 mW/m^2 is used.

Fluorescence detection

Fluorescence detection close to the trap yields the highest detection rates. However, the cryogenic environment and the strong magnetic field severely limit the choice of detector. At the same time, different detectors are sensitive to different wavelengths.

Acceptance and intensity

With only an extreme Zeeman sub-state probed, the ions emit circularly polarised light. The ions' magnetic moment aligns itself with the magnetic field axis. This light is emitted anisotropically. In particular, for these transitions, the emission is proportional to [85]:

$$I(\theta) \sim 1 + cos^2 \theta \qquad\qquad 5.10$$

Θ is the angle between the outgoing photon and the magnetic field axis. In order to obtain the rate on a detector (I_D), this expression must be integrated over the solid angle of the detector and normalised with the full solid angle of emission:

$$I_D = Rate \frac{\iint_0^{\theta max} 1 + cos^2 \theta \; dcos\theta d\varphi}{\iint_{-\pi}^{\pi} 1 + cos^2 \theta \; dcos\theta d\varphi} \qquad\qquad 5.11$$

The normalisation factor is obtained by performing the integration over all θ and φ. Its value is $5\frac{1}{3}\pi$. Also the fluorescence rate is included in this equation. This rate depends on the laser intensity and the lifetime of the excited state. It also depends on the transmission efficiency between the source and the detector and is therefore not necessarily equal to γ_p.
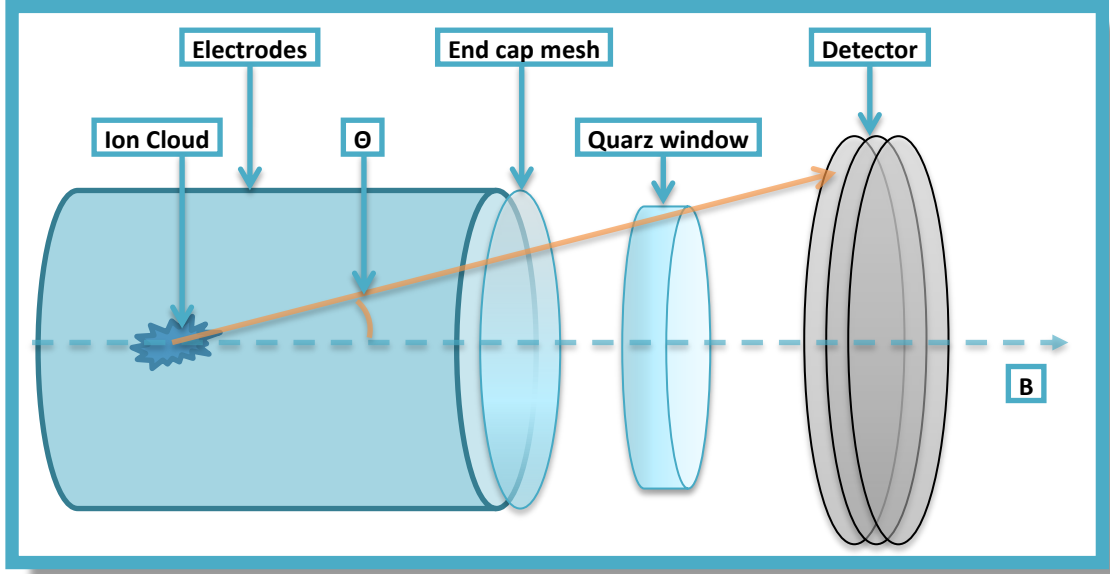
Figure 5.35: Optical detection scheme. The dashed line is the magnetic field axis (B). The cone of fluorescence light (orange arrow) is defined by its polar angle (ϑ).

For the basic configuration of the *g*-factor trap, as shown in figure 5.35, the detector covers the full azimuthal angle. The polar angle is limited by the geometry of the trap and the quartz window. For window size D and a distance z from the ion cloud, the polar angle is simply given by $\theta_{max} = atan\, D/2z$. Therefore, equation 5.11 becomes:

$$I_D = \frac{2Rate}{5\frac{1}{3}}\left[cos\,\theta\big|_0^{\theta_{max}} + \frac{1}{3}cos^3\,\theta\big|_0^{\theta_{max}}\right] \qquad\qquad 5.12$$

For $D = 25.4\,mm$ and $D = 17.3\,mm$, $\theta_{max} = 0.63$ and $I_D = 0.3 \cdot Rate$. The intensity at the detector is further modified by the transmission of the end-cap mesh and the quartz window. The transmission of the first is estimated at 64%, while the latter is estimated to transmit 98%. On top of this, also the quantum efficiency (ϵ) of the detector should be taken into account. So the effective rate on the detector is:

$$I'_D = 0.23 \cdot \epsilon \cdot \gamma_p \qquad\qquad 5.13$$

Several modifications to the basic geometry are possible. For instance, an MCP with a central hole can be used, where the probe laser enters the trap through this hole. In this case, the centre of the detection surface is not available for fluorescence detection. Thus, this 'hole' must be subtracted from

88

equation 5.13. Depending on its size, I'_D may be reduced by as much as 20%. The easiest way to calculate the reduction in rate is by introducing a minimum angle (θ_{min}) in equation 5.12:

$$I_D = \frac{2Rate}{5\frac{1}{3}}\left[cos\,\theta\,|_{\theta_{min}}^{\theta_{max}} + \frac{1}{3}cos^3\,\theta\,|_{\theta_{min}}^{\theta_{max}}\right] \qquad\qquad 5.14$$

A similar situation occurs when the laser is introduced from the bottom. The laser intensity is many orders of magnitude larger than the fluorescence light and the area on the detector with the laser becomes blinded.

Backscattering

The reflection of light from the quartz window is estimated at % of the incoming light. When introduced through a fibre from the top, some of the laser light will therefore be reflected back into the detector. For example, assuming a laser intensity of 1mW and with the energy of a single photon as $E = hc/\lambda$. So a 244 nm photon carries an energy of $8.1 \times 10^{-19}J$. This leads to a reflection rate of order $10^{13}\ s^{-1}$ in the case of H-like bismuth. The same calculation for the H-like uranium case yields a reflected rate of $10^{13}\ s^{-1}$ as well. Clearly the reflection rate at the quartz window alone will drown the fluorescence signal.

The easiest solution to these problems is to periodically chop the laser beam and to only measure the fluorescence light in the laser-off periods. The chopping period must be matched to the lifetime of the state under observation. The trade-off is that the effective scattering rate will go down with at least a factor 2.

Detectors

The choice of the fluorescence detector depends on the wavelength of the hyperfine transition of the ion in the trap. Other important considerations are the magnetic field and the cryogenic temperatures that may influence the detector operation. Detectors based on secondary charged particles often function poorly in strong magnetic fields while semi-conductor devices may require additional local heating. Limits on quantum efficiency and maximum count rates should be considered as well. Table 5.7 shows how several detection options respond to the environment of the Penning trap.

For H-like bismuth the hyperfine transition is well inside the UV domain. For this wavelength, a micro channel plate (MCP) may be used. This detector has the advantage of a large active area, increasing the solid angle for detecting photons. Although MCP's are meant for charged-particle detection,

special coating will convert UV photons into an electron avalanche as well. Functionality within a magnetic field is limited to roughly 1T though [98, 99]. This means that the *g*-factor magnet would have to be retuned for this detector. The cryogenic temperatures at the location where the photons will be detected increases the resistance across the MCP and so the current through the MCP is decreased and the channels of the MCP will gain a considerable dead-time. As a result, the maximum count rate will be lower [100-102]. However, the expected photon rate will still be within the accepted rate for this experiment.

Detector type	Optical range	suitability with B- field	Cryogenic issues
MCP	UV only	Bad performance above 1 T	Increased dead time
Photodiode	Most wavelengths	Mostly independent of B-field	GaAs & SiGe only
Lens and fibre	Visible light	Independent of the B-field	No problem

Table 5.7: Overview of detector types available to the g-factor experiment.

Different photodiodes exist for different wavelengths. In essence they have 2 drawbacks. The suitability at cryogenic temperature depends strongly on the semiconductor material and their active surface tends to be small. Detectors based on Ga are available, improving the cryogenic response. Also, a local heating device could be installed to improve their performance. The second problem can be solved by building an array of detectors, provided they don't have a large inactive area. Alternatively, a lens can focus the fluorescence light on the detector. It requires that the diode is fast enough for the required detection rate. Avalanche photo diodes (APD) convert photons into charge and provide additional internal gain through avalanche multiplication. For single photon detection, APD's are best suited. Table 5.8 provides an overview of different diodes for different wavelengths. In general, every individual diode must be tested for its cryogenic suitability. But in particular the Si-based detectors require local heating.

Type	Range [nm]	Semiconductor	Manufacturer
SG01	215 - 360	SiC	sglux
TW30SX	215 - 387	TiO_2	sglux
C30645	900 - 1700	InGaAs APD	Perkin Elmar
AG38	290 - 375	GaN	sglux
G196x	190 - 550	GaP	Hamamatsu
S534x &S907x	200 – 1000	Si APD	Hamamatsu

Table 5.8: Overview of photo diodes across the entire wavelength range of interest to the g-factor experiment.

A lens in combination with an optical fibre allows light detection outside of the B-field and at room temperature. Unfortunately this is only possible for wavelengths for which optical fibres exist. In particular, for UV light this will be a problem. For measurements on $^{40}Ar^{13+}$, such a set-up has been constructed [85].

5.5 Operation

Ion lifetime

Ions can change their charge state by exchanging charges in collisions with other particles. If this happens for the ions in the *g*-factor trap, they would be effectively lost for the experiment. Other processes that cause ion losses include trap imperfections and energy transfer during elastic scattering within the ion cloud. The *g*-factor trap is designed with a minimum of imperfections and the electric and magnetic fields will be strong compared to the amount of energy that can be accumulated by the ions during elastic scattering. So, in the case of the *g*-factor experiment the dominant process by which the highly-charged ions change their charge state is through collisions with the neutral rest gas in the trap vacuum. The cross-section for this form of electron capture is approximated at low kinetic energies by the Schlachter formula [103]:

$$\sigma = 1.43 \times 10^{-16} q^{1.17} V_I^{-2.76} \ [m^2] \qquad\qquad 5.15$$

Here V_I is the ionisation potential of the rest gas in eV and q is the charge state of the ion in unit charges. At cryogenic temperatures most of this rest gas consists of hydrogen molecules. The ionization potential of H_2 is 15.44 eV [104]. With this cross-section, the lifetime (τ) of the ion can be calculated for a density of the rest gas n and relative velocity v_r:

$$\tau = \frac{1}{\sigma n v_r} = \frac{k_B T_r}{\sigma P} \left(\frac{3 k_B T_i}{m_i} + \frac{3 k_B T_r}{m_r} \right)^{-1/2} \qquad\qquad 5.16$$

T_i and T_r are the temperatures of respectively the ions and rest gas. The masses are m_i and m_r and P denotes the pressure. In the case of the g-factor experiment, gas can only enter and leave the vacuum chamber through a relatively small aperture at the bottom. Furthermore, if access into the trap chamber is only possible through a narrow but long tube, movement of neutral particles into the trap vacuum will be limited. Therefore it is safe to assume that the rest gas has a temperature of 4 Kelvin, just like the ions. The straight and open path into the trap, required for ion injection and laser access limits the quality of the vacuum. How much exactly is not yet clear. A conservative pressure of 10^{-13} mbar gives for $^{235}U^{91+}$ ions a lifetime of 28 minutes. With a pressure of 10^{-15} mbar, the lifetime becomes 48 hours.

Measurement time

During the double-resonance experiment the magnetic field should be monitored at regular intervals to compensate for small drifts of the magnetic field. The magnetic field can be accurately determined from the motional frequencies of a single ion. Therefore, the spectroscopy measurements on a cloud should be alternated by frequency measurements on a single ion. The ion cloud may be recycled by moving it back and forth between the capture section and the spectroscopy section. It is important to remember that, depending on the quality of the vacuum, most of the ions will maintain their charge state for at least 20 minutes. Therefore, in the worst case scenario this limit on the lifetime of the charge state defines the experimental cycle.

The double-resonance experiment involves measuring the fluorescence signal over a range of microwave frequencies. Based on previous *g*-factor experiments, roughly 14 individual Zeeman-transition measurements at 15 different frequencies are necessary for a single frequency scan [7]. By repeating the same frequency scan 10 times at e.g. different microwave powers to study systematic errors, 2100 data points will be measured to fix a single microwave frequency.

This experiment is sensitive to 20% of the solid angle. Also, without optical pumping, slightly more than 10% of the ions will be in the Zeeman sub-state we want to probe. Between the different ions listed in table 5.6, H-like uranium has the lowest scattering rate. For a scattering rate of order 2.2 s^{-1} per ion in the case of H-like uranium, this is equivalent to 0.44×10^3 individual Zeeman transition measurements per second. A single frequency scan, requiring 15x14 measurement points, will take 0.5 seconds. To reduce the influence of reflections, the beam must be chopped. If this is done at a speed that is comparable to the lifetime of the excited hyperfine state, roughly 2 seconds will be required. With 15 different frequencies per sweep, this is equivalent to 140 ms to measure the transition probability at one single frequency.

The required microwave frequency is in the order of 65 GHz. A relative precision of the microwave field of 10^{-9} implies a maximum width of 65 Hz for the microwave peak. This limits the speed with which the microwave generator can change the frequency to 16 ms. Since, during a frequency sweep, 140 ms of measurement time per frequency is necessary to get enough statistics, the microwave field can be changed fast enough to fit a single sweep in a 10 minute cycle. This amounts to 2 hours of effective measurement time to obtain a single atomic *g*-factor.

Experimental cycle

Figure 5.36 shows the experimental working cycle during the *g*-factor experiment. The start of the cycle should be matched relative to the ESR/HITRAP trigger. One cycle consists of the following steps:

1. Creation and injection of electrons for cooling. These electrons are created within the electrode stack by the field-emission point, so they don't need to be injected into the magnetic field.

2. The electrons are trapped in the nested traps of the capture section. Here they will cool through the emission of synchrotron radiation.

3. Ions, coming from the Cooler trap will be injected into the magnetic field from below. They have a transport energy of 5 keV/q. Most of this energy will be reduced in the injection line and by deceleration against the trap entrance. When they enter the capture trap, the ions should have a remaining energy of 100 eV/q. The HV electrode at the far end of the trap will be raised to block particles at this energy.

4. As the ions enter the electrode stack, the potential on the first HV electrode is raised to trap the ions. At this stage, the ions will lose their kinetic energy against the cold electrons.

5. With about 10 eV/q remaining, the electrons will be purged from the trap. At this stage, resistive cooling will take over. The ions can be assembled in between 1 and 4 sub-traps.

6. Less than 10 ions are separated out of the capture section and transported into the spectroscopy section of the trap. Here they are cooled, using resistive cooling, to 4 Kelvin. By measuring their motional frequencies a precision measurement of the magnetic field will be performed.

7. A large number of ions are transported into the spectroscopy section of the trap. Now the double-resonance spectroscopy measurement is performed. Depending on the number of ions captured, only a part of the captured bunch can be transported for spectroscopy and thus the experiment may be repeated several times per experimental cycle. In this case, the magnetic field should be measured between each sub-cycle.

93
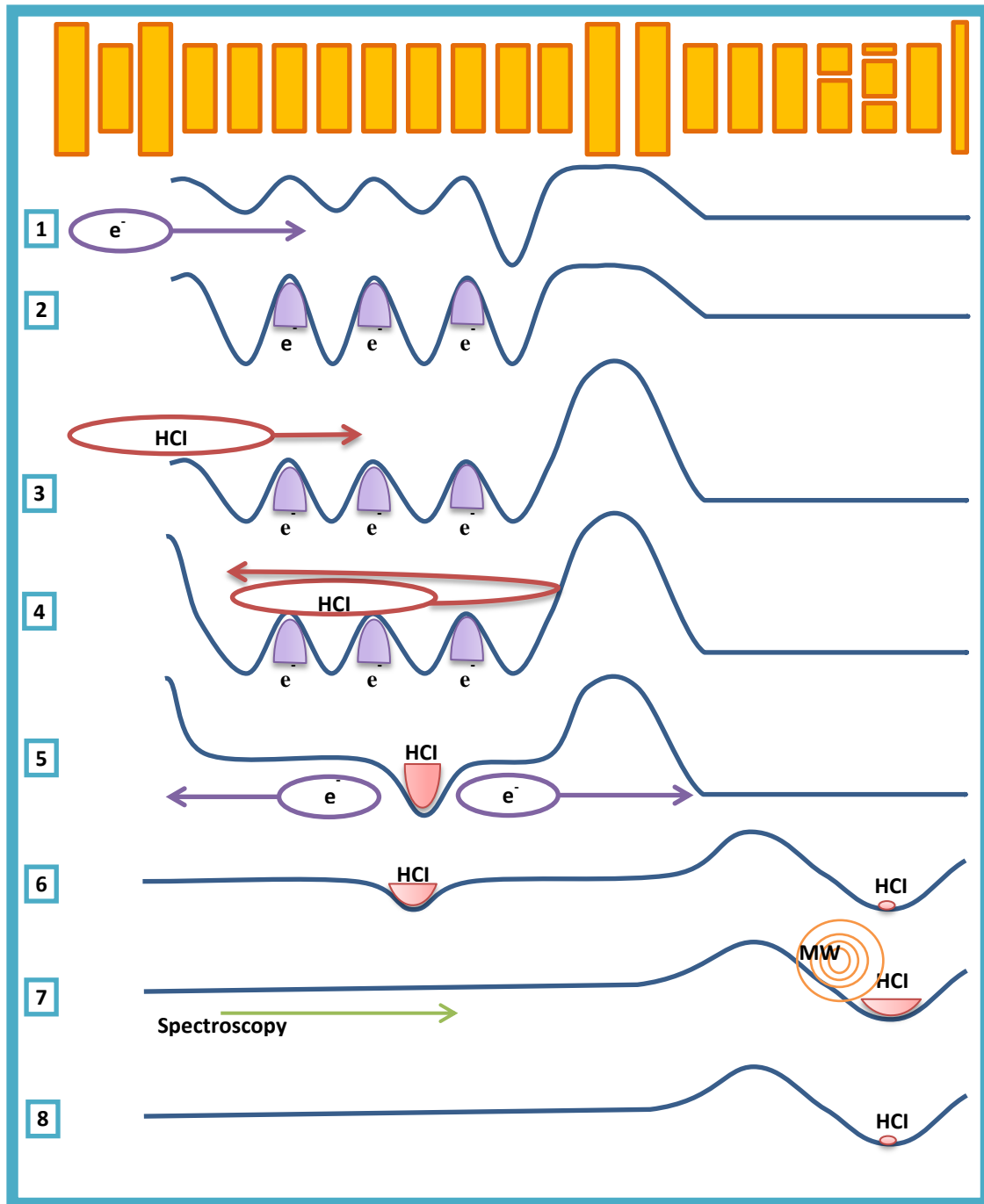
Figure 5.36: Working cycle for the g-factor trap. At the top is a sketch of the electrode stack. The most important steps during the experiment are schematically drawn. In (1) the electrons are created at the electron source. Then the nested traps are closed (2) and subsequently highly-charged ions (HCI) are injected into the trap (3). As the entrance electrode is closed (4), electron cooling starts. Afterwards, the electrons are purged from the trap (5) and resistive cooling takes over. A few ions are split off into the spectroscopy section to measure the magnetic field (6), and then the other ions are transported there as well for the double-resonance experiment (7). Finally, most ions are removed and the magnetic field is measured again.

8. At the end of the cycle, all but a few ions are removed from the trap. With these ions, the magnetic field is measured again in order to correct for small instabilities in the magnetic field.

6 Summary and Outlook

6.1 Summary

The work done within the scope of this thesis is the first step towards a *g*-factor measurement in heavy highly-charged ions. It includes the design and construction of the *g*-factor Penning trap, its electronic detection circuit and the injection of ions into the trap itself.

The behavior of a charged-particle plasma inside the Cooler trap was studied. At the same time its ion detection electronics has been tested and improved and the commissioning of the Cooler trap was started. Electrons have been trapped inside the Cooler trap successfully.

The relevance of a *g*-factor measurement of heavy ions to fundamental physics has been motivated in the first chapter. The other chapters discuss the technical and experimental details of the *g*-factor measurement. The Penning trap in general is discussed in Chapter 2 and the Cooler trap and *g*-factor trap are discussed in chapters 4 and 5, respectively. An important aspect of precision experiments on heavy highly-charged ions is the production of said ions. Chapter 3 deals with the production and deceleration of heavy highly-charged ions.

6.2 Current status

Cooler trap

At this point in time, the Cooler trap is warmed up and disassembled in order to make a few technical improvements. The entire connection system is being upgraded to improve signal transmission between the cryogenic region and the room temperature electronics. Also the cabling and feedthroughs are being prepared to allow the trap to float at high voltage. Also additional HV protection will be added to the interface board (Figure 4.20) in order to protect the amplifier from accidental discharges. Finally, on the entrance of the trap, at the side of the RFQ, a ring will be mounted to the entrance of the connection plug (Figure 4.6). This ring will allow inductive pick-up of electrons leaving the trap. The location of this ring is closer to the trap than the existing Faraday cup and the magnetic field at this location is a factor 10 higher.

These improvements should take a few more weeks. Then the trap will be reassembled and cooled down to cryogenic temperatures. At this time, it is important to align the magnetic field with electric

field of the electrodes. Then, trapping of electrons will be repeated and another systematic study of the influence of the potential distribution on the trapping time should improve the lifetime of the electron cloud. For larger numbers of electrons, it should also be possible to detect the particles inductively. This way, the lifetime of the cloud can be measured without distortion from extraction losses. Also, inductive pick-up can be used to study the plasma modes of the cloud and thus measure its parameters like size, density and temperature.

Finally, ions will be trapped. At this stage ions can be created locally but EBIT ions will be available to the Cooler trap in a matter of months. With EBIT ions, trapping and cooling of medium-heavy highly-charged ions can be achieved. The heavy highly-charged ions will become available once the RFQ is commissioned. This may take 1 or 2 more years.

g-Factor experiment

The *g*-Factor trap will be assembled coming May. It will be possible to create ions up to boron-like argon inside the trap itself. These ions can be produced, trapped and measured upon without external sources or the injection line. Once these ions are created, the *g*-factor of $^{40}Ar^{13+}$ will be determined. For heavier systems, EBIT ions or HITRAP ions will be necessary and the beam line up to the *g*-factor trap and its injection line must be constructed. This should be possible within a year.

Only ions and charge states that have hyperfine transitions, accessible by lasers, between the ground state and the first excited state can be measured in this *g*-factor set-up. Also, optical detection must be possible for this particular wavelength. This last requirement can be relaxed by using a 'blind spectroscopy' method [105]. The *g*-factor trap can also be used for a Stern-Gerlach type measurement by replacing the ring electrode with an electrode made out of ferromagnetic material. The large size of the trap reducs systematic shifts due to the image-charge effect compared to existing traps [106]. Also, the experiment must be sensitive enough to distinguish and track several different Zeeman sub-states. Recent improvements in simple cryogenic detectors allow for relatively short measurement times and a *g*-factor measurement on a single ion may now also be possible within the time constraints of a beam time schedule [7, 107].

In conclusion, important progress has been made to test QED in the presence of strong electric fields. The future *g*-factor measurements at HITRAP will be sensitive to QED corrections at nuclear charges well outside the perturbative regime. At the same time, a combined measurement of the hydrogen-like and lithium-like *g*-factors can be used to disentangle QED effects and nuclear size effects to first

order. In general, with the strong influence of nuclear effects at high Z (see figure 1.8), nuclear properties are experimentally accessible with high precision as well.

A. Capture Trap

SECTION A-A

Notes:
- Inner diameter and heigth of the electrodes is most imprtant!
- Space between the C-electrodes should be 0,4 mm
- Space between the C-electrodes and the H-electrodes should be 0,7 mm
- Electrodes should be made to fit the vitronit rings such that these distances are achived.

Dimensions:
- 0,41 ± 0,02
- 0,7 ± 0,02
- 0,4 ± 0,02
- 0,4 ± 0,02
- 0,4 ± 0,02
- 0,4 ± 0,02
- 0,4 ± 0,02
- 0,4 ± 0,02
- 0,4 ± 0,02
- 0,4 ± 0,02
- 0,7 ± 0,02

Electrode labels:
- High Voltage Electrode H8
- High Voltage Electrode H9
- Capture Electrode C10
- Capture Electrode C11
- Capture Electrode C12
- Capture Electrode C13 (Split Capture Electrode)
- Capture Electrode C14
- Split Capture Electrode C15
- Capture Electrode C16
- Capture Electrode C17
- Capture Electrode C18
- High Voltage Electrode H19

REVISION HISTORY

REV	DESCRIPTION	DATE	APPROVED

UNLESS OTHERWISE SPECIFIED
DIMENSIONS ARE IN MILLIMETERS
ANGLES ±X°
2 PL ±X.XX 3 PL ±X.XXX

	NAME	DATE
DRAWN	klmartje	06/28/11
CHECKED		
ENG APPR		
MGR APPR		

SOLID EDGE
UGS - The PLM Company

TITLE

SIZE A3 DWG NO

FILE NAME: DecaTrap.dft

SCALE WEIGHT: SHEET 1 OF 1

REV

First drawing (top):

REVISION HISTORY

REV	DESCRIPTION	DATE	APPROVED

Connector

A

A

SECTION A-A

14,13 ± 0,01

1,305 ± 0,01   1,305 ± 0,01

11,52 ± 0,10

27,49 ± 0,10

23,47 ± 0,10

17,513 ± 0,02

$\varnothing$ 1 ± 0,10 ⍌ 3

	NAME	DATE	**SOLID EDGE**
DRAWN	kbrantje	06/28/11	*UGS - The PLM Company*
CHECKED			TITLE
ENG APPR			electrode decatrap - C10, 11, 12, 14, 16, 17, 18
MGR APPR			

UNLESS OTHERWISE SPECIFIED
DIMENSIONS ARE IN MILLIMETERS
ANGLES ±X.X°
2 PL ±X.XX 3 PL ±X.XXX

SIZE A3   DWG NO   REV

FILE NAME: electrode_decatrap.dft

SCALE: WEIGHT: SHEET 1 OF 1

Title	Material	Comments
Capture Electrode - Unsplit	OFHC Copper	7 Pieces

Second drawing (bottom):

REVISION HISTORY

REV	DESCRIPTION	DATE	APPROVED

0,2 ± 0,05   A

Connector

Connector

A

14,13 ± 0,01

1,305 ± 0,01   1,305 ± 0,01

7,16 ± 0,10

27,49 ± 0,10

23,49 ± 0,10

17,513 ± 0,02

SECTION A-A

2 X $\varnothing$ 1 ± 0,10 ⍌ 3

2 X R 1 ± 0,1

12 ± 0,1

	NAME	DATE	**SOLID EDGE**
DRAWN	kbrantje	06/28/11	*UGS - The PLM Company*
CHECKED			TITLE
ENG APPR			Split decatrap electrode - C13, 15
MGR APPR			

UNLESS OTHERWISE SPECIFIED
DIMENSIONS ARE IN MILLIMETERS
ANGLES ±X.X°
2 PL ±X.XX 3 PL ±X.XXX

SIZE A3   DWG NO   REV

FILE NAME: electrode_decatrap_split.dft

SCALE: WEIGHT: SHEET 1 OF 1

Title	Material	Comments
Capture Electrode - Split	OFHC Copper	2 Pieces (4 halves)

Drawing 1 (Top)

6 X Ø 6 ± 0,10

Ø 1 ± 0,10
↧ 2

4,986 ± 0,010
3 ± 0,10
3,983 ± 0,10
1,003 ± 0,010

27,49 ± 0,10
23,47 ± 0,10
5,046 ± 0,010

50 ± 0,10

A

A

SECTION A-A

Drawing 2 (Bottom)

A

A

Capture Electrode
C10

HV Electrode
H8

6,5 ± 0,10
1,003 ± 0,01
1,3 ± 0,05
3,25 ± 0,10

27,4 ± 0,10
23,4 ± 0,05
10 ± 0,05

SECTION A-A

Ø 1 ± 0,10
↧ 3

Connector

Top drawing (High Voltage Electrode – Bottom):

REVISION HISTORY

REV	DESCRIPTION	DATE	APPROVED

6 X Ø 6 ± 0,10

75° ± 0,10

15° ± 0,10

0° ± 0,10

A

A

Ø 1 ± 0,10
↧ 3

Transport Electrode T7

HV Electrode H9

1 ± 0,05

6,5 ± 0,05

1,3 ± 0,05

0,7 ± 0,10

3 ± 0,10

1,25 ± 0,10

50 ± 0,10

27,43 ± 0,10

23,43 ± 0,10

10 ± 0,10

SECTION A–A

Connector

SOLID EDGE
UGS - The PLM Company

	NAME	DATE
DRAWN	kbrantje	06/28/11
CHECKED		
ENG APPR		
MGR APPR		

TITLE
High Voltage Electrode Bottom – H8

UNLESS OTHERWISE SPECIFIED
DIMENSIONS ARE IN MILLIMETERS
ANGLES ±X.X°
2 PL ±X.XX 3 PL ±X.XXX

SIZE A3 DWG NO REV

FILE NAME: electrode_capture_H8.dft

SCALE: WEIGHT: SHEET 1 OF 1

Title	Material
High Voltage Electrode – Bottom	OFHC Copper

Bottom drawing (Transport Electrode – T7):

REVISION HISTORY

REV	DESCRIPTION	DATE	APPROVED

A

A

End Tube Electrode S6

HV Electrode H8

8 ± 0,05

1,5 ± 0,05

1,305 ± 0,05

4 ± 0,10

27,48 ± 0,10

23,48 ± 0,10

17,519 ± 0,01

SECTION A–A

Ø 1 ± 0,10
↧ 3

Connector

SOLID EDGE
UGS - The PLM Company

	NAME	DATE
DRAWN	kbrantje	06/28/11
CHECKED		
ENG APPR		
MGR APPR		

TITLE
Transport Electrode – T7

UNLESS OTHERWISE SPECIFIED
DIMENSIONS ARE IN MILLIMETERS
ANGLES ±X.X°
2 PL ±X.XX 3 PL ±X.XXX

SIZE A3 DWG NO REV

FILE NAME: electrode_transport.dft

SCALE: WEIGHT: SHEET 1 OF 1

Title	Material
Transport Electrode	OFHC Copper

102

B. Spectroscopy Trap

SECTION A-A

Notes: This is the 'precision trap'.
- Inner diameter and heigth of the electrodes is most important!
- Space between electrodes S4 and S5 should be 0,4 mm.
- Space between the other electrodes should be 0,2 mm.
- Electrodes should be made to fit the saphire rings such that these distances are achived.

Copper Mesh S1-α

Insulators

Centre Electrode S3

Correction Electrode S2

End Cap Electrode S1

End tube Electrode S6

Anti-correction Electrode S5

Correction Electrode S4

	NAME	DATE
DRAWN	NP M. Brauri	05/28/11
CHECKED		
ENG APPR		
MGR APPR		

UNLESS OTHERWISE SPECIFIED
DIMENSIONS ARE IN MILLIMETERS
ANGLES ±X.X°
2 PL ±X.XX 3 PL ±X.XXX

SOLID EDGE
UGS - The PLM Company

TITLE
Spectroscopy Trap

SIZE	DWG NO		
A3			REV
FILE NAME: trap_no_ball.dft			
SCALE:	WEIGHT:	SHEET 1 OF 1	

REV	DESCRIPTION	DATE	APPROVED
	REVISION HISTORY		

103

Capture Trap Side

SECTION A–A

DETAIL B

Spectroscopy Trap Side

DETAIL C

104

Drawing 1

REV | DESCRIPTION | DATE | APPROVED

A
A

$6,22 \pm 0,010$
$1,505 \pm 0,1$
$0,702 \pm 0,1$

Correction Electrode; S4

End Tube; S6

$27,485 \pm 0,10$
$25 \pm 0,1$
$19,52 \pm 0,05$
$17,503 \pm 0,010$
$2,153 \pm 0,05$

0°
B
20°

$2,508 \pm 0,01$
$5,919 \pm 0,01$

SECTION A-A

$\emptyset \; 1 \pm 0,10$
$\downarrow 3$

End Tube side

DETAIL B

	NAME	DATE
DRAWN	kbrantje	06/28/11
CHECKED		
ENG APPR		
MGR APPR		

SOLID EDGE
UGS - The PLM Company
TITLE
Anti-correction Electrode; S5

UNLESS OTHERWISE SPECIFIED
DIMENSIONS ARE IN MILLIMETERS
ANGLES ±X.X°
2 PL ±X.XX 3 PL ±X.XXX

SIZE A3 | DWG NO | | REV 1
FILE NAME: electrode_anti_correction.dft
SCALE: | WEIGHT: | SHEET 1 OF 1

Title	Material
Anti-correction Electrode	OFHC Copper

Drawing 2

REV | DESCRIPTION | DATE | APPROVED

A
A

$6,796 \pm 0,1$
$5,893 \pm 0,010$
$1,505 \pm 0,1$

Centre Electrode; S3

Anti-correction Electrode; S5

$25 \pm 0,02$
$19,52 \pm 0,05$
$17,503 \pm 0,010$
$21,526$
$25 \pm 0,01$
$27,485 \pm 0,10$

$4 \times R \; 1 \pm 0,10$
$\downarrow 4$

$12,283 \pm 0,10$

$16,23 \pm 0,010$

$2,508 \pm 0,01$
$5,793 \pm 0,01$

SECTION A-A

Anti-correction Side

	NAME	DATE
DRAWN	kbrantje	06/28/11
CHECKED		
ENG APPR		
MGR APPR		

SOLID EDGE
UGS - The PLM Company
TITLE
Correction Electrode, End Tube Side; S4

UNLESS OTHERWISE SPECIFIED
DIMENSIONS ARE IN MILLIMETERS
ANGLES ±X.X°
2 PL ±X.XX 3 PL ±X.XXX

SIZE A3 | DWG NO | | REV 2
FILE NAME: electrode_correction.dft
SCALE: | WEIGHT: | SHEET 1 OF 2

Title	Material
Correction Electrode, End Tube Side	OFHC Copper

105

Sheet 1 (top)

REV	DESCRIPTION	DATE	APPROVED

70° ± 0,10

Connector

0° ± 0,10

Connector

Seperator holes should be fit with the sapphire balls!

2 X Ø 1 ± 0,10
3

Centre Side

	NAME	DATE	**SOLID EDGE**
DRAWN	kbrantje	06/28/11	UGS - The PLM Company
CHECKED			TITLE
ENG APPR			Correction Electrode, End Tube Side; S4
MGR APPR			

UNLESS OTHERWISE SPECIFIED
DIMENSIONS ARE IN MILLIMETERS
ANGLES ±X.X°
2 PL ±X.XX 3 PL ±X.XXX

SIZE A3 · DWG NO · REV 2

FILE NAME: electrode_correction.dft

SCALE: · WEIGHT: · SHEET 2 OF 2

Sheet 2 (bottom)

REV	DESCRIPTION	DATE	APPROVED

A

A

6,78 ± 0,1
5,38 ± 0,010
0,7 ± 0,1
0,7 ± 0,1

Correction Electorde; S2
End Cap Side

Correction Electrode; S4
End Tube Side

27,48 ± 0,10
24,999 ± 0,05
21,525 ± 0,05
17,511 ± 0,010
22,052 ± 0,05
24,922 ± 0,05

0,231 ± 0,010

4 X R 1 ± 0,10
4

12,28 ± 0,010

0,23 ± 0,010

0,805 ± 0,01
0,303 ± 0,01

End Tube side

SECTION A-A

Title	Material
Centre Electrode	OFHC Copper

	NAME	DATE	**SOLID EDGE**
DRAWN	kbrantje	06/28/11	UGS - The PLM Company
CHECKED			TITLE
ENG APPR			Centre Electrode; S3
MGR APPR			

UNLESS OTHERWISE SPECIFIED
DIMENSIONS ARE IN MILLIMETERS
ANGLES ±X.X°
2 PL ±X.XX 3 PL ±X.XXX

SIZE A3 · DWG NO · REV 2

FILE NAME: centre_electrode.dft

SCALE: · WEIGHT: · SHEET 1 OF 2

Drawing 1 (Sheet 2 of 2):

REVISION HISTORY

REV	DESCRIPTION	DATE	APPROVED

4 X 1 ± 0,10
⌁ 2,5

Connector

20°

Connector

0°

Connector

Connector

- Seperator holes should be fit with the sapphire balls!

End Cap side

	NAME	DATE	**SOLID EDGE**	
DRAWN	kbrantje	06/28/11	*UGS - The PLM Company*	
CHECKED				
ENG APPR			TITLE	
MGR APPR			Centre Electrode; S3	

UNLESS OTHERWISE SPECIFIED
DIMENSIONS ARE IN MILLIMETERS
ANGLES ±X.X°
2 PL ±X.XX 3 PL ±X.XXX

SIZE A3	DWG NO	REV 2
FILE NAME: centre_electrode.dft		
SCALE:	WEIGHT:	SHEET 2 OF 2

Drawing 2 (Sheet 1 of 2):

REVISION HISTORY

REV	DESCRIPTION	DATE	APPROVED

Connector

DETAIL B

A

A

45° ± 0,1

B

0° ± 0,10

Connector

	NAME	DATE	**SOLID EDGE**	
DRAWN	kbrantje	06/28/11	*UGS - The PLM Company*	
CHECKED				
ENG APPR			TITLE	
MGR APPR			Correction Electrode, End Cap Side; S2	

Title	Material
Correction Electrode, End Cap Side	OFHC Copper

UNLESS OTHERWISE SPECIFIED
DIMENSIONS ARE IN MILLIMETERS
ANGLES ±X.X°
2 PL ±X.XX 3 PL ±X.XXX

SIZE A3	DWG NO	REV 1
FILE NAME: electrode_correction_endcap.dft		
SCALE:	WEIGHT:	SHEET 1 OF 2

SECTION A-A

Drawing 1 title block:

	NAME	DATE
DRAWN	kbrantje	06/28/11
CHECKED		
ENG APPR		
MGR APPR		

SOLID EDGE
UGS - The PLM Company

TITLE
Correction Electrode, End Cap Side; S2

SIZE A3 | DWG NO | REV 1

FILE NAME: electrode_correction_endcap.dft

SCALE: | WEIGHT: | SHEET 2 OF 2

UNLESS OTHERWISE SPECIFIED
DIMENSIONS ARE IN MILLIMETERS
ANGLES ±X.X°
2 PL ±X.XX 3 PL ±X.XXX

DETAIL B
Attachment point of copper mesh.

SECTION A-A
Attachment point of copper mesh.

Title	Material	Quantity
End Cap	OFHE Copper	1

Drawing 2 title block:

	NAME	DATE
DRAWN	kbrantje	06/28/11
CHECKED		
ENG APPR		
MGR APPR		

SOLID EDGE
UGS - The PLM Company

TITLE
End Cap Electrode; S1

SIZE A3 | DWG NO | REV 2

FILE NAME: electrode_endcap.dft

SCALE: | WEIGHT: | SHEET 1 OF 1

UNLESS OTHERWISE SPECIFIED
DIMENSIONS ARE IN MILLIMETERS
ANGLES ±X.X°
2 PL ±X.XX 3 PL ±X.XXX

Bibliography

1. Gabrielse, G., et al., New Determination of the Fine Structure Constant from the Electron g Value and QED. Physical Review Letters, 2006. **97**(3): p. 030802.

2. G. Gabrielse, D.H., T. Kinoshita, M. Nio, and B. Odom, Erratum: New Determination of the Fine Structure Constant from the Electron g Value and QED. Physical Review Letters, 2007. **99**: p. 039902.

3. Odom, B., et al., New Measurement of the Electron Magnetic Moment Using a One-Electron Quantum Cyclotron. Physical Review Letters, 2006. **97**(3): p. 030801.

4. D. Hanneke, S.F., and G. Gabrielse, New Measurement of the Electron Magnetic Moment and the Fine Structure Constant. Physical Review Letters, 2008. **100**: p. 120801.

5. Verdu, J., et al., Electronic g Factor of Hydrogenlike Oxygen $^{16}O^{7+}$. Physical Review Letters, 2004. **92**(9): p. 093002.

6. Haeffner, H., et al., High-Accuracy Measurement of the Magnetic Moment Anomaly of the Electron Bound in Hydrogenlike Carbon. Physical Review Letters, 2000. **85**(25): p. 5308.

7. Sturm, S., et al., g Factor of Hydrogenlike $^{28}Si^{13+}$. Physical Review Letters, 2011. **107**(2).

8. Shabaev, V.M., Transition probability between the hyperfine structure components of hydrogenlike ions and bound-electron g-factor. Canadian Journal of Physics, 1998. **76**(11): p. 907-910.

9. Johnson, C.E. and H.G. Robinson, Gj Factor of an Ion - Determination of $g_j(^4He^+ 1^2S_{1/2})/g_j(^4He, 2^3S_1)$. Physical Review Letters, 1980. **45**(4): p. 250-252.

10. Beier, T., The g_j factor of a bound electron and the hyperfine structure splitting in hydrogenlike ions. Physics Reports, 2000. **339**(2-3): p. 79-213.

11. NIST. CODATA: Nist reference on constants, units and uncertainty. 2012; Available from: physics.nist.gov/cuu/index.html.

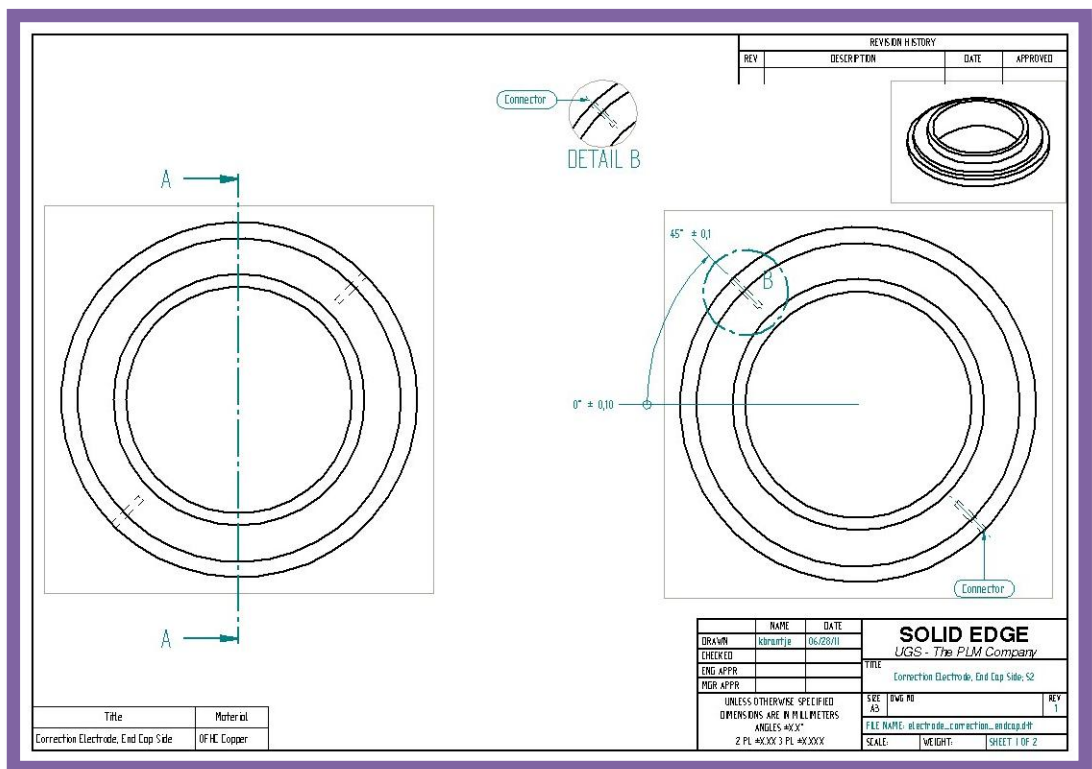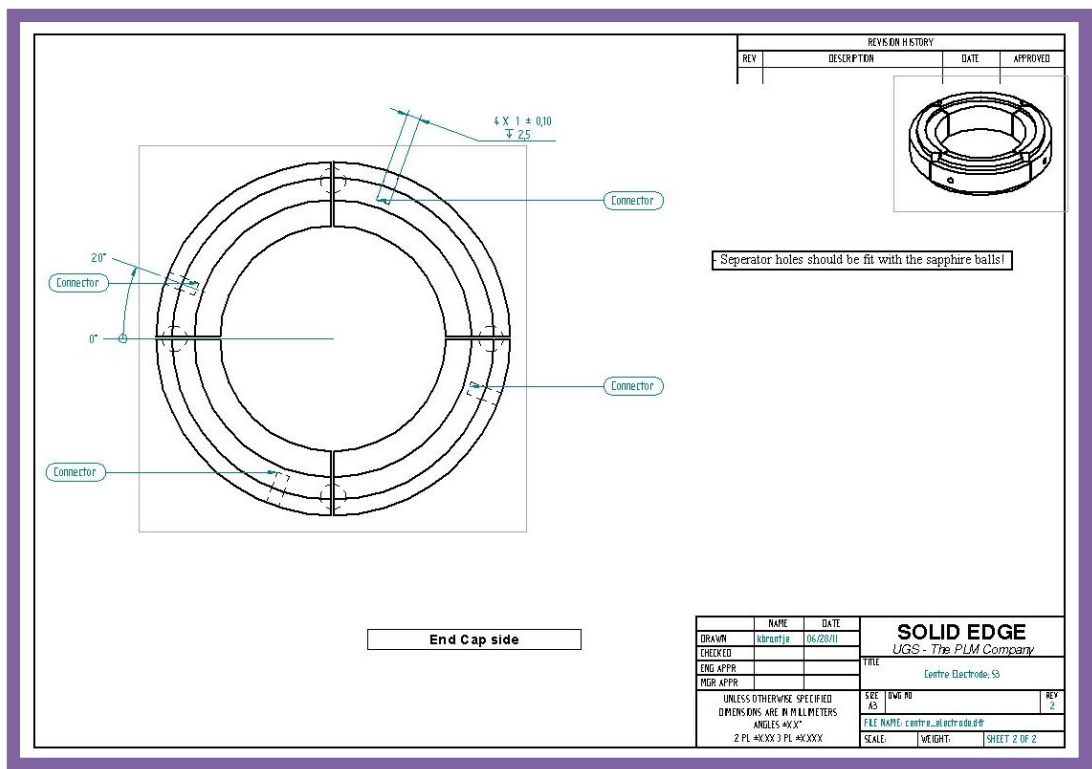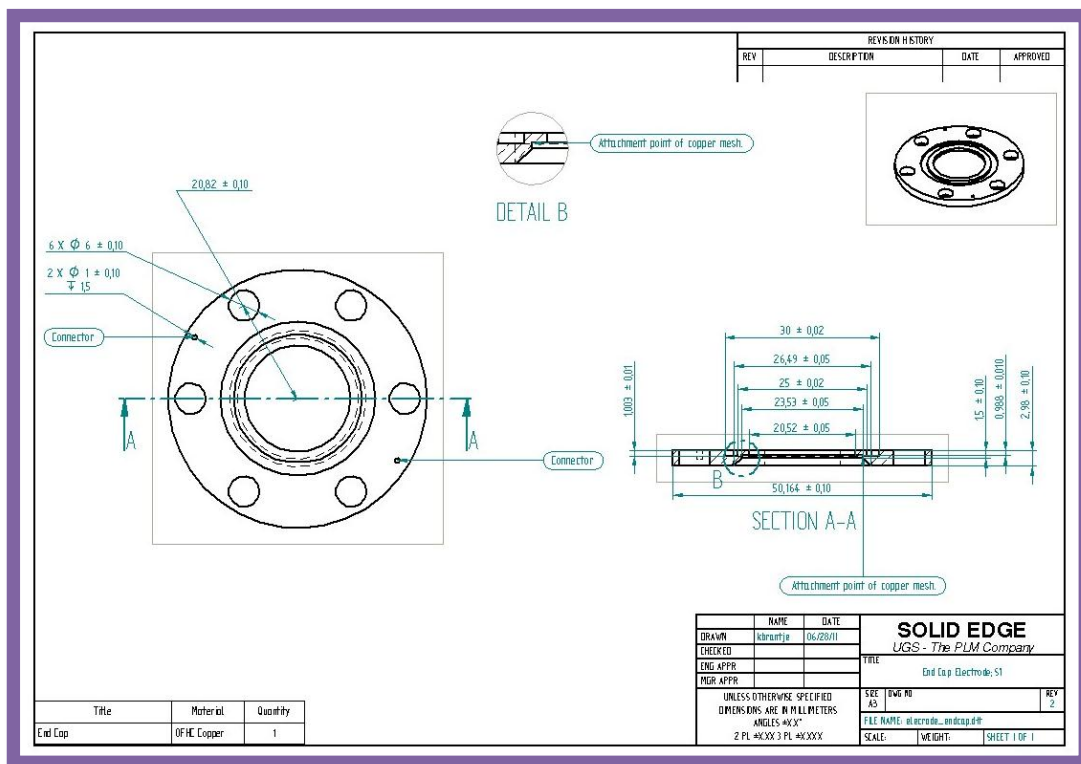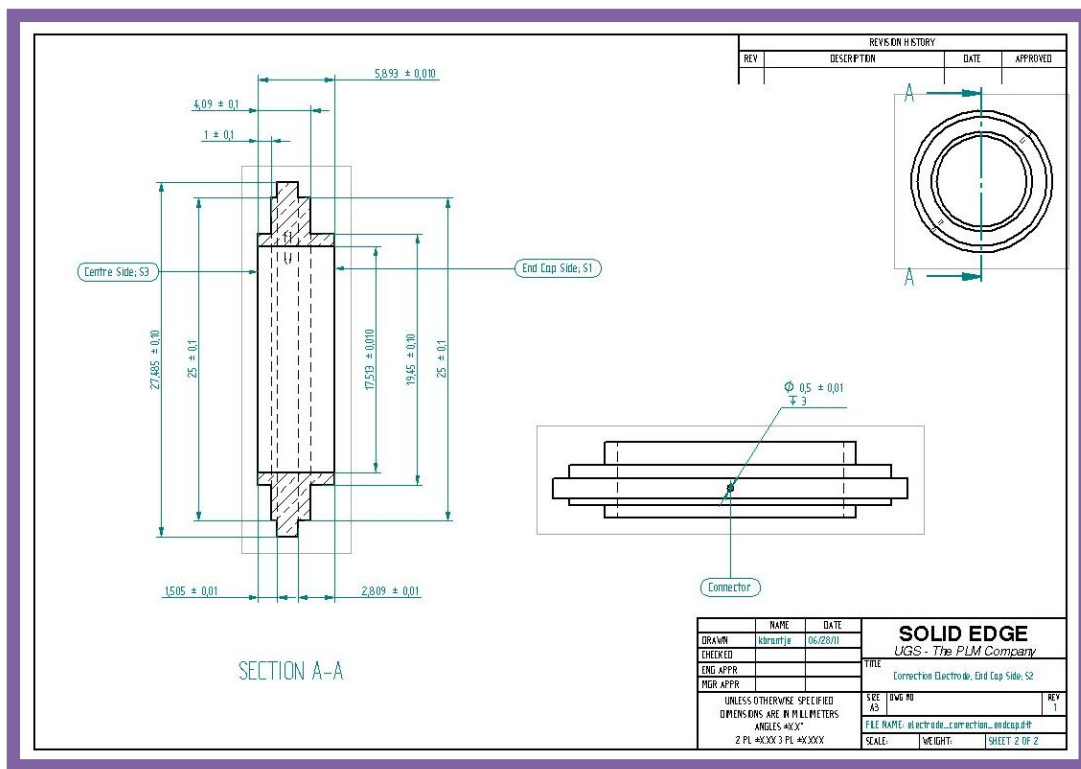12. Dehmelt, H., Continuous Stern-Gerlach Effect - Principle and Idealized Apparatus. Proceedings of the National Academy of Sciences of the United States of America, 1986. **83**(8): p. 2291-2294.

13. Quint, W., The g_j factor of hydrogenic ions. Physica Scripta, 1995. **1995**(T59): p. 203.

14. Schabinger, B. and et al., Towards a g-factor determination of the electron bound in highly-charged calcium ions, in Journal of Physics: Conference Series. 2007. p. 121.

15. Alonso, J., et al., A miniature electron-beam ion source for in-trap creation of highly charged ions. Review of Scientific Instruments, 2006. **77**(3): p. 03A901-3.

16. Quint, W., et al., Laser-microwave double-resonance technique for g-factor measurements in highly charged ions. Physical Review A, 2008. **78**(3): p. 032517.

17. Beier, T., et al., The measurement of the electronic g-factor in hydrogen-like ions --A promising tool for determining fundamental and nuclear constants. The European Physical Journal A - Hadrons and Nuclei, 2002. **15**(1): p. 41-44.

18. W. Greiner, J.R., Quantum Electrodynamics. Theoretical Physics. Vol. 4. 1992, Berlin: Springer-Verlag.

19. Atkinson, D. and P.W. Johnson, Quantum Field Theory: A Self-Contained Course. Vol. 2. 2002: Rinton Press, Inc.

20. Michael E. Peskin, D.V.S., An Introduction To Quantum Field Theory, ed. W. Press. 1995.

21. Furry, W.H., A Symmetry Theorem in the Positron Theory. Physical Review, 1937. **51**(2): p. 125-129.

22. Shabaev, V.M., Generalizations of the virial relations for the Dirac equation in a central field and their applications to the Coulomb field. Journal of Physics B: Atomic, Molecular and Optical Physics, 1991. **24**(21): p. 4479.

23. Shabaev, V.M., Quantum electrodynamical theory for the natural shape of the spectral line. Journal of Physics A: Mathematical and General, 1991. **24**(23): p. 5665.

24. Mohr, P.J., G. Plunien, and G. Soff, QED corrections in heavy atoms. Physics Reports, 1998. **293**(5–6): p. 227-369.

25. W. Greiner, B.M., J. Rafelski, Quantum Electrodynamics of Strong Fields. 1985, Berlin: Springer-Verlag.

26. Grotch, H., Phys. Rev. A, 1970. **2**: p. 1605.

27. Grotch, H. and R.A. Hegstrom, Phys. Rev. A, 1971. **4**: p. 59.

28. Brown, L.S. and G. Gabrielse, Geonium theory: Physics of a single electron or ion in a Penning trap. Reviews of Modern Physics, 1986. **58**(1): p. 233.

29. Gabrielse, G. and F.C. Mackintosh, Cylindrical Penning traps with orthogonalized anharmonicity compensation. International Journal of Mass Spectrometry and Ion Processes, 1984. **57**(1): p. 1-17.

30. Gabrielse, G., L. Haarsma, and S.L. Rolston, Open-endcap Penning traps for high precision experiments. International Journal of Mass Spectrometry and Ion Processes, 1989. **88**(2-3): p. 319-332.

31. Gabrielse, G., Why Is Sideband Mass Spectrometry Possible with Ions in a Penning Trap? Physical Review Letters, 2009. **102**(17): p. 172501.

32. Ulmer, S., First Observation of Spin Flips with a Single Proton Stored in a Cryogenic Penning Trap. 2011, University of Heidelberg.

33. Wineland, D., Principles of the stored ion calorimeter. J. Appl. Phys., 1975. **46**(2): p. 919.

34. Feng, X., et al., Tank circuit model applied to particles in a Penning trap. Journal of Applied Physics, 1996. **79**(1): p. 8-13.

35. Kirschman, R.K., S.V. Lemoff, and J.A. Lipa. Evaluation of GaAs FETs for cryogenic readout. in Infrared readout electronics. 1992. Orlando, FL: SPIE.

36. Robinson, A., Cryogenic amplifier for 1 MHz with a high input impedance using a commercial pseudomorphic high electron mobility transistor. Rev. Sci. Instrum., 2004. **75**(10): p. 3169.

37. Lee, A., A low-power-dissipation broadband cryogenic preamplifier utilizing GaAs MESFETs in parallel. Rev. Sci. Instrum., 1993. **64**(8): p. 2373.

38. Dubin, D.H.E. and T.M. O'Neil, Trapped nonneutral plasmas, liquids, and crystals (the thermal equilibrium states). Reviews of Modern Physics, 1999. **71**(1): p. 87-172.

39.   Maero, G., Cooling of highly charged ion in a Penning trap for HITRAP, in Atomic Physics. 2008.

40.   Poth, H., Electron Cooling - Theory, Experiment, Application. Physics Reports-Review Section of Physics Letters, 1990. **196**(3-4): p. 135-297.

41.   Ichioka, T., Development of intense beam of ultracold antiprotons. 2001, Tokio.

42.   Amoretti, M., et al., The ATHENA antihydrogen apparatus. Nuclear Instruments & Methods in Physics Research Section a-Accelerators Spectrometers Detectors and Associated Equipment, 2004. **518**(3): p. 679-711.

43.   Gabrielse, G., et al., The ingredients of cold antihydrogen: Simultaneous confinement of antiprotons and positrons at 4 K. Physics Letters B, 1999. **455**(1-4): p. 311-315.

44.   Beier, T., et al., HITRAP Technical Design Report. 2003, GSI Darmstadt.

45.   L.A. Dahl, et al. The HITRAP Decelerator Project at GSI in EPAC. 2006. Edinburgh.

46.   L. Dahl, et al. The HITRAP-Decelerator for Heavy Highly-Charged Ions in LINAC 2004. 2004.

47.   B. Hofmann, A. Schempp, and O.K. Kester, The HITRAP RFQ Decelerator at GSI in EPAC. 2006: Edinburgh. p. 1586.

48.   Koszudowski, S., Developments for the HITRAP Cooler Trap and mass measurements around A=96 at SHIPTRAP, in Atomic Physics. 2009.

49.   Ratzinger, U. and R. Tiede, Status of the HIIF RF linac study based on H-mode cavities. Nuclear Instruments and Methods in Physics Research Section A: Accelerators, Spectrometers, Detectors and Associated Equipment, 1998. **415**(1-2): p. 229-235.

50.   Wangler, T.P., Principles of RF Linear Accelerators. 1998: John Wiley and Sons, New York.

51.   F. Herfurth, e.a., HITRAP Commissioning – Status and Perspectives. 2011, GSI Helmholtzzentrum für Schwerionenforschung GmbH.

52.   Hofmann, B., Konstruktion und Aufbau einer kompakten RFQ-Spiral-Struktur zum Abbremsen hochgeladener Schwerionenstrahlen fuer dat HITRAP-Project de GSI. 2008, Frankfurt.

53.   Geyer, S., et al., Characterization of the SPARC-EBIT at GSI. Journal of Instrumentation, 2010. **5**.

54.   Sokolov, A., et al., SPARC EBIT - a charge breeder for the HITRAP project. Journal of Instrumentation, 2010. **5**.

55.   Klaft, I., et al., Precision Laser Spectroscopy of the Ground State Hyperfine Splitting of Hydrogenlike ^{209}Bi^{82+}. Physical Review Letters, 1994. **73**(18): p. 2425-2427.

56.   Seelig, P., et al., Ground State Hyperfine Splitting of Hydrogenlike ^{207}Pb^{81+} by Laser Excitation of a Bunched Ion Beam in the GSI Experimental Storage Ring. Physical Review Letters, 1998. **81**(22): p. 4824-4827.

57.   Crespo López-Urrutia, J.R., et al., Direct Observation of the Spontaneous Emission of the Hyperfine Transition F=4 to F=3 in Ground State Hydrogenlike ^{165}Ho^{66+} in an Electron Beam Ion Trap. Physical Review Letters, 1996. **77**(5): p. 826-829.

58.   Crespo López-Urrutia, J.R., et al., Nuclear magnetization distribution radii determined by hyperfine transitions in the 1s level of H-like ions ^{185}Re^{74+} and ^{187}Re^{74+}. Physical Review A, 1998. **57**(2): p. 879-887.

59. Beiersdorfer, P., et al., Hyperfine structure of hydrogenlike thallium isotopes. Physical Review A, 2001. **64**(3): p. 032506.

60. Lukas, G. and et al., Formation of Strongly Coupled Plasmas from MultiComponent Ions in a Penning Trap. Physica Scripta, 2005. **71**(1): p. 60.

61. Greaves, R.G. and C.M. Surko, Inward Transport and Compression of a Positron Plasma by a Rotating Electric Field. Physical Review Letters, 2000. **85**(9): p. 1883-1886.

62. Vogel, M., Proposed precision laser spectrometer for trapped, highly charged ions. Rev. Sci. Instrum., 2005. **76**(10): p. 103102.

63. Arnould, M. and K. Takahashi, Nuclear astrophysics. Reports on Progress in Physics, 1999. **62**(3): p. 395.

64. Schatz, H., The importance of nuclear masses in the astrophysical rp-process. International Journal of Mass Spectrometry, 2006. **251**(2-3): p. 293-299.

65. Hardy, J. and I. Towner, Standard-Model Tests with Superallowed β-Decay: An Important Application of Very Precise Mass Measurements. Hyperfine Interactions, 2001. **132**(1): p. 115-126.

66. Blaum, K., High-accuracy mass spectrometry with stored ions. Physics Reports, 2006. **425**(1): p. 1-78.

67. Bradley, M.P., et al., Penning Trap Measurements of the Masses of ^{133}Cs, ^{87,85}Rb, and ^{23}Na with Uncertainties ≤0.2 ppb. Physical Review Letters, 1999. **83**(22): p. 4510-4513.

68. Herfurth, F., et al., Precision measurements with highly charged ions at rest: The HITRAP project at GSI. International Journal of Mass Spectrometry, 2006. **251**(2-3): p. 266-272.

69. Lemell, C., et al., Electron emission from surfaces induced by HCI and lasers. Nuclear Instruments and Methods in Physics Research Section B: Beam Interactions with Materials and Atoms, 2005. **235**(1-4): p. 425-430.

70. Khemliche, H., et al., Hollow Atom Dynamics on LiF Covered Au(111): Role of the Surface Electronic Structure. Physical Review Letters, 1998. **81**(6): p. 1219-1222.

71. Briand, J.P., et al., Observation of Hollow Atoms or Ions above Insulator and Metal Surfaces. Physical Review Letters, 1996. **77**(8): p. 1452-1455.

72. Ullrich, J. and et al., Recoil-ion and electron momentum spectroscopy: reaction-microscopes. Reports on Progress in Physics, 2003. **66**(9): p. 1463.

73. Dörner, R., et al., Cold Target Recoil Ion Momentum Spectroscopy: a 'momentum microscope' to view atomic collision dynamics. Physics Reports, 2000. **330**(2-3): p. 95-192.

74. Bollen, G., et al., ISOLTRAP: a tandem Penning trap system for accurate on-line mass determination of short-lived isotopes. Nuclear Instruments and Methods in Physics Research Section A: Accelerators, Spectrometers, Detectors and Associated Equipment, 1996. **368**(3): p. 675-697.

75. SPECS-GmbH, Performance Data Sheet Ion Source: IQE 12/38, SPECS-GmbH, Editor. 2004.

76. SPECS-GmbH, User's Manual for the IQE 12/38, SPECS-GmbH, Editor. 2004.

77. Brillouin, L., A Theorem of Larmor and Its Importance for Electrons in Magnetic Fields. Physical Review, 1945. **67**(7-8): p. 260.

112

78. Mitchell, D.W. and R.D. Smith, Cyclotron motion of two Coulombically interacting ion clouds with implications to Fourier-transform ion cyclotron resonance mass spectrometry. Physical Review E, 1995. **52**(4): p. 4366.

79. Kuroda, N., Accumulation of a large number of antiprotons and production of an ultra-slow antiproton beam. 2003, University of Tokyo.

80. Dubin, D.H.E., Theory of electrostatic fluid modes in a cold spheroidal non-neutral plasma. Physical Review Letters, 1991. **66**(16): p. 2076.

81. Hermanspahn, N., et al., Observation of the Continuous Stern-Gerlach Effect on an Electron Bound in an Atomic Ion. Physical Review Letters, 2000. **84**(3): p. 427.

82. Brantjes, N., et al., A Penning trap for g-factor measurements in highly charged ions by laser-microwave double-resonance spectroscopy. Hyperfine Interactions, 2011: p. 1-6.

83. Behlke Power Electronics online catalogue. 2008; Available from: http://www.behlke.de.

84. Magnex, Technical Specifications for a 7.0 Tesla/160 mm Actively Shielded Vertical RT Bore Magnet System for Ion Trap Applications. 2009.

85. Lindenfels, D.v., Development of an Ion Trap Experiment for the Measurement of the Electron Magnetic Moment by Double-Resonance Spectroscopy. 2010, Ruprecht-Karls-University: Heidelberg.

86. von Lindenfels, D., et al., Bound electron g-factor measurement by double-resonance spectroscopy on a fine-structure transition. Canadian Journal of Physics, 2011. **89**(1): p. 79-84.

87. Schetgen, R., The ARRL Handbook for Radio Amateurs. 1994: The American Radio Relay League.

88. Ulmer, S., et al., The quality factor of a superconducting rf resonator in a magnetic field. Review of Scientific Instruments, 2009. **80**(12): p. 123302-8.

89. Huellen, M., Axial Amplifier, Manual. 2011, GSI-Darmstadt.

90. Huellen, M., Entwicklung und Test eines elektronischen Nachweissystems fuer hoch geladene Ionen in einer Penning-Falle, in Fakultaet Elektro- und Informationstechnik. 2011, Hochschule Karlsruhe - Technik und Wirtschaft: Karlsruhe

91. Stahl, S.K.-H., Aufbau eines Experimentes zur Bestimmung elektronischer g-Faktoren einzelner wasserstoffähnlicher Ionen. 1998, Johannes Gutenberg-Universität: Mainz.

92. Metcalf, H.J. and P.v.d. Straaten, Laser cooling and trapping. 1999: Springer. 323.

93. Foot, C.J., Atomic Physics. 2005: Oxford University Press. 331.

94. Schneider, S.M., W. Greiner, and G. Soff, The Transition Time for the Ground-State Hyperfine Splitting of $^{209}Bi^{82+}$. Zeitschrift Fur Physik D-Atoms Molecules and Clusters, 1994. **31**(3): p. 143-144.

95. Shabaev, V.M., Hyperfine structure of hydrogen-like ions. Journal of Physics B: Atomic, Molecular and Optical Physics, 1994. **27**(24): p. 5825.

96. Beiersdorfer, P., et al., Measurement of QED and Hyperfine Splitting in the $2s_{1/2} - 2p_{3/2}$ X-Ray Transition in Li-like $^{209}Bi^{80+}$. Physical Review Letters, 1998. **80**(14): p. 3022-3025.

97. Mackel, V., et al., Laser Spectroscopy on Forbidden Transitions in Trapped Highly Charged Ar^{13+} Ions. Physical Review Letters, 2011. **107**(14).

98.   Morenzoni, E., et al., Performance of microchannel plates in high magnetic fields. Nuclear Instruments and Methods in Physics Research Section A: Accelerators, Spectrometers, Detectors and Associated Equipment, 1988. **263**(2-3): p. 397-400.

99.   Fraser, G.W., The gain, temporal resolution and magnetic-field immunity of microchannel plates. Nuclear Instruments and Methods in Physics Research Section A: Accelerators, Spectrometers, Detectors and Associated Equipment, 1990. **291**(3): p. 595-606.

100.   Kuehnel, K.-U., C.D. Schröter, and J. Ullrich. Operating MCP Detectors as Cryogenic Temperatures. in EPAC08. 2008. Genoa, Italy.

101.   Roth, P. and G.W. Fraser, Microchannel plate resistance at cryogenic temperatures. Nuclear Instruments and Methods in Physics Research Section A: Accelerators, Spectrometers, Detectors and Associated Equipment, 2000. **439**(1): p. 134-137.

102.   Rosen, S., et al., Operating a triple stack microchannel plate-phosphor assembly for single particle counting in the 12--300 K temperature range. Review of Scientific Instruments, 2007. **78**(11): p. 113301-5.

103.   Schlachter, A.S. Charge-changing-collisions. in 10th Int. Cyc. Conf. Michigan. 1984.

104.   Herzberg, G., Dissociation Energy and Ionization Potential of Molecular Hydrogen. Physical Review Letters, 1969. **23**(19): p. 1081-1083.

105.   Vogel, M. and W. Quint, Trap-assisted precision spectroscopy of forbidden transitions in highly-charged ions. Physics Reports, 2010. **490**(1–2): p. 1-47.

106.   Vandyck, R.S., et al., Number Dependency in the Compensated Penning Trap. Physical Review A, 1989. 40(11): p. 6308-6313.

107.   Sturm, S., et al., Phase-Sensitive Cyclotron Frequency Measurements at Ultralow Energies. Physical Review Letters, 2011. 107(14).

Acknowledgements

Although the whips and scorns of time, spent both as a PhD student and as an expat, have been well documented, there were many people who, practically or in spirit, greatly alleviated this burden. I hold many fond memories of the friends I made while working towards this thesis. To those around me in the past few years I wish to convey my expressed gratitude.

I wish to specifically thank both of my direct supervisors: Wolfgang Quint and Frank Herfurth. I could always count on Wolfgang for advice and scientific discussions. Also he contributed many valuable suggestions and corrections to my reports, papers, presentations and finally this thesis itself. Frank became important as I started work on the Cooler trap. We had many encouraging discussions and he provided important feedback on many parts of my thesis. Also, I want to thank to Klaus Blaum who kindly agreed to referee my thesis and to take a seat in the examination committee and Werner Aeschbach-Hertig who also agreed to sit on my committee. Andrey Surzykov not only agreed to sit on my committee, but I very much enjoyed his lectures on relativistic quantum mechanics as well.

I am thankful to the atomic-physics group at GSI for its warm and friendly atmosphere. In particular I am thankful to the members of the HITRAP group with whom, amongst other things, I spend many exhausting but enjoyable beam-time shifts. I want to thank especially Svetlana Fedotova, Nikita Kotovskiy, Alexey Sokolov and Gleb Vorobjev with whom I enjoyed a great cooperation on the Cooler trap project. Also I am very grateful for their friendship, whether it was on the football field, behind the grill or just drinking beer. Furthermore, I want to specifically thank Zoran Andjelkovic and Manuel Vogel who first welcomed me to the AP group and guided me through the first few days. I enjoyed many scientific discussions with them. Also, I thank Oliver Zurkan, Harald Hahn and Stefan Stahl for their technical help. Their knowledge and experience was very important to this work. Similarly I want to thank Stefan Ulmer for his advice and helpful suggestions.

During my stay in Darmstadt I made many international friendships. I am very grateful for all of those and I immensely enjoyed the trips and excursions we undertook together. I still have many of the photographs and they never fail to make me smile. A special mention goes to Klaas Vantournhout who proofread parts of the theory section.

Last but not least I want to thank my parents and my brothers and sister for their everlasting support and faith. Especially my father has been a great help and I could always trust him to stand behind me.